7-12-2019

Evaluation of the cracking performance of geogrid-reinforced hot-mix asphalt for airfield applications

Daniel Offenbacker
Rowan University

EVALUATION OF THE CRACKING PERFORMANCE OF GEOGRID-REINFORCED HOT-MIX ASPHALT FOR AIRFIELD APPLICATIONS

by

Daniel Offenbacker

A Dissertation

Submitted to the
Department of Civil and Environmental Engineering
College of Engineering
In partial fulfillment of the requirement
For the degree of
Doctor of Philosophy
at
Rowan University
April 19, 2019

Dissertation Chair: Yusuf Mehta, Ph.D. P.E.

Dedications

This thesis is first dedicated to my wife, Liz Offenbacker, for her help, patience, love, and support to help me persevere and fulfill my dreams. I also would like to dedicate this thesis to my parents, Sara Offenbacker, George Romeo, and Cindy Vitto, my brother Michael Offenbacker, my sister Alicia Offenbacker, and the rest of my supportive family. Finally, I would like to dedicate this dissertation to my dad, Daniel Offenbacker II, whose early passing in my life helped me to see that life is short and should be enjoyed and cherished with family and friends.

Acknowledgments

I hereby acknowledge my appreciation and due gratitude to my advisor and study leader, Dr. Yusuf Mehta, for the academic guidance, mentorship, and technical advice rendered during the course of this thesis. This thesis would not have been completed without his exemplary motivation and encouragement. Special thanks also go to Dr. Cheng Zhu, for his continued guidance and support which inevitably made this research study a success. Special thanks are also owed to my committee members Dr. Douglas Cleary, Dr. Gilson Lomboy, and Dr. Tirupathi Chandrupatla for their valuable input and time spent serving on my thesis committee. This study was conducted as part of Department of Defense (DoD) Research Project entitled "Development of Innovative Materials and Methods to Solve United States Department of Defense (DoD) Horizontal Infrastructure Challenges in Cold Regions." I thank the DoD and the United States Army Corps of Engineers (USACE) for their support in funding this research study for their help in the course of this research work. In particular, special thanks are due to Dr. Wade Lein, Mr. Jeremy Robinson, and Mr. Christopher Decarlo. Finally, the success of my degree would not have been possible without the support of my colleagues and personal friends. In this regard, I wish to mention some of them by name: Dr. Gourab Saha, Dr. Parth Bhavsar, Mr. Andrae Francois, Dr. Ayman Ali, and Ms. Caitlin Purdy. Finally, I would like to acknowledge all the undergraduate students and laboratory technicians that made the success of my degree possible.

Abstract

Daniel Offenbacker
EVALUATION OF THE CRACKING PERFORMANCE OF GEOGRID-REINFORCED HOT-MIX ASPHALT FOR AIRFIELD APPLICATIONS
2018-2019
Yusuf Mehta, Ph.D. P.E.
Doctor of Philosophy

The objective of this study was to evaluate the fatigue cracking performance of geogrid-reinforced Hot-Mix Asphalt (HMA) for use in airfield runways. An airfield HMA mixture with four different geogrid types were selected for this study. The geogrids varied in tensile strength, coating type, opening size, thickness, and fiber material. Several different laboratory performance tests were conducted (Dynamic Complex Modulus, DCM, Overlay Test, OT, and Indirect Tensile Strength, ITS) and the fatigue and/or cracking performance was evaluated. Additionally, different approaches were adopted or developed for the modeling of geogrids in HMA using Finite Element Modeling (FEM). Finally, a Life-Cycle Cost Analysis (LCCA) was conducted to determine if the additional investment of using geogrids in HMA is a cost-effective strategy over the pavement service life. Overall, this study discovered a significant increase in the fatigue cracking performance when reinforcing HMA airfield mixtures with geogrids. Additionally, the geogrids exhibited crack deterring characteristics that slowed down crack propagation in the HMA mixture, especially when embedded below the neutral axis. Furthermore, a unique approach of FEA was developed to evaluate impact of geogrid-reinforced HMA mixtures under different loading conditions and configurations within a pavement system. Finally, geogrids proved to be a cost-effective strategy when the reinforcement is embedded below the mid-depth of the HMA layer.

Table of Contents

Table of Contents (Continued)

Table of Contents (Continued)

Table of Contents (Continued)

List of Figures

Figure Page

List of Figures (Continued)

List of Figures (Continued)

Figure | Page

List of Figures (Continued)

Figure Page

List of Figures (Continued)

Figure Page

List of Tables

List of Tables (Continued)

Table Page

Chapter 1

Background and Introduction

Introduction

Geogrid reinforcements are used in pavement systems to mitigate pavement distresses and improve service life [1]. Because of their potential to improve pavement service life, the use of geogrid reinforcements in pavement systems have gained increased interest by researchers and highway agencies and has led to nationally funded research projects and federal pavement construction guidelines [2]–[4]. Geogrids reinforce pavement systems through three primary mechanisms including: (i) lateral aggregate restraint (LAR), (ii) wider stress distribution, and (iii) upward reactionary forces due to tensioned membrane effect [5]. Past studies have primarily focused on the use of geogrids in unbound pavement layers to reduce the surface deformation (or rutting) in pavement systems [6]–[11].

Geogrid reinforcements are primarily implemented in pavement systems for the stabilization of weak unbound pavement soil layers. Various researchers have shown that the use of geogrids for reinforcing unbound pavement layers is successful in reducing permanent surface deformation (or rutting) [6]–[11]. The current state-of-the-art investigated the reinforcement of several different subgrade materials with California Bearing Ratios (CBR) between 1% and 8%. Testing of the reinforced subgrades was conducted using large scale tank testing, accelerated pavement testing, and public trafficking. Several studies reported similar findings; that is, a reduction in rutting for geogrid-reinforced pavement sections [6]–[10]. Robinson et al. [11] evaluated the reinforcement of base-subgrade interfaces using two different triaxial geogrid types. These sections were tested using truck tire loading applied using a Heavy Vehicle Simulator (HVS). The study concluded that sections reinforced with geogrids experienced less rutting than unreinforced sections [11]. Gu et al. [12] also found a reduction in rutting with geogrid-reinforced unbound pavement layers, however, it was also discovered that the reinforcement of unbound pavement layer has minimal impact on the cracking performance of HMA layers.

Therefore, researchers have implemented geogrids directly beneath or within HMA layers to improve the cracking durability. To evaluate the impact on fatigue performance due to geogrid reinforcement, bending beam fatigue testing has been conducted at intermediate temperatures (approximately 20°C) on prism samples [13]–[16]. HMA materials have shown a significant increase in the fatigue performance with the use of geogrid reinforcements [15], [17]–[20]. It has also been found that implementation of geogrid within HMA samples exhibits greater fatigue resistance when it is constructed at the bottom of the HMA layer [19], [20]. Researchers have discovered that the embedded depth of the geogrid reinforcement in the HMA layer also impacts the overall fatigue life [18], [21].

However, the research has been limited to primarily highway HMA mixtures [15], [17]–[20]. Airfield HMA mixtures are conventionally much stiffer than highway HMA mixtures to ensure structural capacity under the heavier loading conditions. The increase in stiffness may have a significant negative impact on the performance of geogrid reinforcements on the cracking resistance of HMA materials. Furthermore, there is uncertainty regarding the need for tack coat in laboratory fabrication of geogrid-reinforced HMA samples [4] and the amount of tack coat, if used [13]. Finally, the cracking resistance of geogrid-reinforced HMA mixtures may be impacted by the environmental conditions. Thus far, intermediate temperature conditions (15°C to 25°C) have been the typical testing temperature range in past studies that investigated the cracking resistance of HMA mixtures [20]–[23]; however, it is vital to consider alternative environmental or temperature conditions to ensure the structural capacity of geogrid-reinforced HMA under conditions that could be experienced in the field.

Research Hypothesis

The two research hypotheses are:

1) The environmental and construction conditions associated with cold regions (i.e. cold temperature and freeze-thaw cycling) will reduce the fatigue resistance of geogrid-reinforced HMA.
2) The use of geogrids within HMA mixtures is a cost-effective strategy over the service life of flexible pavement systems.

Research Objectives

The objectives to prove the hypotheses are summarized as follows:

- Quantify the impact in HMA laboratory cracking performance due to geogrid reinforcement at low and intermediate temperatures.
- Evaluate geogrid-reinforced HMA laboratory fatigue performance after experiencing freeze-thaw cycling.

- Develop a Finite Element Model (FEM) approach to quantify change in pavement response (tensile strains) due to geogrid reinforcement.
- Quantify effect of geogrid embedment depth on the tensile strain and fatigue performance using laboratory testing and FEM.
- Conduct Life-Cycle Cost Analysis (LCCA) to determine the cost-effectiveness of using geogrids in HMA pavement systems.

Outline of Research

This research study is divided into eight chapters. The first chapter provides a brief introduction and outline and goals of the research. Following this, chapter two presents the literature review on geosynthetics and flexible pavements. This section summarizes the critical points of flexible pavement systems, various types of geosynthetics, the reinforcement mechanisms associated with geosynthetics, and studies conducted on geosynthetic-reinforced pavement systems.

Following chapter two, chapter three presents a description of the materials and methods used in this study. This chapter includes the details of the gradation, the mix design, and the geogrid types used for the laboratory testing. This chapter also discusses the different compaction methods and the experimental matrix for this study. Chapter four presents the findings from each laboratory test and direct interpretations from the findings.

In chapter five, a description of the finite element model is provided including the geometry, meshing, and loading conditions. This chapter also shows the verification of the finite element model with the laboratory testing and full-scale pavement simulations.

Chapter six consists of a cost evaluation of the use of geogrid-reinforced HMA based on the findings from the laboratory tests. This chapter explains the assumptions used, the service life estimation methodology, and the cost-effectiveness of using geogrid-reinforced HMA. Chapter seven provides an overall ranking of each geogrid type based on the results of the laboratory performance testing and the cost evaluation. Chapter eight concludes the study with a summary of the project and findings, conclusions that can be extrapolated from the findings, and any limitations and recommendations for future study.

Chapter 2

Literature Review

Introduction

This chapter is aimed at reviewing relevant literature-to-date regarding the topic of geogrid-reinforced HMA. The topics include a brief review of general flexible pavement structural design, methods of evaluating the laboratory performance of HMA, and types of geosynthetics in pavement applications. Additionally, this chapter presents the results of the literature review on past laboratory and field performance of geogrids in flexible pavement applications. Finally, a review of the methods utilized to numerically model geogrid reinforcement in pavement systems is presented.

General Overview of Flexible Pavement Distresses

Flexible pavements experience distress or failures due to repeated traffic loading. Three primary distresses are commonly experienced in flexible pavement: rutting, fatigue cracking, and thermal cracking or low temperature cracking. Rutting can be commonly observed by surface deformation and can occur in the HMA surface layer or the subgrade with both rutting forms resulting in surface depressions [11], [24], [25]. Fatigue cracking can occur when the maximum tensile strain of the HMA layer exceeds the tensile stain at failure. This commonly occurs in intermediate temperature range (5°C -25°C) [26], [27]. All forms of cracking will lead to greater water penetration into the pavement system, resulting in erosion of the underlying pavement layers and eventually a structural and functional failure. Therefore, laboratory testing is typically conducted to evaluate the susceptibility of HMA mixtures to these distresses prior to pavement construction to ensure the structural integrity is sufficient for the designed traffic loading [28].

Laboratory Performance Characterization of Asphalt Mixtures

In literature, small-scale laboratory tests are conducted on pavement materials to evaluate their adequacy under different loading and environmental conditions. Several laboratory tests have been developed for the purpose of evaluating the fatigue cracking performance of HMA materials [29], [30]. Table 1 presents a summary of the most common tests typically used in characterizing the behavior (mainly cracking resistant) of asphalt mixtures [29], [30]. As shown in Table 1, the most commonly used tests are the Dynamic Complex Modulus (|E*|, AASHTO T278), Indirect Tension Test (IDT, AAHSTO T322), Overlay Tester (OT, Tex-248-F), the Four-Point Bending Beam Fatigue (BBF, AASHTO T322 or ASTM D7460), Semi-Circular Bend (SCB, AASHTO TP124, TP105, and ASTM D8044), and Disk Compaction Test (DCT, ASTM D7313).

Despite the common usage of these cracking tests for HMA mixtures, their usage for geogrid-reinforced HMA (defined as asphalt pavements or lab samples in which the geogrid is embedded) is rare. This is the case because most studies found in literature focused on evaluating the benefits of geogrids as reinforcement of unbound pavement layers. Additionally, several of these laboratory tests include sample notching, which is not possible for geogrid-reinforced HMA samples. This is because the geogrid reinforcement could be cut or compromised during the notching process, due to the lack of visibility when the geogrid is embedded in HMA. Therefore, most researchers utilize laboratory tests that do not involve notching to evaluate the fatigue cracking performance of geogrid-reinforced HMA [13], [15], [17], [18], [20]–[23]. A detailed discussion of the considered tests (i.e., DCM, IDT, OT, and BBF) is presented in the following subsections.

Table 1

Commonly Used Laboratory Performance Tests for HMA Mixtures

Laboratory Test	Relevant Specifications	Specimen Dimension	Distress Measured
Dynamic Complex Modulus	AASHTO T378	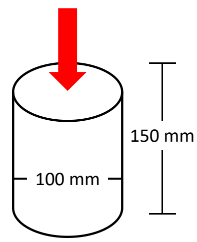	Fatigue Resistance Rutting Resistance
Indirect Tension Test	AASHTO T322	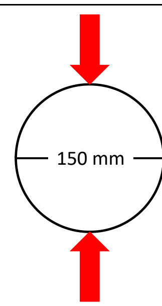	Intermediate Cracking Low-Temperature Cracking
Overlay Test	Tex-248-F	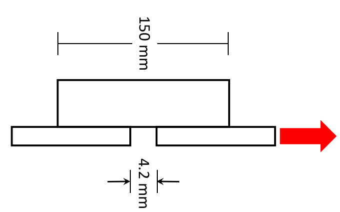	Reflective Cracking
Four-Point Bending Beam Fatigue	AASHTO T322 ASTM D7460	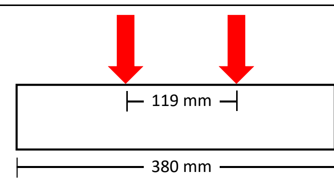	Fatigue Cracking

Table 2 (continued)

Commonly Used Laboratory Performance Tests for HMA Mixtures

Laboratory Test	Relevant Specifications	Specimen Dimension	Distress Measured
Semicircular Bend (SCB)	AASHTO TP 124 AASHTO TP 105 ASTM D8044	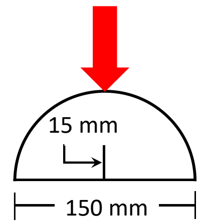	Intermediate Cracking Low-Temperature Cracking
Disk Compaction Test (DCT)	ASTM D7313	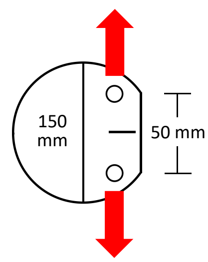	Low-Temperature Cracking

Dynamic Complex Modulus (|E*|) Test. The Dynamic Complex Modulus ($|E^*|$) test measures and quantifies the viscoelastic behavior of HMA materials. The stress-strain response of viscoelastic materials under continuous cyclic loading (Figure 1a) is defined through the complex modulus ($|E^*|$) as a function of angular frequency (ω) [28]. $|E^*|$ allows for the consideration of both the elastic stiffness (referred to as Storage Modulus, E') and the internal damping due to the viscous nature of the material (referred to as Loss Modulus, E''). The complex modulus can be graphically represented assuming the elastic and viscous components as vectors as shown in Figure 1b.

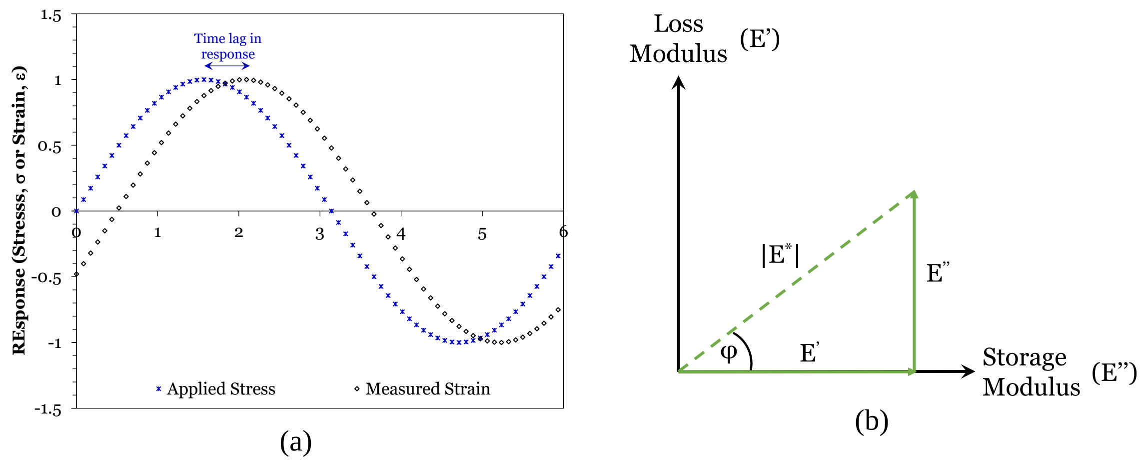

Figure 1. (a) Loading-Response Cycle in DCM Testing and (b) Vector Representation of the Dynamic Complex Modulus (|E*|).

The associated angle between the complex modulus and the elastic component is known as the phase angle (φ), which is the delay in response due to the internal damping of the viscous component. The phase angle (φ) is dependent on the time lag in response between the applied stress loading and the measured strain response (Figure 1a). The storage modulus (E') and loss modulus (E") can then be determined using |E*| and φ. These relationships are shown in Equations 1 and 2 [28].

$$E'(\omega) = |E^*| \times \cos(\varphi) \tag{1}$$

$$E''(\omega) = |E^*| \times \sin(\varphi) \tag{2}$$

Where,

E' = Storage Modulus, MPa

E'' = Loss Modulus, MPa

$|E^*|$ = Dynamic complex modulus, MPa

φ = Phase angle, deg

In addition, the |E*| parameter is defined as the ratio of the peak applied axial stress at a given time (i.e., test frequency) to the peak measured recoverable axial strain at the same time. Equation 3 below presents the definition of |E*| [30], [31].

$$|E^*| = \frac{\sigma(t)}{\varepsilon(t)} \tag{3}$$

Where,

|E*| = Dynamic complex modulus, MPa

σ(t) = Peak axial compressive stress, MPa

ε(t) = Peak axial compressive strain

According to the AASHTO T378, the DCM test is conducted at wide range of loading frequencies (0.1, 0.5, 1, 5, 10, and 25 Hz) and temperatures (4°C, 21°C, 37°C, and 54°C). This is the case because the behavior of asphalt mixtures is viscoelastic in nature. Specimens prepared for this test are compacted, using a Superpave Gyratory Compactor (SGC), to a height of 170 mm. The SGC samples are then cored and the ends saw cut to obtain cylindrical shaped specimens having a diameter of 100 mm (4 in.) and a height of 150 mm (6 in.). It is noted that the applied stress, as specified in AASHTO T378, is selected such that the resulting strain response is between 75 and 125 micro-strains (□□). This is to ensure minimal plastic deformation is induced on the sample.

Using the generated testing results (for all frequencies and test temperatures), one can then determine, using the time-temperature superposition, a materials characteristics curve known as the |E*| master curve. The master curve provides insights into the performance of asphalt mixtures at high and low temperature. The master curve is also considered a valuable input in mechanistic-empirical flexible pavements structural design methods. In general, higher |E*| values are desired for low frequency loading (or high temperatures) and lower |E*| values are desired for high frequency loading (or lower temperatures).

Indirect Tension (IDT) Test. The Indirect Tension (IDT) test is typically used to evaluate the fracture resistance of HMA mixtures [29], [30], [32]. The IDT test involves loading an HMA sample diametrically causing horizontal tensile stresses at the center of the sample (Figure 2). The horizontal tensile stress ultimately reaches a maximum threshold and then fractures the test specimen. To quantify the maximum horizontal tensile stress, a simple and general equation (Equation 4) has been developed using the load applied and specimen dimensions (AASHTO T322). A greater horizontal tensile strength value indicates greater crack resistance in HMA mixtures.

$$\sigma_t = \frac{2 \times P_{ult}}{\pi \times d \times t} \tag{4}$$

Where,

σ_t = Maximum tensile strength, MPa

P_{ult} = Peak Load, N

d = Specimen diameter, mm

t = Specimen thickness, mm

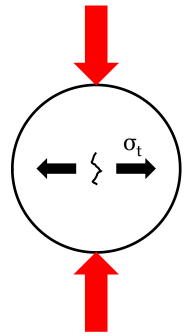

Figure 2. Illustration of ITS loading and resulting tensile stress (σ_t) at the center of the HMA sample.

Indirect Tensile Asphalt Cracking Test (IDEAL-CT) Analysis. Further analysis of the IDT test results, when the test is conducted at 25°C, were proposed by Zhuo et al. [32] using fracture parameters obtained from the IDT load-displacement curves. Figure 3 presents a typical load-displacement curve from IDT testing and the fracture parameters used in the IDEAL-CT analysis. One fracture parameter measure that is determined is the work done during the cracking process (W_d) by computing the area beneath the load displacement curve (Figure 3).

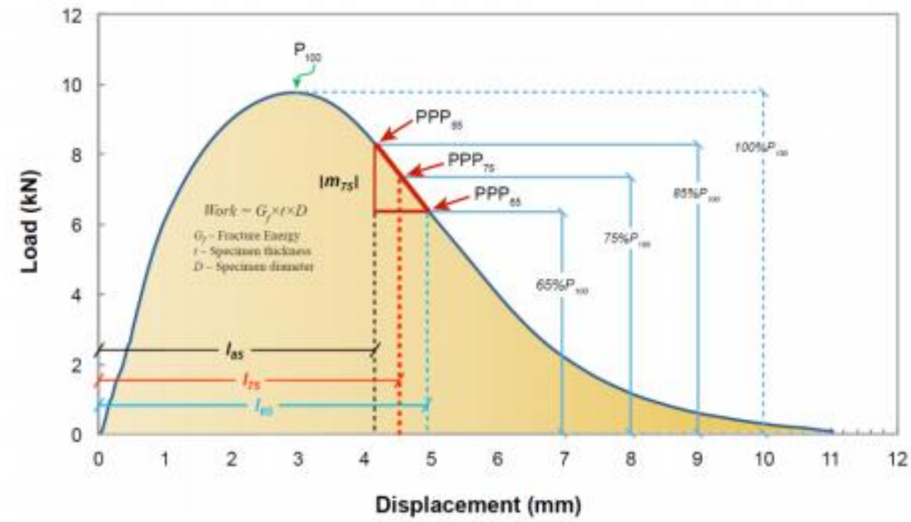

Figure 3. Representative load versus displacement and respective parameters used in the IDEAL-CT evaluation [32].

The critical energy release rate (G_f), otherwise known as fracture energy, can then be calculated following Equation 5.

$$G_f = \frac{W_d}{D \times t} \times 10^6 \qquad (5)$$

Where,

G_f=Critical Fracture Energy, Joules/mm

W_d = Work done during fracture, Joules

d = Specimen diameter, mm

t = Specimen thickness, mm

In general, G_f describes the rate at which cracks propagate through the tested sample and can be used, along with other fracture mechanics parameters, to define a cracking index (CT_{index}) as shown in Equations 6 and 7. Generally, higher CT_{index} values are desirable for asphalt mixtures and indicates greater cracking resistance. The relationship between CT_{index} and HMA cracking resistance can be further understood as a greater CT_{index} value was able to withstand more deformation (I_{75}), exhibited slower failure ($|m_{75}|$), and/or required more energy (G_f) to reach failure.

As reported in literature, the CT_{index} provides a greater understanding of the cracking resistance of HMA mixes and was found to strongly correlate with field cracking performance (*15*). Due to the development from fracture mechanics, it is worth noting that the IDEAL-CT analysis can be applied to IDT testing at different testing temperatures as a comparative measure.

$$CT_{index} = \frac{t}{62} \times \frac{I_{75}}{D} \times \frac{G_f}{|m_{75}|} \tag{6}$$

$$|m_{75}| = \left| \frac{P_{85} - P_{65}}{I_{85} - I_{65}} \right| \tag{7}$$

Where,

CT_{index} = Cracking test index

l_{75} = Vertical displacement when at 75% of peak load after peak, mm

G_f = Fracture Energy, J/m^2

D = Specimen diameter, mm

t = Specimen thickness, mm

$|m_{75}|$ = Absolute value of the post-peak slope at 75 percent of peak load after peak, N/m

P_{65} = Applied load when at 65% of peak load after peak, kN

P_{85} = Applied load when at 85% of peak load after peak, kN

l_{65} = Vertical displacement when at 65% of peak load after peak, mm

l_{85} = Vertical displacement when at 85% of peak load after peak, mm

Overlay Test. The Overlay Test (OT) can evaluate the cracking resistance potential of an HMA mix with an emphasis on reflective cracking [17], [29], [33], [34]. The OT operates by applying a cyclic displacement load to the upper half of the HMA sample while keeping the lower half of the HMA fixed. The OT terminates when the HMA cracking has fully propagated through the OT sample. The results are defined in terms of the number of cycles to failure, where the failure is defined as a percent reduction in initial load or when an acceptable number of cycles to failure is reached (typically 93%). In literature, HMA mixes that last over 300 cycles have been considered acceptable with respect to laboratory fatigue performance [35] and greater number of cycles to failure is desirable as this can be interpreted as a greater cracking resistance. The OT is conducted at a temperature of 25°C according to the standard specification (TxDOT-248-F). The OT applies a cyclic displacement load of 0.635 mm to an HMA specimen at a rate of 0.1 Hz (Figure 4). All HMA mixtures are compacted to a height of 115 mm and are saw cut to the proper dimensions. The OT samples are fabricated by gluing the HMA sample to a set of two steel plates with a 4.2 mm gap between plates to replicate a pre-existing crack.

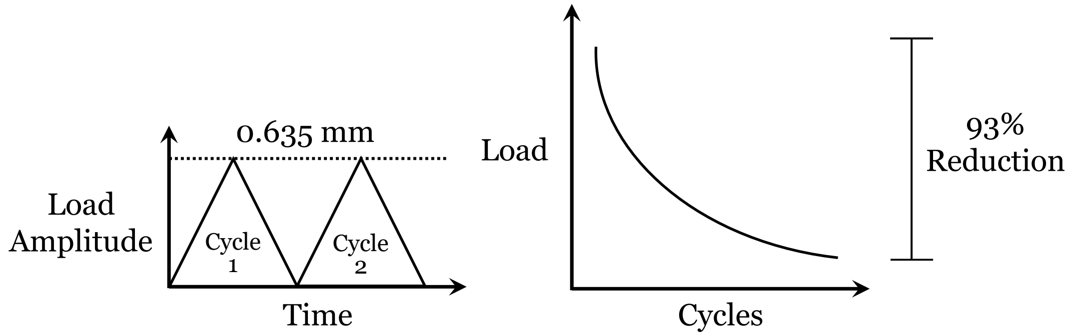

Figure 4. Illustration of the response curve (load versus cycles) and triangular loading signal associated with OT testing.

Four-Point Bending Beam Fatigue Test. The four-point Bending Beam Fatigue (BBF) test is used to evaluate the fatigue performance of HMA mixtures. The BBF test applies a cyclic displacement load at a specified loading rate to the center of the beam while fixing the end of the HMA beam. The BBF test then records the loading required to reach the specified displacement and the stress and strain are calculated using Equations 8 and 9.

$$\sigma_t = \frac{3 \times a \times P}{b \times h^2} \tag{8}$$

$$\varepsilon_t = \frac{12 \times \delta \times h}{(3 \times L^2) - (4 \times a^2)} \tag{9}$$

Where,

σ_t = Tensile stress, MPa

a = Center-to-center load spacing, mm

P = Load, N

b = Specimen width, mm

h = Specimen thickness, mm

ε_t = Tensile strain

δ = Beam deflection, mm

L = Specimen Length, mm

The flexural stiffness is then determined (Equation 10) and used to compute the normalized modulus (Equation 11). According to ASTM D7460, the normalized modulus is then used as a measure to determine when the HMA beam specimen has failed. The outcome from this test—Number of cycles to failure ($N_{f\text{-}BBF}$)—can be used as a comparative measure to evaluate the service life of HMA mixtures.

$$S = \frac{\sigma_t}{\varepsilon_t} \tag{10}$$

$$\text{Normalized Modulus (NM)} = \frac{S_i \times N_i}{S_0 \times N_0} \tag{11}$$

Where,

σ_t = Tensile stress, MPa

ε_t = Tensile strain

S = Flexural stiffness, MPa

NM = Normalized modulus

S_i = Flexural stiffness at cycle i

N_i = Number of cycles at cycle i

S_o = Flexural stiffness at initial cycle

N_o = Number of cycles at initial cycle (typically chosen to be cycle 50)

The BBF test is typically conducted according to ASTM D7460 or AASHTO T321 standards. The asphalt beam specimen is conditioned in an environmental chamber at a testing temperature of 20 ± 0.5°C. The temperature-conditioned beam is then secured in the BBF testing apparatus using four clamps that are spaced apart at a distance of approximately 4.6 in (118.5 mm). A constant-displacement load is applied to the center of the beam and is measured using a Linear Variable Differential Transducer (LVDT). The test is terminated after it reaches a specified failure criterion (i.e. flexural stiffness reduces by fifty percent).

Use of Geosynthetics in Pavement Applications

Geosynthetics are durable polymer materials used in or on soil to improve the characteristics and capabilities of soil substructures. The geosynthetics improve weak soil substructures through improved soil shear strength, greater separation between low-quality and high-quality soil layers, improved filtration (i.e. erosion control of fine soil), controlled drainage of water, containment of gases (primarily for waste management), and temperature insulation [36]. Geosynthetics can be primarily categorized into seven types—textiles, grids, nets, membranes, composites, clay liners, and foam. Three of the geosynthetic types are commonly employed to improve the strength of pavement layers—geotextiles, geogrids, and composites. These three geosynthetics types are described further in the following subsections.

Geotextiles. Geotextiles have openings (or apertures) that are very close together. They are made using synthetic polymers—polyethylene or polyester—or other materials like: nylon, fiberglass, or natural organic materials [1], [37]–[39]. The intertwining of the fabric is typically done using two different methods: woven and non-woven. Woven geotextiles are manufactured using a method where two or more strands are interlaced together. These strands are typically silt films or monofilaments, and they can be interlaced uniquely (i.e. silt with silt films) or combined (i.e. silt films with monofilaments) [39]. Woven geotextiles are preferred for locations with high design loads that requires soil stabilization, soil separation, and/or erosion control [1], [37]–[39].

Non-woven geotextiles are bonded together using chemicals/heat or needle-punching. Non-woven geotextiles are preferred for locations where weak-strong soil blending and/or erosion is a concern [1], [37]–[39]. They do not have high tensile strength, so they do not perform well when used as a soil strengthening measure. In roadway construction, non-woven geotextiles have been used in HMA overlays to improve soil separation and eliminate erosion due to water seepage. These benefits of non-woven geotextiles reduce the rate of pavement failure and increase the longevity of HMA overlays [1], [37]–[39].

Geogrids. Geogrids (mesh or nets) are similar to geotextiles, but have large openings to allow aggregate interlock and improve soil shear strength. Geogrid openings can be rectangular or triangular in shape and can vary between ½ to 2 inches wide [1], [37]–[39]. Geogrids are made from several materials including synthetic polymers, nylon, basalt, carbon, and other organic materials. Geogrids also improve soil drainage and allow for water fluctuation control. They are formed by punching plastic sheets and stretching them to the intended aperture size or through a weaving process similar to woven geotextiles.

Geocomposites. Geocomposites are a combination of all other geosynthetics types and are designed to meet situation-specific needs [1], [39]. Since geocomposites are typically constructed based on need, there is currently no common construction practice or design for these materials. Common examples of geocomposites are blanket drains and edge drains. Blanket drains are used to improve pavement base layer drainage. Edge drains are used to remove excessive lateral seepage from roadway base layers. Both geocomposite drain types consist of a geogrid (or geonet) surrounded by a geotextile filter. This system allows water to pass through, but prevents fine-grained soils from clogging [1], [39].

Mechanisms for Reinforcing Pavements using Geogrids

The primary focus of this research study is directed towards evaluating the reinforcement benefits at the airfield pavement through the use of geogrids. Geogrids are primarily used as a strength reinforcement measure as its apertures are too large to be an effective separation or filtration reinforcement method. The geogrid reinforcement can be designed to reinforce soils in one direction (uniaxial), two directions (biaxial), or three directions (triaxial), with each having their own respective advantages and disadvantages. In pavement systems, geogrids are typically installed at the subgrade-base interface, in the base layer, or at the base-surface interface. The reinforcement capabilities of geogrid have been attributed to three reinforcement mechanisms: lateral restraint, increased bearing capacity, and tensioned membrane effect [2], [5], [24].

Lateral Restraint. The primary mechanism associated with geogrids is lateral restraint or confinement. This function has been considered and used in many fields including: pavement design, retaining wall design, and a soil stabilization technique in foundation design. In flexible pavement systems, the surface layer is subjected to traffic loading and this traffic loading results in a downward stress causing the aggregates in the underlying layers to shift laterally. Over time, this process continues to develop permanent deformation on the surface layer, and results in rutting. Geogrids, however, endure the shear load and transfers it into a tensile load, which is endured by the tensile stiffness of the geogrid. The geogrid also interlocks with the aggregates increasing the sliding friction thus increasing the shear strength of the layer. This reinforcement mechanism is portrayed in Figure 5. Therefore, it is critical to choose an aperture size that corresponds to the gradation of the aggregates. Additionally, it is vital to examine the tensile stiffness, thickness, and frictional capabilities of the geogrid in order to select a geogrid that can withstand the stress and strains it will be exposed to in the field [5].

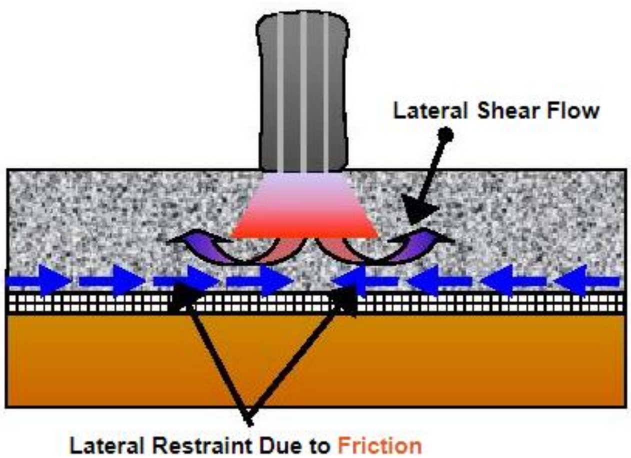

Figure 5. Representation of the lateral aggregate restraint reinforcement mechanism associated with geogrid reinforcement [5].

Increased Bearing Capacity. Another mechanism associated with the implementation of geogrids is the discontinuance it causes in the failure plane of the soil.

Typically, unreinforced pavement soil layers fail in local shear; however, the use of geogrids in pavement systems modifies the subgrade failure envelope and causes it to fail in general shear. The pavement system typically fails in the weak subgrade, but the use of geogrids shift the failure plane from the weak subgrade to the stronger base. This behavior is represented in Figure 6. In order to fail in general shear, the pavement system must undergo higher loads for longer periods of time, thus implying the implementation of geogrids results in higher shear resistance. Additionally, through the activation of its tensile stiffness, geogrids are capable of decreasing the shear stresses that are transferred to the layers below the geogrid [2], [5], [24].

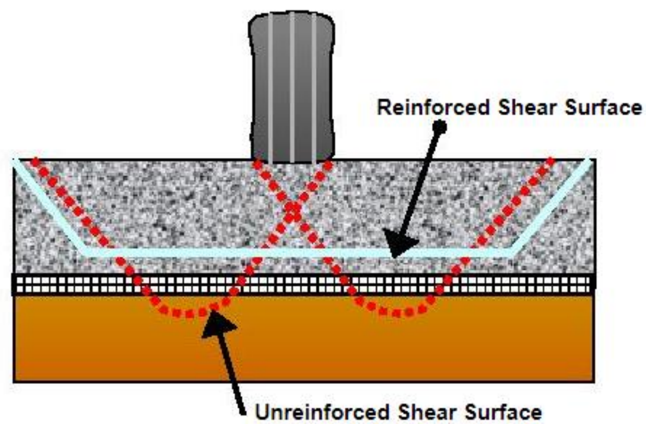

Figure 6. Representation of the improved bearing capacity reinforcement mechanism associated with geogrid reinforcement [5].

Tensioned Membrane Effect. The final reinforcement mechanism associated with geogrids is known as the tensioned membrane effect. This theory rests on the notion that the horizontal tensioning of material adds additional vertical strength. As the pavement layers bend beneath the wheel loads, the geogrid is horizontally stretched. This stretching results in additional upward support underneath the wheel load. Therefore, a greater wheel load or longer traffic times will be needed to experience high deformations or until the geogrid ruptures in tension. This reinforcement mechanism is represented in Figure 7 [2], [5].

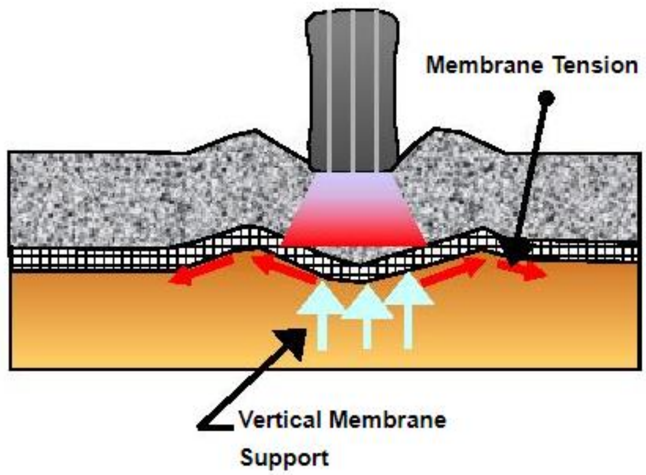

Figure 7. Representation of the tensioned membrane reinforcement mechanism associated with geogrid reinforcement [5].

Performance of Geosynthetic-Reinforced Pavements

Geogrid reinforcement has been utilized to extend the service life of pavement systems [3], [4]. Commonly, geogrids are placed in unbound pavement layers to mitigate pavement rutting and beneath HMA layers (base-HMA interface) to deter reflective cracking [1]. The literature regarding the use of geogrids as a reinforcing agent in pavement systems to improve the rutting and cracking resistance is presented in the following sections.

Impact of Geogrid Reinforcement on Rutting Performance. Geogrid reinforcement has been primarily studied and implemented for the stabilization of weak unbound pavement soil layers. Laboratory studies have been used, primarily through large scale tank testing (LSTT), to investigate effects of geogrid reinforcement in the unbound pavement layer. Tingle and Jersey [6] conducted an LSTT with a steel box measuring 1.83 meters by 1.83 meters by 1.37 meters deep. The simulated pavement system consisted of 2 layers: base course and subgrade. The base course consisted of a crushed limestone (SW-SM) base and the subgrade was made up of a high plasticity clay (CH). The target moisture content of the subgrade was to be 47% and to reach a design CBR of 1. In total, five test specimens were constructed with varying base layer thicknesses and varying geotextiles, geogrid, or geotextile-geogrid composite at the base-subgrade interlayer. The testing was conducted using a hydraulic actuator, which loaded a 305 mm diameter steel plate with sinusoidal loading of 40 kN with 0.1s load time and 0.9 second rest period. The testing found that all reinforcement tactics provided beneficial results with TBR values exceeding 1. The researchers do note that the best reinforcement method was the increased base thickness; however, that result may be skewed by the reduction in subgrade due to the confinement of the testing. The geocomposite proved to be most successful as it was able to achieve the greatest number of ESALs and able to separate the subgrade and base layers. Several other studies utilized large tank testing to replicate full-scale pavement sections in the laboratory and observed the reinforcement benefits of geosynthetics (Table 2).

Table 3

Review of Current Large-Scale Laboratory Testing

Reference Study	Geogrid Type	Geogrid Location	Findings
Perkins (1999) [40]	Biaxial Geogrid	Various locations within the base Base-subgrade interface	Geogrids performed best when placed in the base layer. Higher TBR values for geogrids with higher modulus and placed at the middle of the base layer.
Ling and Liu (2001) [41]	Biaxial Geogrid	Asphalt-base interface Asphalt-subgrade interface	Geogrids increased the bearing capacity and reduced the settlement of the layer it is placed in.
Jersey et al. (2005) [6]	Nonwoven geotextile, biaxial geogrid, and geotextile-geogrid composite	Base-subgrade interface	The main reinforcement mechanism at the base-subgrade interface is the geotextile. Geocomposites have added benefits and perform the best, but the costs may be too high.
Chen et al. (2009) [42]	Biaxial and Triaxial Geogrid	Base-subgrade interface	Geogrid reinforcement increases the area of loading, which results in less stress and deformation in the subgrade.

Table 4 (Continued)

Review of Current Large-Scale Laboratory Testing

Reference Study	Geogrid Type	Geogrid Location	Findings
Abu-Farsakh et al (2016) [43]	Triaxial Geogrid	152 mm below asphalt-base interface Base-subgrade interface	Permanent deformation in the subgrade was reduced by the triaxial geogrid reinforcement
Gu et al. (2016) [12]	Not specified	Middle of base Base-subgrade interface	The use of geogrids reduced vertical compressive stresses, but does not appear to have a significant effect on HMA tensile strains when placed at these locations.

Field testing has also been widely utilized for geogrid-reinforced pavement systems due to its similarity to implementation. Several field studies have been conducted on the rutting performance of geogrid-reinforced pavement systems [25], [38], [44]–[49]. One field test was carried out by Greene et al. [7] to determine on the effect of geosynthetics when used between the base, subbase, and subgrade layers. A highly organic soil with high swelling capacities (referred to as Torry Muck) was the subgrade soil that was reinforced with geosynthetics. The types of geosynthetics used in this study were rigid geogrids, woven geotextiles, and flexible geogrids and they were placed between the subgrade and subbase and between the subbase and the base. The duration of the field evaluation was four years and they estimated that about 1.8 million equivalent single-axle loads (ESALs) passed over the pavement during that time. The rigid geogrid and woven geotextile placed between base and subbase provided an increment in stiffness as well as allowed 2.4 more ESALs than roadway without geosynthetic support. The flexible geogrid when placed between base and subbase provided no increase in stiffness, but allowed 1.8 more ESALs than roadway without geosynthetic support. Finally, the study reported that preloading the section provided excellent results and increased the life of the experimental pavement by 11 years.

Accelerated pavement testing (APT) has also been utilized to evaluate the field performance of geosynthetic-reinforced pavement systems [2], [8]–[10], [50]–[55]. The US Army Corps of Engineers evaluated the performance of flexible pavement systems with geogrid-reinforced subgrade soil [10]. In this study, three test sections were constructed. The first section had a 2-inch AC surface layer and a triaxial geogrid between the subgrade and aggregate base. The second section had a 2-inch AC surface layer and the third section had a 3-inch AC surface layer. The last two sections had no geosynthetic reinforcement. The pavements were constructed with a high plasticity clay (CH) subgrade (CBR of 3%) and a crushed limestone aggregate base (thickness of 8 inches). The sections were tested using an HVS with bi-directional dual-wheel tandem axle load of 20,000 pounds in the first and third sections to better represent truck loading on typical traffic lanes and the second section was tested using a bi-directional dual-wheel single axle load of 10,000 pounds. The failure mode chosen was when 50% of a test section exceeded a rut depth of 1 inch. The geogrid-reinforced test section reached 100,000 ESALs without reaching the failure criteria, whereas the other two sections reached the failure criteria at approximately 10,000 (section 2) and 20,000 (section 3) ESALs. The triaxial geogrid was found to be the optimal choice as rutting and permanent surface deformation occurred at the slowest rate [10]. A similar finding was also found in another APT study that evaluated the reinforcement of base-subgrade interfaces using two different triaxial geogrid types. These sections were tested using truck tire loading applied using a Heavy Vehicle Simulator (HVS). The study concluded that sections reinforced with geogrids experienced less rutting than unreinforced sections [11].

Impact of Geogrid Reinforcement on Cracking Performance. To evaluate the impact of geogrid reinforcement on cracking performance of HMA, geogrid reinforcement has been placed as an interlayer beneath, or within, new HMA overlays to delay/prevent reflective cracking. Several studies have illustrated an increase in HMA laboratory fatigue performance from geogrid reinforcement [14], [15], [17], [38], [56]–[61]. Khodaii et al. [18] conducted a laboratory study with the goal of evaluating whether geosynthetics embedded in HMA samples at various locations impacted the cracking resistance. The researchers placed a biaxial geogrid at three locations within the HMA sample: between a damaged and new beam (replicating the interface between existing pavement and new HMA overlays), one-third of the new overlay beam (measured from the bottom), and half-depth of the new overlay beam. Additional beams were constructed without the geogrid for reference. The beams were tested through repeated loading using a hydraulic dynamic loading frame at a rate of 10 Hz and load of 100 psi (equivalent to truck loading). It was concluded that geogrids increased the overlay cracking resistance. The geogrids were most effective when placed at one-third of the depth measured from the bottom. There was little to no effect on the beam deflection and the rate of crack propagation from the type of existing damaged pavement and higher ambient temperatures increased cracking susceptibility.

Another laboratory study was conducted on the reinforcement of HMA layers with geogrids using bending beam testing [21]. The HMA beams were constructed by compacting the first asphalt beam and letting the HMA layer cool to room temperature. The HMA layers were then reheated using a blowtorch and geogrids were placed. This allowed for the geogrid coating to melt and the asphalt to become warm, which created better bonding conditions. Finally, the second asphalt beam was then compacted on top of the system reinforced HMA beams was tested using the cyclic four-point bend test and the monotonic 3 point bend test. The findings of the study suggested that the geogrids add a significant benefit in force needed to induce cracking, especially the carbon fiber geogrid. The researchers also found that four times more energy is needed for crack propagation through the carbon fiber geogrid and the second asphalt beam [21]. Similar findings were found in a later studies and further evaluation was conducted using digital image correlation (DIC) technique was used to observe the displacements and strains on the surface of the beam specimens [22], [62].

Vismara et al. [15] evaluated geosynthetic reinforcement in asphalt overlays, primarily focusing on its ability to prevent or delay reflective cracking. The test specimens were made up of two asphalt concrete beams and two types of geosynthetics were considered. Both geosynthetics were geocomposites (non-woven geotextile and fiberglass geogrid), but with two different tensile strengths, 50 and 100 kN/m^2. The geocomposites were placed in between the two asphalt concrete beams and applied with

1.6 kg/m^2 of tack coat (0.8 kg/m^2 on each side). In order to understand the effect of geosynthetics, two different laboratory tests were included. The first test investigated the bond strength at interface to better understand the relationship between the amount of reinforcement imparted by geosynthetics and their tensile strength. The results of this testing showed that a much lower peak stress was needed to cause slippage in the geocomposite-reinforced pavement specimens than the control one. The control specimen showed a brittle failure when peak forced was reached, whereas the reinforced specimen showed a ductile failure. A nonconventional fatigue test was also included in the study in which the specimens were fully supported and had a notch of 5 mm on the lower asphalt beam. The test results showed that the geosynthetics reduced crack opening displacements by approximately 20% and altered the crack propagation path through the HMA specimen. The study recommended that further research was needed to understand the optimal method of bonding geosynthetics to existing pavements for overlays [15]. Sobhan et al. [20] investigated the optimal bonding practice for geogrid reinforcement in HMA layer and the respective fatigue performance of geogrid-reinforced HMA. The researchers found that embedded geogrid in HMA is the optimal application procedure resulting in the greatest fatigue performance; however, construction feasibility needs to be investigated [20].

Finite Element Modeling of Geogrid Reinforcement

Finite element modeling (FEM) has been extensively utilized due to its ability to predict responses for a broad range of materials, loading configurations, and systems.. Several studies have been conducted on geogrid-reinforced systems for better evaluation and understanding of the overall mechanistic responses. These studies modeled the geogrid-reinforced system and found a reduction in compressive strains and, thus, an improvement in rutting performance [52], [63]–[71]. More recently however, the focus of FEM of geogrid-reinforcements has included the reinforcement in HMA layers and the overall impact on the cracking performance. These studies also vary the element type that is utilized in the FEM simulation in an attempt to further improve the accuracy of the FEM. Table 3 provides a list of recent studies the simulated geogrid-reinforced pavement systems using FEM.

Table 5

Recent Finite Element Modeling Studies on Geogrid-Reinforced HMA

Author and Year	Geogrid Element Type	Geogrid Location	Findings
Howard & Warren, 2009 [72]	Tension	Base-Subgrade Interface	Numerical modeling was not successful in predicting pavement response with geogrid reinforcement.
Moayedi et al., 2009 [73]	Membrane	Varying	Pavement system exhibited tensile strain reductions with the use of geogrid reinforcement.
Kazemian et al., 2010 [74]	Tension	Base-HMA Interface	Stiffness of geogrid helps prevent rutting in pavement and reduces subgrade settlement.
Siriwardane et al., 2010 [75]	Membrane	HMA	FEM showed no significant change in vertical stress when geogrid is placed in HMA layer.
Buonsanti & Leonardi, 2012 [76]	Membrane	HMA	Fiber glass geogrid can improve the performance of flexible pavement and can be observed using finite element method.
Huang, 2014 [77]	Solid	Base-Subgrade Interface	Approximately 50% improvement in the soft subgrade materials.
Abu-Farsakh et al., 2014 [70]	Membrane	Base-Subgrade Interface	Base reinforcement reduces compressive strain at the top of the subgrade and permanent surface deformation.
Correia et al., 2018 [78]	Solid	HMA	Reduction in tensile strains due to geogrid reinforcement. No significant change with change in tensile strength of geogrid.

Hussein and Meguid [79] conducted a parametric study to investigate the optimal FEM strategy of geogrid reinforcement. The study investigated the impact of element type, element shape, and geogrid geometry on the overall accuracy of the FEM. For this study, the geogrid was modeled assuming a nonlinear elasto-plastic constitutive model with no anisotropy. The FEM included an axisymmetric model with integrated soil particles within the geogrid apertures. To determine the impact of geogrid geometry on accuracy, the geogrid was subjected to tensile testing and was modeled using the physical geogrid dimensions (including measured aperture opening sizes) and a simplified planar prism (i.e. simple rectangular prism). The element type (membrane or solid elements) and shape (rectangular or triangular) were evaluated and validated using the experimental results from for a square footing supported by geogrid-reinforced crushed limestone soil [42]. The results of this study showed that the geogrid geometry using physical dimensions, then no calibration process is necessary. It was also found that the geogrid geometry can be simplified to a planar sheet; however, a calibration process is necessary to determine the proper thickness. With regards to element type, no significant impact of element type on the accuracy of the model was found. Finally, this study instituted a geogrid model with integrated soil particles that proved to be successful in capturing the behavior of the reinforced soil layer.

Abdesssemed et al. [80] conducted an evaluation of the deformations and stresses in different airport runway sections. A finite element model (FEM) was constructed to better understand the distribution of stresses and strains throughout the pavement system. A 3D finite element model was developed with four pavement layers—AC surface, base layer, subbase layer, and subgrade—using an eight-noded brick (C3D8) element. Each layer was defined using a linear elastic constitutive model with Young's modulus and Poisson's ratio as material inputs. The geogrid was modeled using a four-noded quadrilateral membrane (M3D4) element and implemented within the base layer. An aircraft loading was simulated using a circular tire pavement contact area with a radius of 221 millimeters and a static vertical load of 25 tons. The results of the numerical model showed a reduction in compressive and tensile strains due to the geogrid reinforcement.

Gu et al. [12] constructed a 2D axisymmetric model to simulate the responses of geogrid-reinforced unbound pavement layers. The researchers used an eight-noded biquadratic homogenous element with reduced integration to model the HMA layer, base course, and subgrade layers. The geogrid was modeled using a three-noded membrane element in an effort to simulate the tensioned membrane effect reinforcement mechanism. The contact between the geogrid and base course is modeled using the Goodman model. This model allows for the introduction of slippage, but allows for the freedom of using a fully bonded interface condition. This model also adds additional confined strength due to the shifting of the unbound aggregated through a user-made material subroutine (UMAT). This UMAT calculates an additional confined strength and then adjusts the resilient modulus of the unbound aggregate layer, accordingly. Additional geogrid and HMA material properties were determined using laboratory testing. The model was validated through a large-scale tank test. The researchers found that the geogrid significantly reduced the compressive stress and strain in the base and subgrade layers;

however, there was no impact on the horizontal tensile strain at the bottom of the surface layer.

Summary of Literature Review

A thorough review of the literature was conducted on the use of geogrids in flexible pavement systems. A majority of the research investigates the stabilization of unbound pavement layers to improve pavement rutting performance. Additionally, the use of geogrids was researched as a technique to delay or prevent cracking in HMA [13], [18], [21]–[23], [62]. The findings from the studies on geogrid-reinforced HMA pavements are as follows:

- The use of geogrids in unbound pavement layers leads to improved rutting performance [10], [11], [81].
- The use of geogrids in bound pavement layers leads to improved cracking performance in HMA mixtures [13], [18], [20], [21], [23], [62].
- The depth of geogrid embedment in HMA mixtures impacts the improvement in cracking performance [18], [20], [21].
- Several FEM approaches exist for modeling geogrid reinforcements with the most common approach being an elastic behavior model using a simplified geogrid geometry [70], [77]–[80].
- The tensile strength of the geogrid has little impact on the strain distribution in HMA mixtures [78].
- Few studies consider the cost-effectiveness of using geogrids in pavement systems [7].

Therefore, due to the limited literature on the use of geogrids in HMA layers, there is a need to extend the research of geogrid-reinforced HMA to investigate the impact of geogrids on HMA cracking performance. Geogrids vary in material properties (i.e. tensile strength, opening size, etc.), thus a preliminary study of the effects of geogrid materials on cracking performance of geogrid-reinforced HMA is required. Further, considering the performance of geogrid-reinforced HMA in extreme climatic conditions (i.e. freeze-thaw conditioning and low temperature cracking) is necessary to gain a further understanding of the cracking performance of geogrid-reinforced HMA in cold regions. It is envisioned that this study will add to current literature on geogrid-reinforced HMA and provide a greater understanding of the factors impacting the fatigue/cracking performance of geogrid-reinforced HMA.

Chapter 3

Materials and Experimental Plan

This purpose of this chapter is to define the materials (HMA mixture and geogrid types) utilized in this study. This chapter also discusses the adopted laboratory testing approach for evaluation of the fatigue cracking performance of geogrid-reinforced HMA. Finally, this study evaluates the fatigue cracking performance of geogrid-reinforced HMA under different environmental and construction conditions. Therefore, a detailed description of the mixing and compaction, sample preparation, and sample conditioning is provided in this chapter.

Materials and Mix Design

A dense-graded airfield HMA mix design was selected for this study. An airfield mix design was selected due to the lack of research into the performance of geogrid reinforcements in high-stiffness HMA mixtures. The HMA mixture was designed following similar specifications to Federal Aviation Administration (FAA) P-401. One aggregate type (diabase) and one asphalt binder (polymer-modified PG 76-22) were used to prepare a dense graded HMA airfield mix following the Superpave mix design procedure [82]. These materials were selected based on local source availability and recommendations from FAA P-401 recommendations for this region [83]. HMA samples were prepared using a Superpave Gyratory Compactor (SGC) as per AASHTO T312. In this process, the design gyration (N_{des}) was selected to be 50, which represents the loading magnitude for aircraft loads less than 60 thousand pounds (or three million ESALs) [83], [84]. The mixing and compaction temperatures for the asphalt mixes were in the range of 157-163°C, and 152-157°C, respectively. After blending the aggregates and asphalt binder, the mixtures were kept for short-term aging for 2 hours at a compaction temperature prior to the compaction. Next, the specimens were cured at a room temperature for 24 hours and then, the bulk specific gravity (G_{mb}) of the specimens were measured as per AASHTO T 166. Further, additional asphalt mixtures have also been prepared for determining the maximum specific gravity (G_{mm}) of asphalt mixtures by the Corelok method. Note that the G_{mb} of asphalt specimens has been calculated by saturated surface dry method with a view to keeping the method consistent throughout this study since the G_{mb} determination of beam specimen using corelok may not be suitable.

The results obtained from the mix design are summarized in Table 4. The target air void of the P-401 mix is 3.5 ± 0.5% and the minimum voids in mineral aggregates (VMA) is 15% as described in the FAA specification [83]. As observed, the specimens prepared with 5.3% binder content in the laboratory meet the required air void and minimum VMA limits. Thus, it can be concluded that the optimum binder content of the aggregate to prepare P-401 mix is 5.3%. Figure 8 presents the final results of the mix design (i.e., gradation and optimum binder content) and the control points for the P-401 HMA mixture.

Table 6

Mix Design Results for P-401 HMA Mixture

Trial	G_{mb}	G_{mm}	Average G_{mm}	Air void (%)	Target Air Void (%)	VMA (%)	Required VMA_{min} (%)
1	2.600	2.697	2.690	3.33	3.50±0.5	16.46	15
2	2.601	2.683		3.29		16.42	

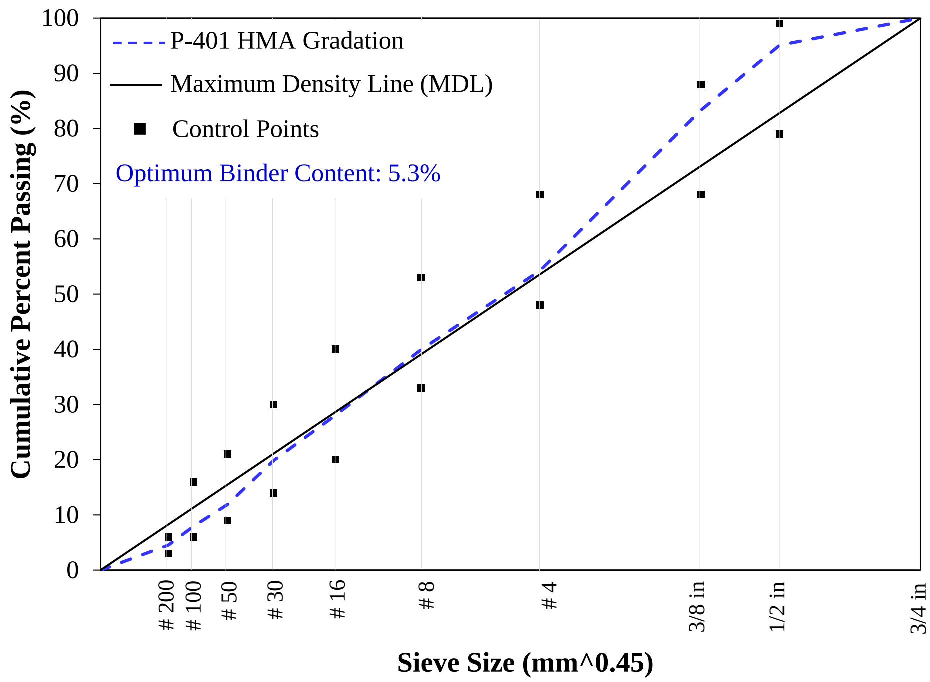

Figure 8. Gradation curve for FAA P-401 airfield HMA mix

In addition to the HMA materials, four different geogrid types were selected for the fabrication of geogrid-reinforced HMA samples. These four geogrids were selected from a larger set of geogrid materials based on their ability to withstand temperatures greater than HMA compaction (approximately 170°C). The selected geogrid types varied in aperture size, tensile strength, material type, and coating additive. Table 5 summarizes the properties of each geogrid reinforcement. Images of each geogrid type are provided in Figure 9.

Table 7

Properties of Selected Geogrid Types

Geogrid Strand Type	Aperture Size	Tensile Strength (kN/m^2)	Coating	Nomenclature
Fiberglass	25 mm x 25 mm	100	Adhesive	F-25-100-A
Fiberglass	25 mm x 19 mm	200	Adhesive	F-25-200-A
Fiberglass	30 mm x 30 mm	100	Bitumen	F-30-100-B
Basalt	25 mm x 25 mm	90	Latex	B-25-90-L

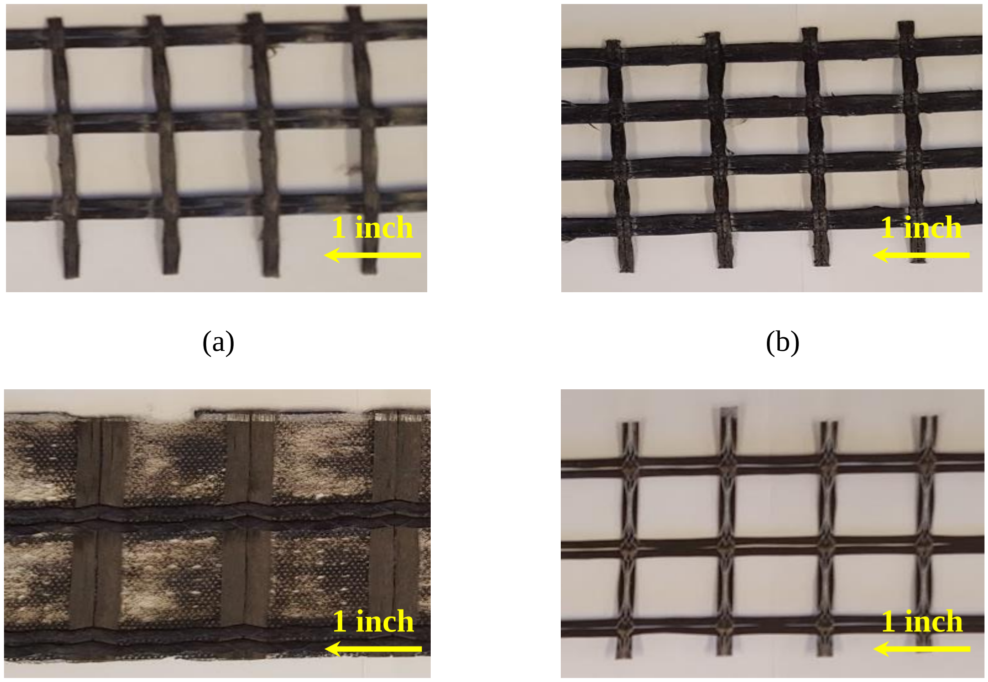

(a) (b)

(c) (d)

Figure 9. Images of each geogrid type (a) F-25-100-A, (b) F-25-200-A, (c) F-30-100-B, and (d) B-25-90-L.

Experimental Plan

The experimental plan was designed to investigate the impact of geogrid reinforcements on the fatigue performance of HMA mixtures. Additional testing combinations were included to investigate the impact of temperature (intermediate and cold temperatures), freeze-thaw cycling, compaction practices, and geogrid placement location. For each performance test, three replicates were fabricated and tested. Table 6 presents the experimental plan adopted for this study. The following subsections summarizes the performance test protocols.

Table 8

Experimental Testing Matrix

Test Method (ASTM or AASHTO procedure)	Mixtures	Temperature (˚C)	Geogrid Depth	Freeze & Thaw[1]	Replicates	Total
DCM (AASHTO T378)	5	Note 1	Half	Yes	3	30
OT (TEX-248-F)	5	4, 25	Half	Yes	3	60
ITS (AASHTO T322)	5	-20, -10, 0	Half	No	3	45
BBF[2] (ASTM D7460)	5	4, 20	Half, Third	Yes	3	144
Compaction Analysis (Delage, 2000)	5	Note 2	Half	No	3	15
Grand Total						294

[1] Freeze-thaw conditioning following AASHTO T283 protocol
[2] Tack coat method will be utilized for two geogrid types for comparison
Note 1: Temperature Sweep at temperatures of 4, 21.1, 37.8, and 54^{O}C;
Note 2: Compaction Analysis was obtained from the SGC at compaction temperature

Dynamic Complex Modulus (|E*|) Test. The |E*| test was selected to evaluate the properties of geogrid-reinforced HMA mixtures under varying temperatures and loading frequencies. Additionally, this test was selected because it is commonly employed in the design of flexible pavement systems. In this study, the DCM test was conducted at a temperature range of 4, 21, 37, and 54°C and six loading frequencies according to AASHTO T378. Three replicates were tested for each mix. Images of the prepared DCM samples with embedded geogrids are presented in Figure 10. All samples were fabricated to an air void level 7 % ± 0.5 %.

Figure 10. Images of prepared DCM samples prior to testing with embedded geogrid reinforcement and during testing in AMPT.

Overlay Test (OT). The OT was conducted at a temperature of 25°C according to the standard specification (TxDOT-248-F). In addition to the testing temperature, a low temperature (4°C) was also selected to evaluate the cracking resistance of geogrid-reinforced HMA at low temperatures. According to TxDOT-248-F, a cyclic triangular displacement load of 0.635 mm was applied to the specimen at a rate of 0.1 Hz. All HMA mixtures were compacted to a height of 115 mm and an air void level of 7% ± 0.5%. Images of prepared OT testing samples are presented in Figure 11. The test was terminated when the reactionary load (as a result of the displacement load) of the sample was reduced to 93% of its initial value or until the exceeded 2000 loading cycles.

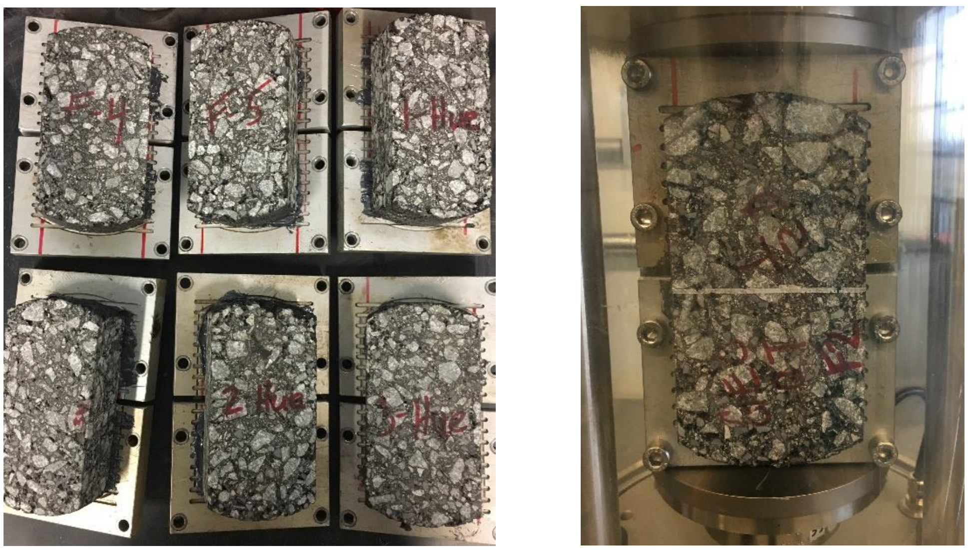

Figure 11. Images of prepared OT samples prior to testing and during testing in AMPT.

Indirect Tensile Strength (IDT) Test. The ITS test was selected in this study as it can be used as an indicator of the cracking resistance of HMA mixtures. The test was conducted at -20°C, -10°C, and 0°C to evaluate the cracking performance of the HMA mixtures at low temperatures. All samples were prepared to an air void level of 7% ± 0.5% and loaded according to AASHTO T322. Images of prepared ITS testing samples are presented in Figure 12. As mentioned previously, additional parameters can be measured during ITS testing that gives an indication of the HMA mixtures' ability to deter crack propagation. These parameters include the energy required to fully break HMA samples (fracture energy) by calculating the area beneath the load-displacement curve. Higher fracture energy values indicate slower crack propagation, and thus more ductile HMA mixtures.

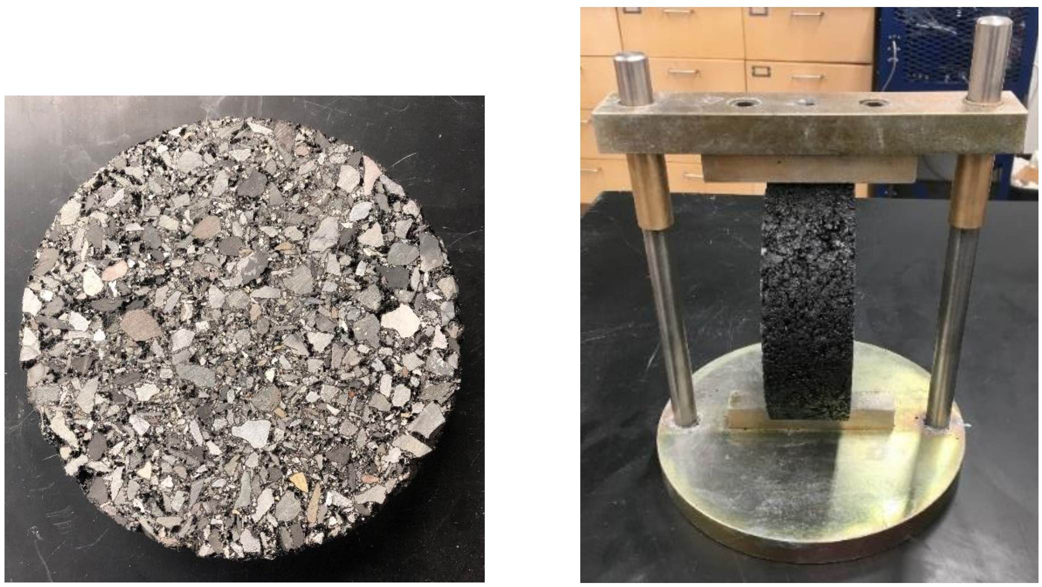

Figure 12. Images of prepared ITS samples prior to testing and ITS samples in testing jig.

Four-Point Bending Beam Fatigue (BBF) Test. For this study, the ASTM D7460 standard was adopted for evaluating the fatigue performance of HMA mixtures. This standard was selected to ensure the appropriate crack propagation behavior in geogrid-reinforced HMA mixtures. The asphalt beam specimens were prepared using the vibratory compactor to an air void level of 7% ± 0.5%. Two testing temperatures were selected (20 ± 0.5°C and 4 ± 0.5°C) to evaluate the fatigue performance at intermediate and low temperatures. Images of prepared BBF testing samples are presented in Figure 13. The test was operated as a controlled-displacement test by applying a specified beam deflection at each load cycle. The test was terminated when the normalized modulus (Equation 11) reduced by 15% of its maximum value or when the sample exceeded 1.0 million cycles.

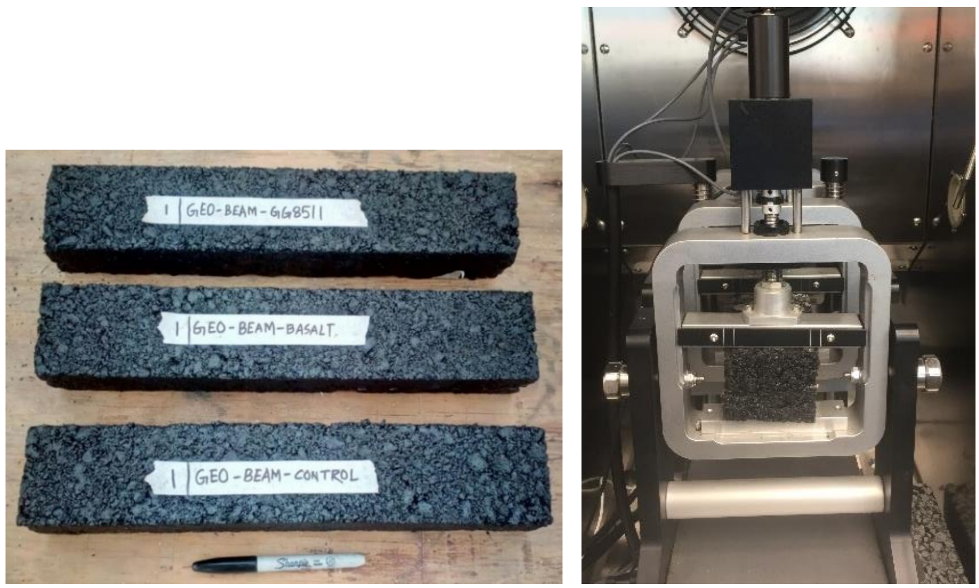

Figure 13. Images of prepared BBF samples prior to testing and during testing.

Compaction Analysis. Compaction energy is a measure of how compactable an asphalt mixture is in the field. Delage (2000) utilized the compaction curve generated by a SGC to determine the compaction energy required for asphalt mixtures. In that study, SGC compaction curves were divided into two sections: construction and traffic. The area underneath the compaction curve from the initial gyration to when the mix reached 92%

of the maximum theoretical specific gravity (G_{mm}) was considered the construction densification index (CDI).

To determine the compaction energy, control (unreinforced) and gr-HMA specimens were compacted using 150 gyrations of a SGC. All specimens were compacted at the same compaction temperature (i.e., 155°C). This high level of compaction was applied to capture the compaction behavior of geogrid-reinforced HMA mixtures. Bulk specific gravity for compacted specimens was determined according to AASHTO T166. CDI was calculated following the procedure outlined in literature [85]. Higher CDI values indicate that more energy is require to compact an asphalt mixture; thus, it is less compactable.

HMA Specimen Preparation

The basic HMA specimen preparation procedure involved the following steps: asphalt-aggregate mixing, compaction, cutting and coring, and sample conditioning. These steps are briefly discussed in this section.

Mixing and Compaction. The mixing and compaction temperatures were kept consistent with the mix design procedure. The mixing and compaction temperatures were in the range of 157 -163°C and 152-157°C, respectively. Prior to asphalt-aggregate mixing, the aggregates were pre-heated at the mixing temperature specification for at least four hours to remove any moisture and facilitate mixing. The asphalt was liquefied by heating it for approximately one hour before mixing. All the specimens were prepared using a SGC or a vibratory compactor (depending on the laboratory test) as presented in Figure 14.

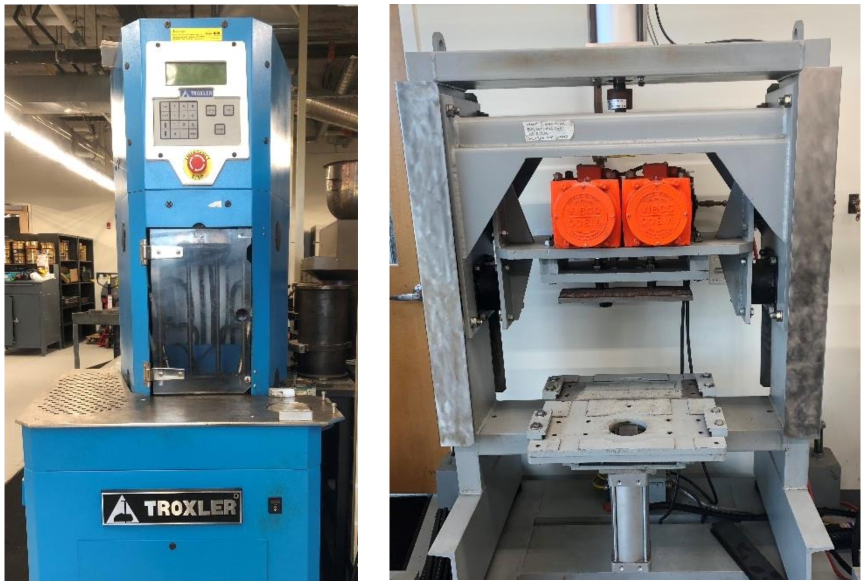

(a) (b)

Figure 14. Images of the HMA compaction equipment (a) Superpave Gyratory Compactor and (b) Vibratory Compactor.

Two compaction procedures were considered in this study. The first compaction method (hereinafter referred to as the hot compaction procedure) consisted of embedding the geogrid between two layers of HMA material and then compacting the sample. The height of each HMA layer was dependent upon the depth of geogrid embedment. Two geogrid heights were considered: half-depth (HD) and one-third depth (TD) measured from the bottom of the specimen. This procedure is similar to previous attempts in literature, in which no tack coat was used to aide in bonding [18], [20], [21]. It is noted that this method was used throughout the study for laboratory performance testing. All HMA specimens were compacted to a target AV content of 7.0% ± 0.5% to simulate field compaction levels of dense-graded HMA mixtures. A secondary compaction procedure was considered due to the uncertainty of the HMA temperature during field compaction.

The secondary compaction procedure was designed to investigate complete cooling of the bottom HMA layer (hereinafter referred to as the cold compaction procedure), with the assumption that the field compaction could potentially occur with an HMA layer that is at ambient temperature. In cold compaction procedure, the first HMA layer was placed and compacted to the target AV content of 7.0% ± 0.5%. This HMA layer was then allowed to cool to room temperature for a minimum of 24 hours. The geogrid was then applied to the first HMA layer with the aid of a tack coat. All geogrid manufacturer recommendations were followed in the application of the tack coat. Finally, the remaining HMA layer was placed and the entire specimen was compacted. It is assumed that in-situ field compaction of geogrid-reinforced HMA would occur in some intermediate temperature state between the hot and cold compaction procedures. Therefore, an evaluation of the laboratory compaction procedures will give an indication of the overall fatigue/cracking performance of geogrid-reinforced HMA. A schematic and summary of the difference in compaction procedure for geogrid-reinforced HMA is provided in Figure 15.

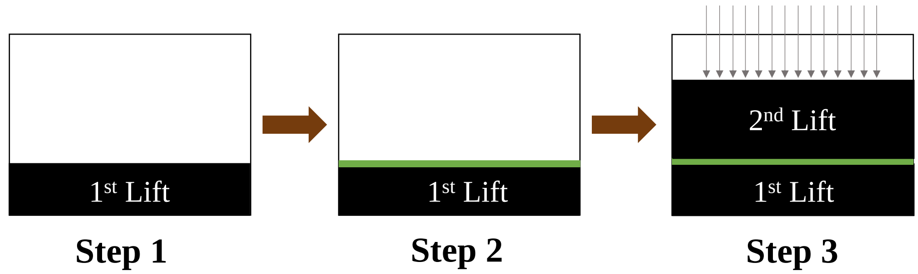

HC: Applies geogrid immediately without tack coat during Step 2

CC: Allows to cool for 24 hours and then applies tack coat during Step 2

Figure 15. Schematic of the compaction procedure used to fabricate geogrid-reinforced HMA samples.

Cutting and Coring. The Dynamic Complex Modulus (DCM), Indirect Tension (IDT), and Overlay Test (OT) were compacted using the Superpave Gyrator Compactor (SGC) with a diameter of 5.9 in (150 mm). Each test was compacted to a height of 6.9 in (175 mm), 2.9 in (75 mm), and 4.5 in (115 mm), respectively. It was necessary to target AVC above the target AVC during compaction due to differing geometry and distribution of the air voids. One DCM sample was cored and cut from each compacted specimen to a height of 5.9 in (150 mm) with a diameter of 3.9 in (100 mm). One IDT sample was cut on each side from each compacted specimen to have a remaining height of 1.7 in (45 mm). One OT sample was cut from each respective compacted sample. After the specimens were cut and cored, volumetric analysis was conducted as specified in AASHTO T166 to determine the bulk specific gravity and AVC content of each specimen. HMA specimens that failed to meet the target AVC range were discarded.

The four-point Bending Beam Fatigue (BBF) samples were compacted using a vibratory compactor. When following the hot compaction procedure, the respective width, height, and length of the compacted BBF specimen was 2.9 in (75 mm) by 2.4 in (63 mm) by 15.3 in (390 mm). When following the cold compaction procedure, the first compaction resulted in varying heights depending upon the depth of geogrid embedment. The geogrid was then placed with the aid of a tack coat, as mentioned previously. For this study, the tack coat was an asphalt emulsion (CSS-1h) commonly used in pavement construction. The amount of tack coat varied depending on the geogrid manufacturer recommendations. The final HMA layer was then placed and compacted to achieve the same final dimensions as the hot compaction procedure. Each sample was then cut to the dimensions of 2.4 in (63 mm) by 1.9 in (50 mm) by 14.9 in (380 mm). To maintain consistency, volumetric analysis was conducted on BBF specimens as specified in AASHTO T166 to determine the bulk specific gravity and AVC content of each specimen. HMA specimens that failed to meet the target AVC range of 7.0% ± 0.5% were discarded.

Sample Conditioning. This study utilized several different conditions to simulate the effects of different environmental climates on the performance of geogrid-reinforced HMA. A majority of fatigue test protocols investigate the fatigue/cracking performance at intermediate temperatures (20°C to 25°C). The samples were conditioned at this temperature for a period of two to four hours and then subjected to their respective performance test. In an effort to investigate the fatigue/cracking performance for cold regions, the tests were also conducted at colder temperatures (4°C or below). This temperature was selected because of its high impact on HMA modulus and as it is also included in the temperature sweep of the DCM test for comparison purposes. Samples subjected to fatigue/cracking tests at 4°C or below were conditioned for approximately 24 hours before testing to ensure they reach temperature.

In addition to temperature variation, the impact of freeze-thaw cycling on the fatigue/cracking performance of geogrid-reinforced HMA mixtures was investigated. AASHTO T283 was used as the procedure to simulate freeze-thaw cycling. Each HMA sample was subjected to one freeze-thaw cycle in which the sample was first saturated to a level of 70% to 80% using a vacuum pump to remove the air. The sample was then placed in an environmental chamber at -18°C for a minimum of 16 hours. The samples were then thawed for 24 hours in a heated water bath at a temperature of 60°C. Images of the vacuum saturation tank and the heated water bath are provided in Figure 16. After one full conditioning cycle, the samples were allowed to dry and cool to room temperature for a minimum of 24 hours before testing. After drying, the sample was reconditioned at the appropriate testing temperature to prepare for performance testing.

(a) (b)

Figure 16. Images of the HMA freeze-thaw cycle equipment (a) vacuum saturation tank and (b) heated water bath.

Chapter 4

Laboratory Results and Analysis

The purpose of this chapter is to discuss the results of laboratory-tested fatigue/cracking performance of geogrid-reinforced HMA mixtures. This chapter presents the laboratory results on the impact of geogrid-reinforced on HMA fatigue cracking performance, the effects of freeze-thaw conditioning, and the effects of different compaction procedures on the fatigue cracking performance of geogrid-reinforced HMA.

Impact of Geogrid Reinforcement on HMA Fatigue Cracking Performance

As mentioned previously, the $|E^*|$ test is capable of evaluating the viscoelastic response of HMA materials. In addition to this, the $|E^*|$ test has been used as an indicator of HMA fatigue performance by quantifying the $|E^*|$ at the high frequencies. As a comparable measure, greater |E*| values at high frequencies are indicative of brittle HMA mixtures, whereas lower |E*| values at high frequencies are indicative of more ductile HMA mixtures. It is desirable for HMA mixes to have lower |E*| values at high frequencies, as a more ductile failure response is desirable in pavement systems [30].

For this study, a master curve of the DCM $|E^*|$ data was fitted to a sigmoidal function at a reference temperature of 21.1°C using a polynomial time-temperature superposition shift function [31], [86], [87]. These fitting functions are presented in Equations 12 through 14 and are found to be the most suitable functions for the fitting of |E*| of HMA mixtures [31].

$$\text{Log}|E^*| = \delta + \frac{\alpha}{1+e^{\beta+\gamma(\log(t_r))}} \tag{12}$$

$$\text{Log a}(T_i) = \text{a}T_i^{\,2} + \text{b}T_i + c \tag{13}$$

$$\text{a}(T_i) = \frac{t}{t_r} \tag{14}$$

Where,

t_r = Reduced time of loading at reference temperature

δ = Minimum value of |E*|, MPa

$\delta + \alpha$ = Maximum value of |E*|, MPa

β, γ = Fitting parameters for sigmoidal function

a(T_i) = Shift factor as a function of temperature

T_i = Temperature of interest, ^{o}F

a, b, and c = Fitting parameters for second order polynomial function

t = Time of loading at desired temperature

An example of the fitting procedure is presented in Figure 17. Figure 17a presents a representation of raw |E*| data with respect to the final fitted master curve. Figure 17b presents the |E*| raw data after applying the shift function with its respective master curve. The master curve is then fitted to the |E*| raw data to minimize the error between the |E*| raw data and the fitted sigmoidal function. A similar procedure was followed for the phase angle of each HMA mixtures. The DCM phase angle data was fitted to a Guassian function master curve at the same reference temperature. This function was found to be suitable for HMA mixtures in literature [88]. Figure 18 presents the $|E^*|$ and ϕ

master curves for all five HMA mixtures—unreinforced and four geogrid-reinforced HMA mixtures—considered in this study. All |E*| and φ master curves were fit within a 2.5 average percent error, with the greatest error being 2.01% (φ master curve for F-25-200-A).

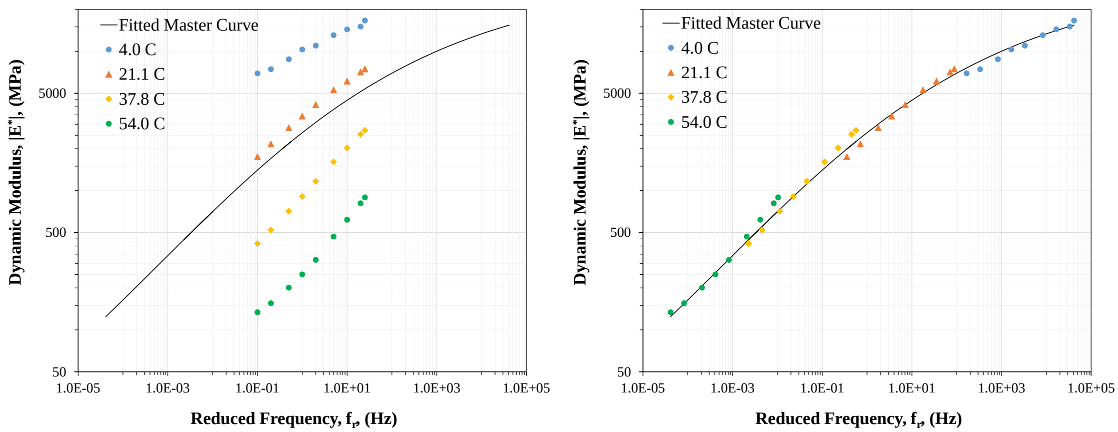

Figure 17. Representation of the fitting process of the procedure used to fit |E*| data to sigmoidal function

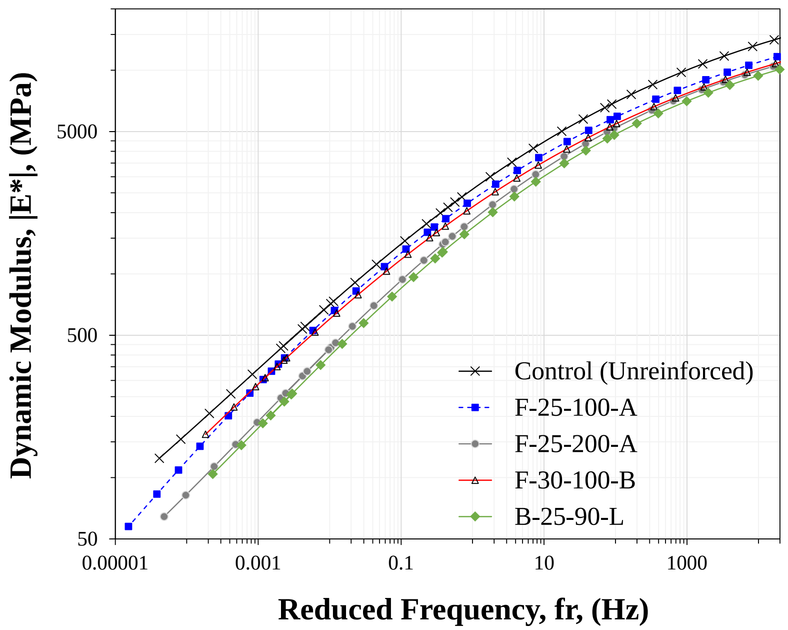

(a)

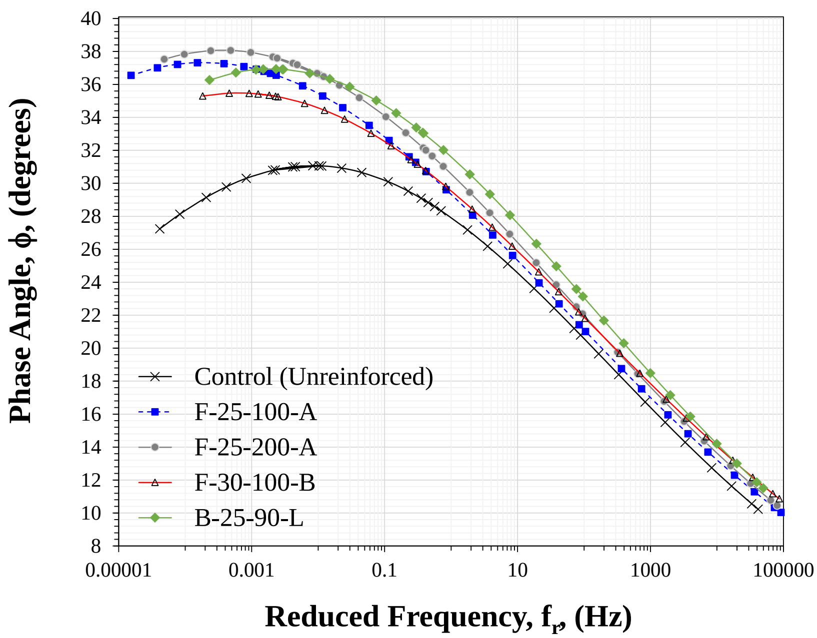

(b)

Figure 18. The (a) Dynamic modulus master curve and (b) phase angle master curve for geogrid-reinforced HMA and control HMA mixtures at 21.1ºC

The |E*| testing showed that the |E*| values for geogrid-reinforced HMA mixtures were similar to the unreinforced HMA mixture (within 20% of the unreinforced |E*| values). This is visually evident from Figure 18a, where it can be observed that the $|E^*|$ values for all geogrid-reinforced HMA mixtures were similar to or lower than that of the control (unreinforced) mixture. Further, the two geogrid types—B-25-90-L and F-25-200-A—exhibited the lowest |E*| values in the high frequency range of values (greater than 10 Hz). As mentioned previously, a lower |E*| value in the high frequency range is indicative of greater fatigue resistance [30]. Thus, these two geogrid types—B-25-90-L and F-25-200-A—show the greatest potential for having better fatigue performance. In addition to the |E*| findings, it can also be observed from Figure 18b, that the ϕ values were greater than the control (unreinforced) HMA mixture. A greater phase angle indicates greater viscous behavior in the HMA mixture and has been incorporated into alternative |E*| analysis procedures for better quantification of the fatigue resistance of HMA mixtures [30].

As stated previously, the $|E^*|$ and ϕ can be used to determine the loss modulus (E''), as shown in Equation 2. The loss modulus, also known as the Fatigue Factor (FF), has also been previously used to predict the fatigue performance of HMA mixtures [30], [89], [90]. As stated in literature, a lower FF indicates greater fatigue performance [30]. Therefore, the FF was calculated in this study for each HMA mixture—one control (unreinforced) and four geogrid-reinforced HMA mixtures—at the reference temperature of 21.1°C. The results of the FF analysis are presented in Figure 19.

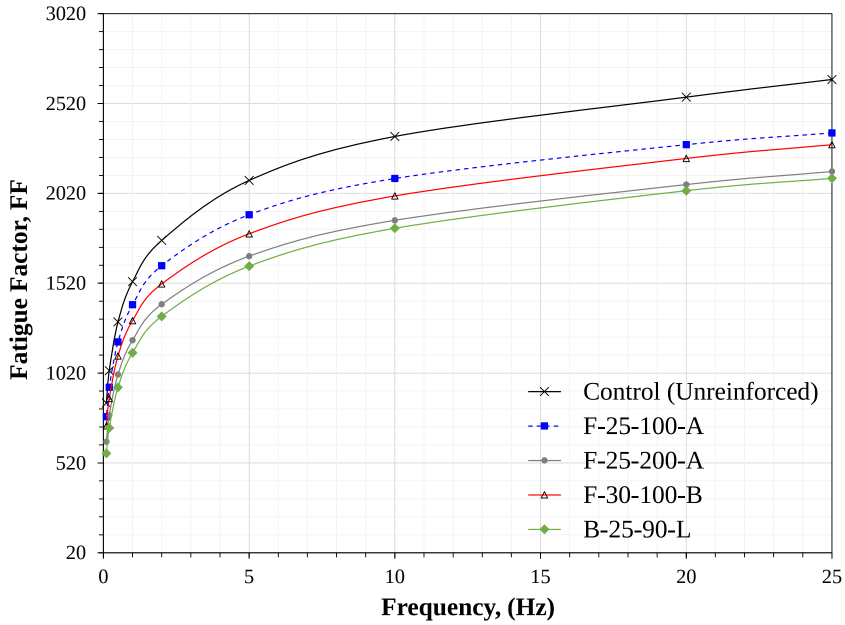

Figure 19. Results of the DCM fatigue factor analysis for geogrid-reinforced HMA and control HMA mixtures at 21.1ºC

As can be observed from Figure 19, the control (unreinforced) HMA mixture had greater FF values when compared to all other geogrid-reinforced HMA mixtures with 17.5% greater FF values, on average, for all testing frequencies at 21.1˚C. The FF results agree with the findings from the |E*| values, where geogrids show the potential for improving the resistance of these mixtures to fatigue cracking. Though this evaluation was conducted under compressive loading, the findings also agree with previous laboratory studies using flexural testing [18], [20], [21]. Figure 19 also shows that the type of geogrid used for reinforcing HMA mixtures has an impact on the FF and fatigue cracking susceptibility of HMA mixtures. The FF indicated that two geogrid types—B-25-90-L and F-25-200-A—were the best at improving the fatigue resistance of asphalt mixtures These geogrid-reinforced HMA mixtures showed 24.3% lower FF values, on average, than the unreinforced HMA mixture, across all loading frequencies considered at 21.1°C.

The observed behavior from |E*| testing (lower |E*| values and higher phase angle) may be a result of testing limitations. From observation during testing, the difference in |E*| between geogrid-reinforced HMA mixes may be due to different strand redistributions under the compressive loading associated with |E*| testing. For example, under compression, one geogrid type may redistribute the fiberglass strands to a more flat surface (lower geogrid thickness) under compressive loading, whereas another geogrid type may resist the redistribution of strands leading to less geogrid compression. In both scenarios, the HMA mixtures may intrinsically have similar |E*| values but the geogrids are showing different amounts of overall compression. Thus, the |E*| testing is measuring different |E*| and φ values. Therefore, other laboratory tests need to be considered to quantify the fatigue cracking resistance of geogrid-reinforced HMA mixtures.

In addition to |E*| testing, the OT was conducted on all HMA mixtures at a temperature of 25°C to evaluate the cracking performance of geogrid-reinforced HMA mixtures. This testing temperature has been readily used for the OT and is recommended in the testing protocol [17], [33]. In addition to the intermediate testing temperature, a low testing temperature (4°C) was also utilized. This is because HMA cracking is most predominant at intermediate and low temperatures and it would be beneficial to gain a greater understanding of the cracking resistance of geogrid-reinforced HMA at both temperatures. Both testing conditions (intermediate and low temperature) were subjected to equivalent displacement loads of 0.635 mm according to the testing standard (Tex-248-F). The results of the OT at 25°C and 4°C are presented in Figure 20.

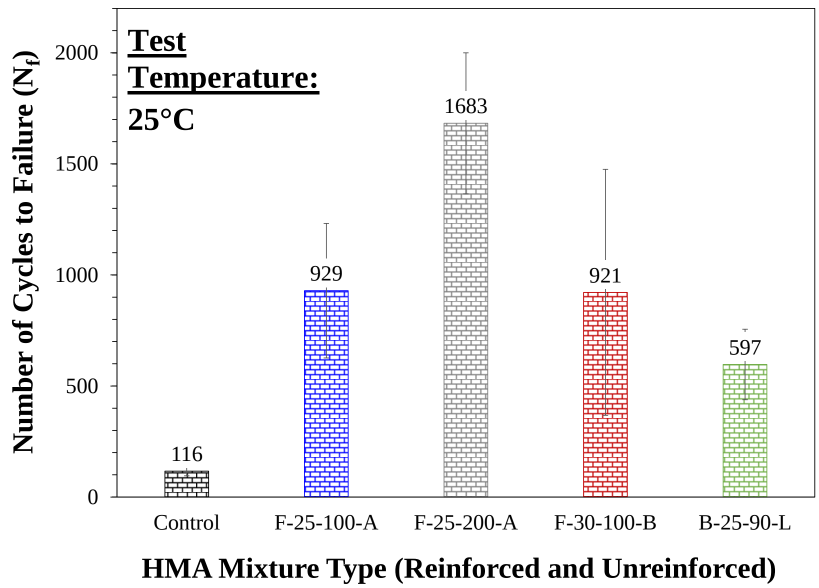

(a)

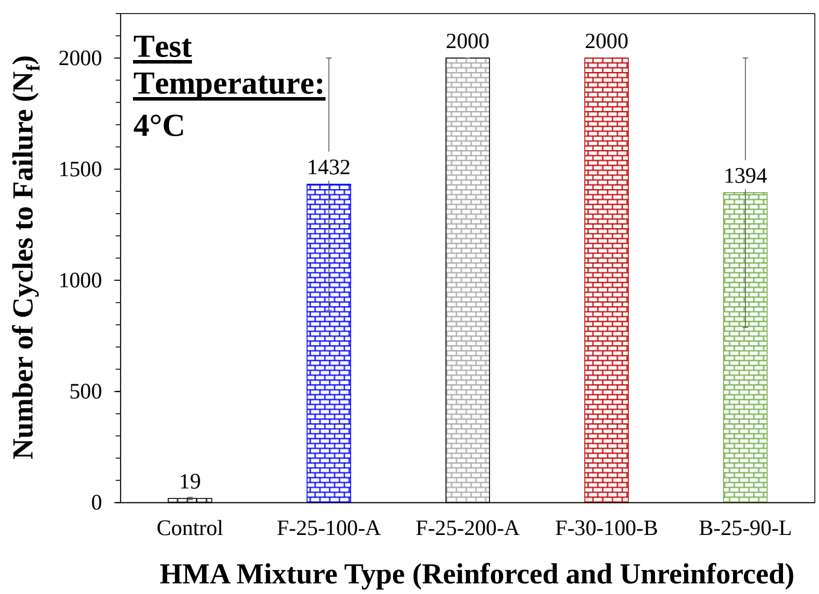

(b)

Figure 20. Results of the OT test for the control (unreinforced) and geogrid-reinforced HMA mixtures at (a) 25°C and (b) 4°C.

As can be observed in Figure 20a, all geogrid-reinforced HMA mixtures showed an average number of OT cycles to failure ($N_{f\text{-}OT}$) greater than the unreinforced HMA mixture with an average improvement in $N_{f\text{-}OT}$ of 8.88 times across all geogrid types. This finding indicates that geogrid-reinforced HMA mixtures exhibit higher cracking resistance, which can lead to an increased pavement service life. The $N_{f\text{-}OT}$ also showed the potential to be dependent on the type of geogrid used within the HMA sample. From Figure 20a, it can be observed that the geogrid with the greatest tensile strength (F-25-200-A) exhibited the greatest resistance to HMA cracking with an improvement in $N_{f\text{-}OT}$ of 14.46 times, on average. This finding agrees with the mechanisms associated with HMA cracking as the geogrid type with high tensile strength (F-25-200-A) is more capable of withstanding the greater loading, located at the crack tip, prior to degradation.

Under low temperature conditions (Figure 20b), all geogrid-reinforced HMA mixtures also showed an average number of OT cycles to failure ($N_{f\text{-}OT}$) greater than the unreinforced HMA mixture with an improvement in $N_{f\text{-}OT}$ of 91.43 times, on average. This finding agrees with the OT at intermediate temperatures in which all geogrid-reinforced HMA mixtures showed greater $N_{f\text{-}OT}$ compared with the unreinforced HMA mixture. It is evident, however, the improvement in $N_{f\text{-}OT}$ at low temperature due to geogrids (91.43) was much greater than the improvement observed at intermediate temperatures (8.88). The major improvement in $N_{f\text{-}OT}$ for geogrid-reinforced HMA mixtures at cold temperatures was unexpected as the stiffness and brittleness of HMA mixtures increases as temperatures decreases due to the viscoelastic nature of asphalt. This rationale is evident in the findings of the unreinforced HMA mixture in which the

$N_{f\text{-}OT}$ at the intermediate testing temperature (116 cycles) was greater than the $N_{f\text{-}OT}$ at the cold testing temperature (19 cycles). The response behind this phenomenon may be due to the complementing properties of both materials (HMA and geogrids). The HMA materials exhibit high stiffness and low phase angles at low temperatures (as evident in |E*| results). Thus, the HMA is more likely to return to its original mechanistic state at low temperatures and behave like an elastic material. In contrast to these beneficial properties, HMA exhibits a more brittle behavior and has a lower tensile strength limit at low temperatures, which results in faster HMA cracking at cold temperatures. The geogrid, however, which is modified to have high tensile strength properties and is not temperature-dependent, is potentially able to counteract the decrease in the tensile strength limit of HMA. Therefore, the geogrid-reinforced HMA material is more capable of returning to its original state after loading at low temperatures without the negative effect of a lower tensile strength threshold.

This rationale was further justified by the fact that several geogrid-reinforced HMA samples were terminated due to reaching the maximum number of OT cycles rather than reaching the appropriate reduction in load. Table 7 presents the number of samples that reached the maximum number of OT cycles for each mixture at each temperature.

Table 9

Number of Samples that Reached Maximum Number of OT Cycles for each HMA Mixture at each Testing Temperature

Test Temperature: 25ºC			**Test Temperature: 4ºC**		
HMA Mixture	Number of samples that reached maximum OT cycles	Total samples tested	HMA Mixture	Number of samples that reached maximum OT cycles	Total samples tested
Control (Unreinforced)	0	3	Control (Unreinforced)	0	3
F-25-100-A	0	3	F-25-100-A	2	3
F-25-200-A	2	3	F-25-200-A	3	3
F-30-100-B	1	3	F-30-100-B	3	3
B-25-90-L	0	3	B-25-90-L	2	3

From Table 7, it can be seen that at both intermediate and low temperature testing, some geogrid-reinforced HMA samples did not reach complete failure. It was also found that more OT samples did not reach complete failure at the low testing temperature. As mentioned previously, this may be due to an overall increase in tensile strength of the mixture from geogrid reinforcement.

The impact of geogrids on HMA cracking performance depends on the properties of the HMA and the geogrid. The quantification of this behavior is difficult because the geogrid properties are not fully initiated until the crack tip reaches the geogrid. The state at which the crack tip reaches the geogrid is difficult to determine, as cracking in HMA is not commonly visible until many micro-cracks have been developed. In an effort to partially alleviate this limitation, an investigation was conducted on the material response with time (load versus time curve) obtained during testing. Then, a thorough visual evaluation was conducted on the OT samples after testing. The visual observations were then compared with the load versus time curves obtained during testing. Representative load versus time curves for each HMA mixture considered are presented in Figure 21.

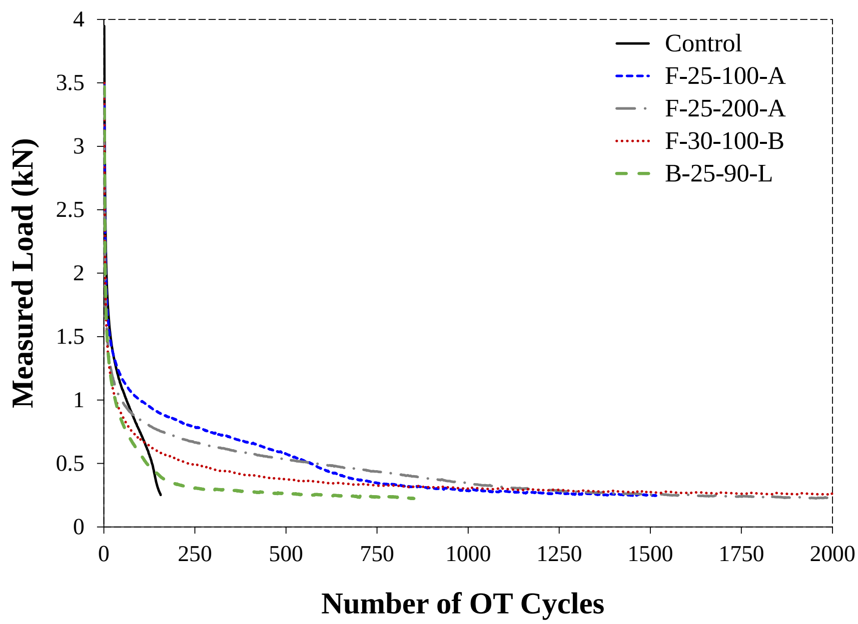

Figure 21. Representative load vs. number of loading cycles curves obtained during OT testing.

As can be seen from Figure 21, the unreinforced and geogrid-reinforced HMA mixes exhibited similar responses during the initial OT load cycles (less than 100 OT cycles). During the early portion of testing, all mixes exhibit a sudden drop in load indicating the appearance and propagation of cracking through the OT sample. The unreinforced HMA mixtures showed a continuance in the sudden load drop resulting in a rapid brittle failure. The geogrid-reinforced HMA mixtures, however, were capable of elongating the $N_{f\text{-}OT}$ as the OT sample approached failure. This finding is evident in the flattening of the load versus number of OT cycles in Figure 21 and is indicative of deterred or slowed crack propagation.

To further investigate the cracking behavior of geogrid-reinforced HMA, a visual inspection was then conducted on the OT samples to further understand the crack propagation behavior of geogrid-reinforced HMA. Each sample was examined to investigate any discontinuities or alterations in the crack propagation path due to the geogrid reinforcement. This observation led to two distinct observations (i) full vertical crack propagation and (ii) arrested crack propagation path. Images of each crack propagation observation is presented in Figure 22. Based on observation during testing, the OT samples exhibiting the full vertical crack propagation path showed to have lower $N_{f\text{-}OT}$. This crack propagation path is expected based on previous use of the OT in literature [17], [33], [34] and is evident in Figure 22a. The arrested crack propagation path stopped the crack propagation at the location of the geogrid (Figure 22b). This phenomenon of altering the crack propagation path in HMA materials agrees with previous studies on geogrid-reinforced HMA [21]. The crack deterring (or arresting) characteristics of geogrid-reinforced HMA may potentially be the reason for the flattening of the load versus number of OT cycles curve Figure 21 and a greater $N_{f\text{-}OT}$.

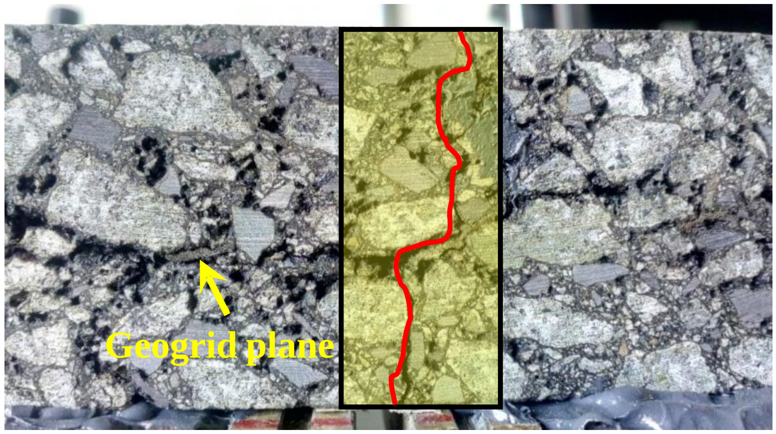

(a)

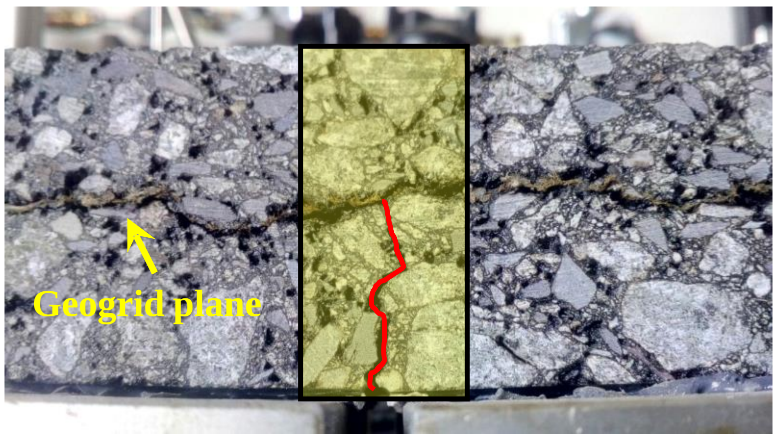

(b)

Figure 22. Illustration of crack propagation paths as identified from OT testing; (a) completely vertical propagation path and (b) vertical-lateral crack propagation path.

The Indirect Tensile Strength (ITS) test is another laboratory test capable of evaluating the cracking resistance of HMA mixtures at low temperatures. Due to the temperature flexibility of this test, temperatures below freezing (0, -10, and -20°C) were used to determine the cracking resistance of geogrid-reinforced HMA mixes in extreme low temperatures. As discussed previously, the ITS test records the loads and measured displacements during testing. Based on these measurements, several parameters can be determined. A representative load-displacement graph obtained during ITS testing is presented in Figure 23.

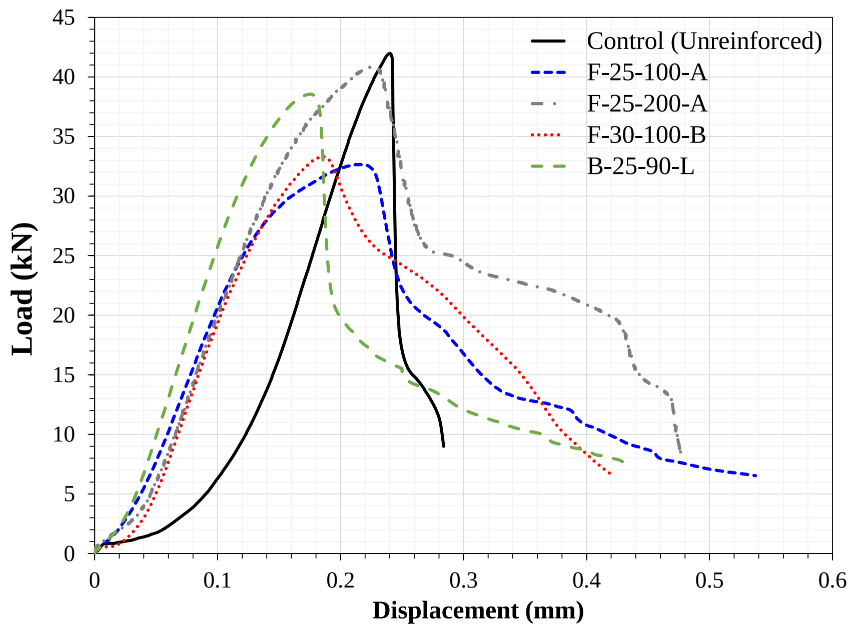

Figure 23: Representative ITS load-displacement curves for unreinforced and geogrid-reinforced HMA mixtures.

Utilizing the load-displacement graphs presented in Figure 23, several parameters can be determined to evaluate the cracking resistance of HMA mixtures. One measure that can easily be determined is the Indirect Tensile Strength (ITS) value for each HMA mixture. As discussed in previous sections, the ITS values can be calculated using the peak load during testing and the specimen dimensions. The ITS values were determined at 0˚C, -10˚C, and -20˚C for the control (unreinforced) and geogrid-reinforced HMA mixtures and are presented in Figure 24.

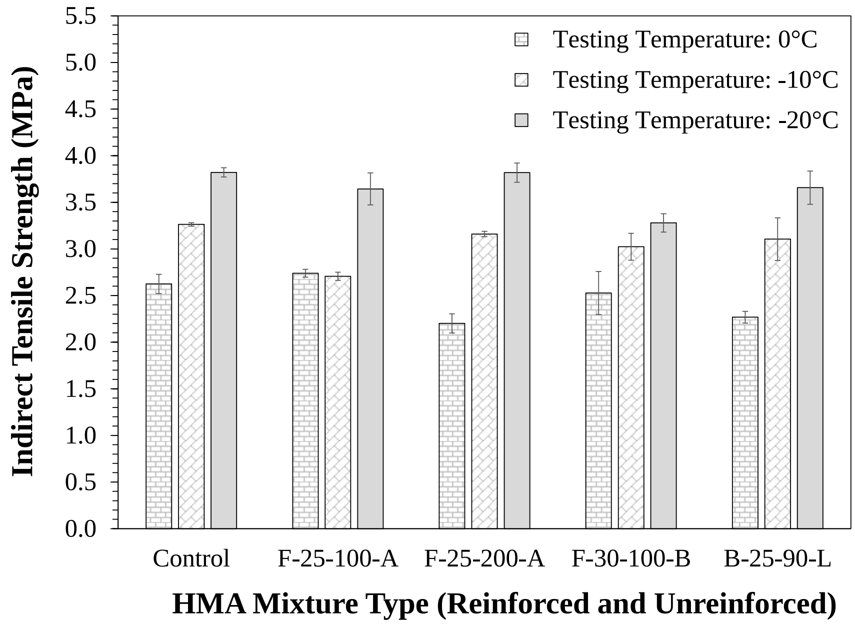

Figure 24: The indirect tensile strength (ITS) values for control (unreinforced) and geogrid-reinforced HMA mixtures at 0˚C, -10˚C, and -20˚C testing temperatures.

From Figure 24, it can be observed that the control (unreinforced) mixture had comparable ITS values (within 0.55 MPa) to those obtained for geogrid-reinforced HMA mixtures. These results suggest that the ITS cracking measure is unable to identify a difference between the cracking characteristics of the control (unreinforced) mixtures and the geogrid-reinforced HMA mixtures. These results are expected based on visual inspection of the peak loads in Figure 23, as the geogrid-reinforced HMA mixtures exhibited similar or lower peak load values than the control (unreinforced) HMA mixture. Figure 24 also shows that all mixtures followed the pattern of increasing ITS values with decrease in testing temperature. It is also observed that the ITS values decrease with an increase in temperature. This pattern was expected due to the increased HMA stiffness (and resulting higher peak loads) at lower temperature conditions.

Though the ITS values (Figure 24) were similar between the control (unreinforced) and geogrid-reinforced HMA mixtures, the post-peak performance of each HMA mixture differed. This is evident in the rate at which the load reduced in Figure 23 after the peak-load was attained. The ITS value, however, is incapable of evaluating the post-peak performance of HMA mixtures as it is only dependent on the peak load (Equation 4). Therefore, alternative measures have been developed to quantify both pre-peak and post-peak load performance. One measure that has been utilized is the Fracture Energy (G_f). The G_f of HMA mixtures are determined by calculating the area beneath the load-displacement curve and normalizing by the cross-sectional area. The calculation of G_f has been presented previously in Equation 5 and graphically represented in Figure 3. The G_f values for the control (unreinforced) and geogrid-reinforced HMA mixtures at all ITS testing temperatures are presented in Figure 25.

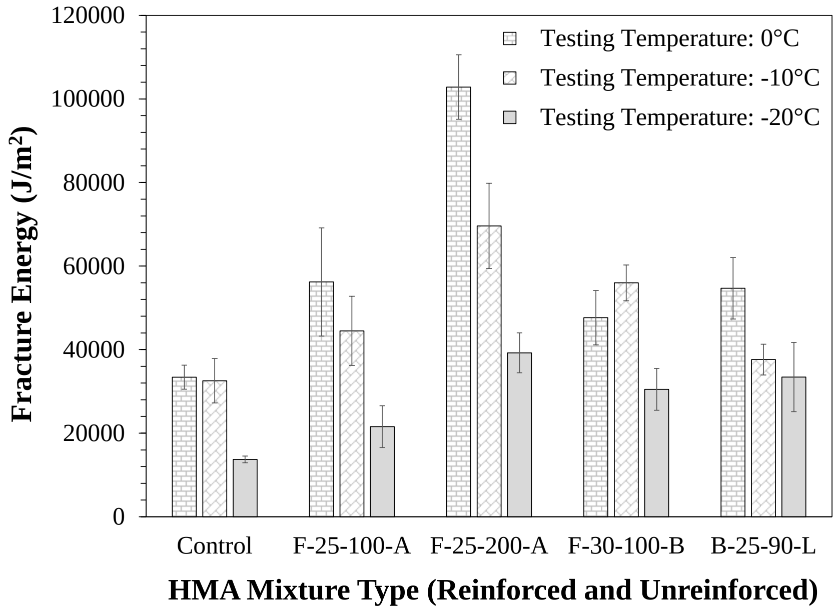

Figure 25: The fracture energy (G_f) values for control (unreinforced) and geogrid-reinforced HMA mixtures at 0°C, -10°C, and -20°C testing temperatures.

From Figure 25, it can be generally observed that the G_f values for geogrid-reinforced HMA mixtures were higher than those of the control (unreinforced) mix across all ITS testing temperatures. Thus, more energy is required to fail a geogrid-reinforced HMA sample compared to the unreinforced HMA sample. This finding can be attributed to the slower load reductions in the geogrid-reinforced HMA samples as evidenced previously in the representative load-displacement curves (Figure 23). The slower load reductions can be interpreted as reduced crack propagation and a longer HMA service life, which agrees with the findings from the OT. The G_f values also appeared to be dependent on the geogrid type utilized within HMA mixtures; especially at 0°C and -20°C. The geogrid-reinforced HMA mixtures prepared using high tensile strength geogrids had the highest fracture energy values (Figure 25).

The G_f value is only one measure from ITS testing used to evaluate cracking resistance of HMA mixtures. Additional ITS test measures have been developed and correlated with field performance [32]. These measures have been described previously in Figure 3 and Equations 6 and 7. Though these measures have been developed for intermediate temperatures, the same concepts are applicable to low temperature testing, as well. The additional cracking parameters obtained in this study are presented in Tables 8 through 10 for each HMA mixture considered and each ITS testing temperature.

Table 10

Additional Cracking Parameters Obtained From ITS Testing at -20°C

HMA Mixture	$\|m\|_{75}$	COV	Strain Tolerance (I_{75}/D)	COV	CT_{index}	COV
Control (Unreinforced)	97.8	27.6%	0.0157	4.5%	0.4	77.2%
F-25-100-A	35.6	47.8%	0.0139	16.2%	4.4	109.6%
F-25-200-A	19.2	90.3%	0.0183	7.0%	40.8	75.6%
F-30-100-B	48.7	109.7%	0.0138	13.2%	14.9	92.9%
B-25-90-L	75.7	63.2%	0.0136	6.2%	4.2	40.8%

Table 11

Additional Cracking Parameters Obtained From ITS Testing at -10°C

HMA Mixture	$\|m\|_{75}$	COV	Strain Tolerance (I_{75}/D)	COV	CT_{index}	COV
Control (Unreinforced)	19.3	30.6%	0.0188	27.5%	22.4	11.5%
F-25-100-A	9.6	77.8%	0.0256	3.2%	129.9	74.0%
F-25-200-A	4.8	62.8%	0.0293	1.6%	443.5	19.6%
F-30-100-B	11.7	44.6%	0.0220	11.5%	86.3	38.5%
B-25-90-L	13.4	24.9%	0.0218	11.4%	38.7	22.5%

Table 12

Additional Cracking Parameters Obtained From ITS Testing at 0°C

HMA Mixture	$\lvert m\rvert_{75}$	COV	Strain Tolerance (I_{75}/D)	COV	CT_{index}	COV
Control (Unreinforced)	17.8	3.8%	0.0229	64.1%	41.7	33.6%
F-25-100-A	8.0	16.3%	0.0302	52.3%	150.3	41.4%
F-25-200-A	2.9	49.5%	0.0477	6.4%	1426.1	3.3%
F-30-100-B	11.0	51.7%	0.0290	7.4%	106.3	31.7%
B-25-90-L	6.8	20.3%	0.0388	31.3%	197.4	17.7%

The OT and ITS test are primarily utilized to investigate the cracking resistance of HMA mixtures because these laboratory tests initiate cracking early during testing [29], [32]. The four-point Bending Beam Fatigue (BBF) test was used to evaluate the fatigue performance of unreinforced and geogrid-reinforced HMA mixtures under flexure. The outcome from this test—Number of cycles to failure ($N_{f\text{-}BBF}$)—can be used as a comparative measure to evaluate the fatigue service life of HMA mixtures. As mentioned previously, the flexural stiffness and normalized modulus are computed using Equations 10 and 11.

For this study, the BBF tests utilized testing temperatures at 20°C and 4°C. The intermediate temperature was selected based on the standard procedure outlined in ASTM D7460. The additional temperature (4°C) was selected to investigate the fatigue performance of geogrid-reinforced HMA at low temperature testing. This temperature also coincides with the low temperature range selected for the DCM temperature sweep and the OT in order to facilitate comparisons. The BBF tests at 20°C and 4°C were operated with peak to peak strains of 725 and 350 microstrains at a loading frequency of 10 Hz, respectively. Varying peak to peak strains were necessary because of the high stiffness of the HMA at colder temperatures. Figure 26 presents the BBF number of cycles to failure at the intermediate and low testing temperature.

At intermediate temperatures, the number of BBF number of cycles to failure ($N_{f\text{-}BBF}$) for geogrid-reinforced HMA mixtures was, on average, 1.71 times greater than that of the unreinforced HMA mixture across all geogrid types and embedment depths. This is evident from Figure 26a, where a majority (five out of eight) of geogrid-reinforced HMA mixtures had a greater average $N_{f\text{-}BBF}$ compared with the unreinforced HMA. Therefore, based on the laboratory BBF performance, the geogrid-reinforced HMA mixtures showed greater fatigue resistance compared with the unreinforced HMA mixture.

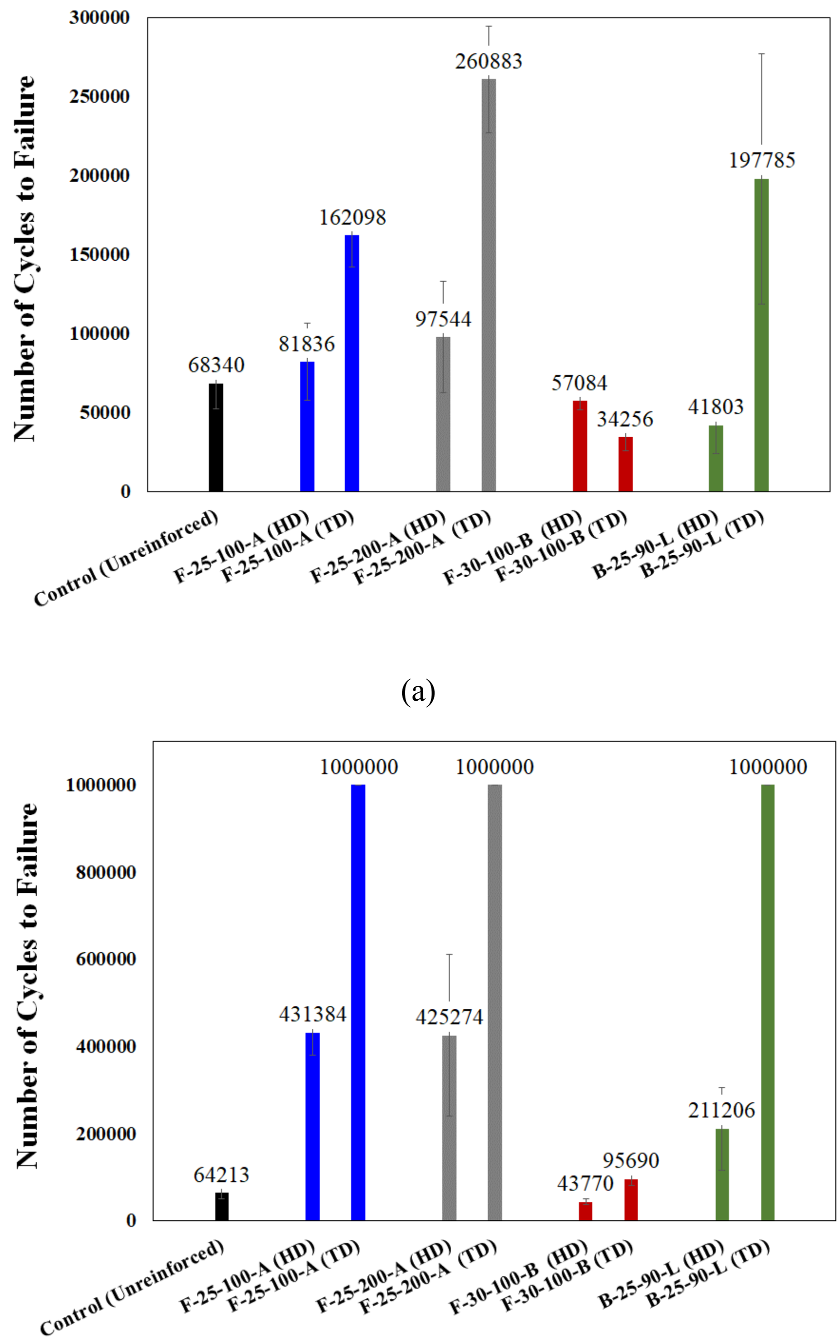

(a)

(b)

Figure 26. BBF number of cycles to failure results at (a) 20°C and (b) 4°C.

In addition, the $N_{f\text{-}BBF}$ varied based on the depth of geogrid embedment. The geogrid-reinforced HMA mixtures with geogrids embedded at one-half depth showed an improvement in $N_{f\text{-}BBF}$ of 1.01 times compared with the unreinforced HMA. The geogrid-reinforced HMA mixtures with geogrids embedded at one-third depth (measured from the bottom of the sample), however, showed an average improvement in $N_{f\text{-}BBF}$ of 2.40 times compared with the unreinforced HMA. Therefore, the embedment depth of the geogrid in HMA mixtures proved to be a critical factor in improving the fatigue performance of HMA mixtures. This agrees with the findings from literature for geogrid-reinforced HMA mixtures when tested under flexure [18], [20], [21]. Thus, placing a strengthening component at the neutral axis would provide little reinforcement to the beam sample. In contrast, a geogrid placed below the neutral axis (in the tensioned section of the beam) would provide additional reinforcement, which is evident in the findings presented in Figure 26a. This finding also agrees with similar studies conducted on geogrid-reinforced HMA [21].

The $N_{f\text{-}BBF}$ obtained from laboratory BBF testing differed for each geogrid type utilized when tested at the intermediate testing temperature. It was found that the geogrid type with the highest tensile strength (F-25-200-A) provided the greatest improvement $N_{f\text{-}BBF}$ with an average improvement of 3.82 (with geogrids embedded at one-third depth). This finding is reasonable because the high strength geogrid type is able to withstand greater loading before degradation. The modulus degradation response and change in normalized modulus is presented in Figure 27. The relationship between fatigue/cracking service life of geogrid-reinforced HMA and the tensile strength of the geogrid type agrees with the previous laboratory tests (OT and ITS) conducted in this study.

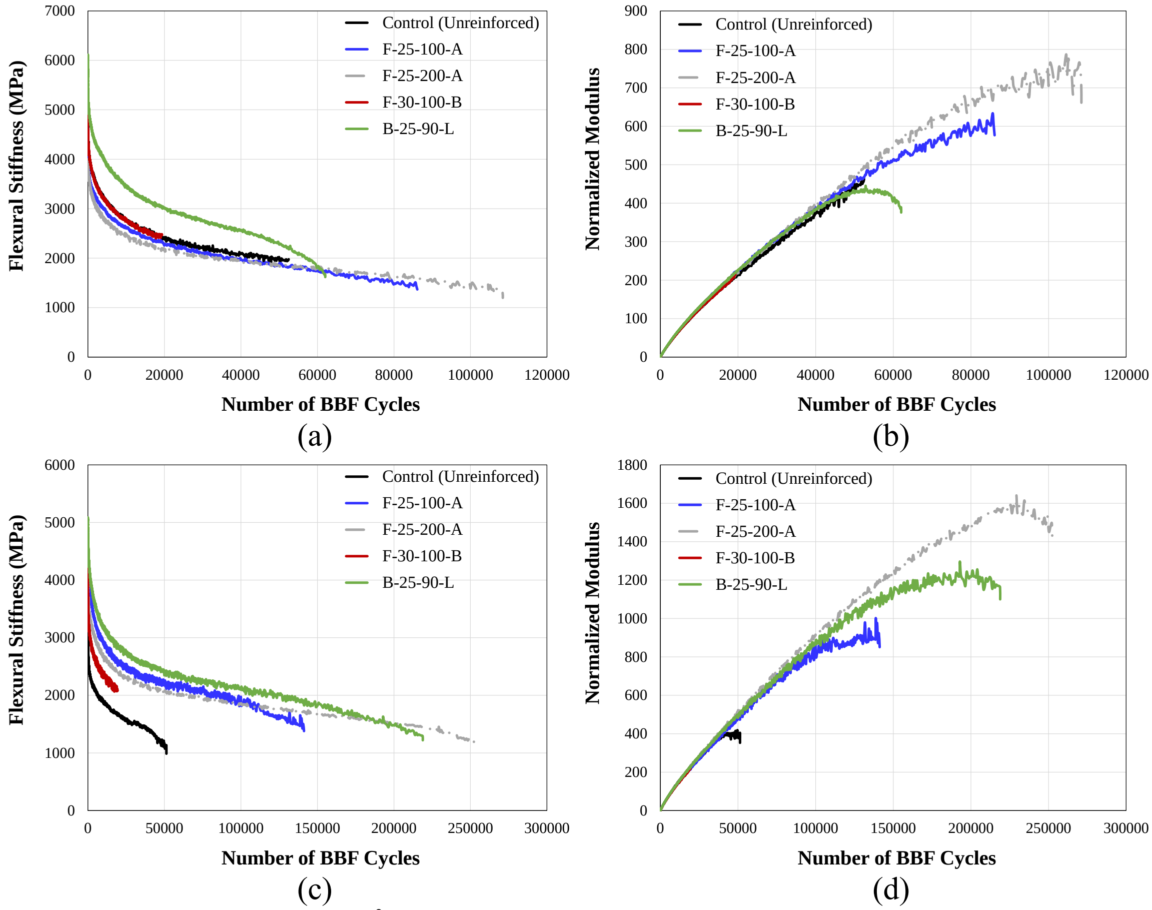

Figure 27. BBF results at 20°C for (a) flexural stiffness for one-half depth specimens, (b) normalized modulus for one-half depth specimens, (c) flexural stiffness for one-third depth specimens, and (d) normalized modulus for one-third depth specimens.

At low temperatures, the $N_{f\text{-}BBF}$ for geogrid-reinforced HMA mixtures was, on average, 13.19 times greater than that of the unreinforced HMA mixture across all geogrid types and embedment depths. As can be observed from Figure 26b, all geogrid-reinforced HMA mixtures had a greater average $N_{f\text{-}BBF}$ than the unreinforced HMA mix with the exception of one geogrid type (F-30-100-B). Furthermore, a greater improvement was observed at low temperatures (13.19 times greater) when compared to intermediate temperatures (1.71 times greater). This finding agrees with the previous laboratory testing conducted in this study under low temperature conditions (OT and ITS test results). Therefore, the fatigue resistance of geogrid-reinforced HMA was greater at cold temperatures when compared with intermediate temperatures. It is noted that the reasoning for the poor performing geogrid (F-30-100-B) may be attributed to the additional fabric placed on the bottom side of the geogrid reinforcement as can be visually observed in Figure 9c. The additional fabric may introduce a failure plane and reduce the bond between the HMA and geogrid reinforcement.

As observed with the intermediate temperatures, the $N_{f\text{-}BBF}$ varied based on the depth of geogrid embedment at low temperatures. The geogrid-reinforced HMA mixtures with geogrids embedded at one-half depth showed an average improvement in $N_{f\text{-}BBF}$ of 4.33 times compared with the unreinforced HMA. The geogrid-reinforced HMA mixtures with geogrids embedded at one-third depth (measured from the bottom of the sample), however, never reached the failure criterion and were terminated by the maximum number of BBF cycles criterion (one million cycles). Therefore, the depth of geogrid embedment is also a critical component in the fatigue performance at low temperatures (Figure 26b). The geogrid-reinforced HMA samples with geogrids embedded at one-third depth (measured from the bottom) appear to reach a state of little to no modulus degradation, thus resulting in a greater number of BBF cycles. The modulus degradation response and normalized modulus are presented in Figure 28.

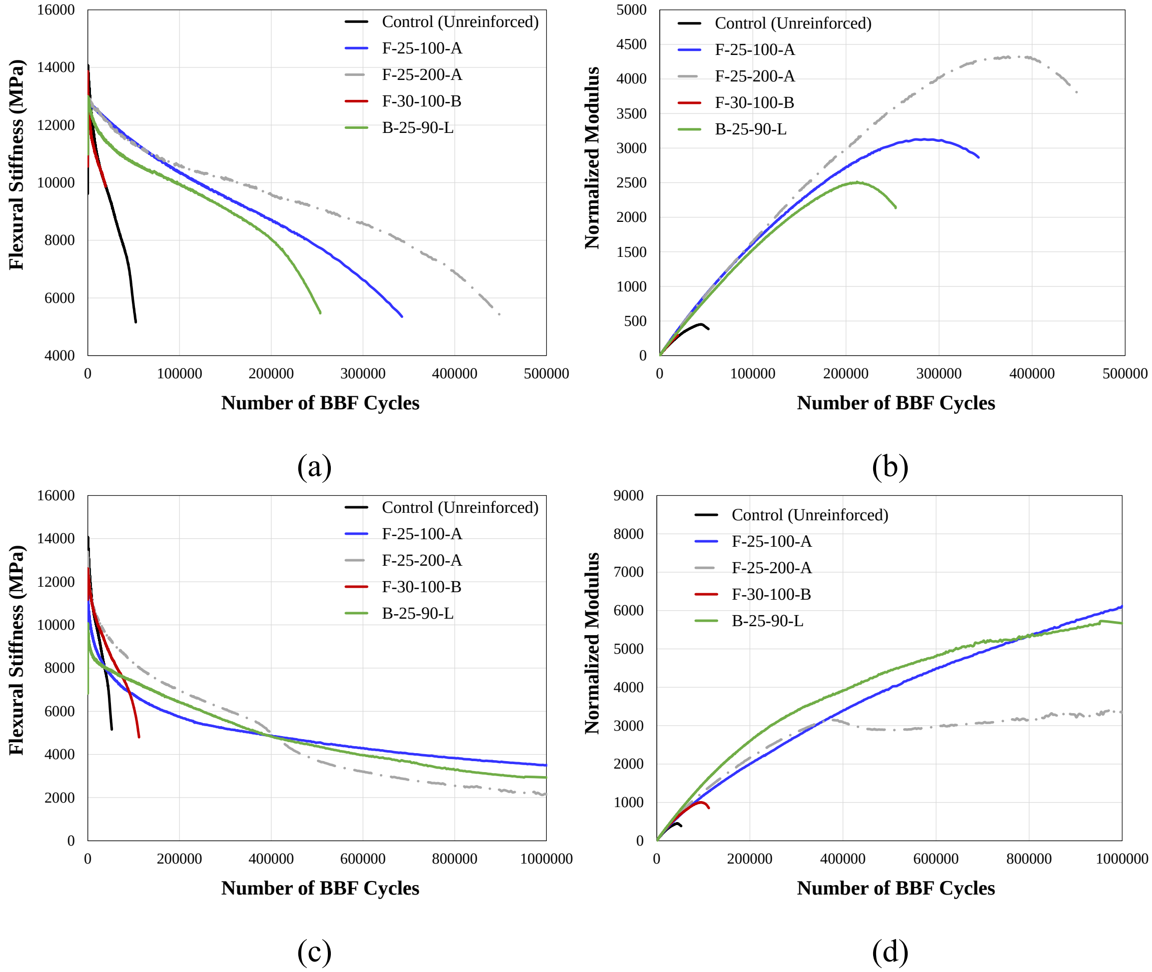

Figure 28. BBF results at 4°C for (a) flexural stiffness for one-half depth specimens, (b) normalized modulus for one-half depth specimens, (c) flexural stiffness for one-third depth specimens, and (d) normalized modulus for one-third depth specimens

It can be inferred from this finding that the tensile strain applied was less than the endurance limit of the geogrid-reinforced HMA mixtures with geogrids embedded at one-third depth (measured from the bottom). This was not the case for the unreinforced or geogrid-reinforced HMA mixtures with geogrids at half-depth, as these samples reached failure in an acceptable number of BBF cycles. Therefore, the geogrid-reinforced HMA mixtures may have greater endurance limits than unreinforced HMA mixtures under low temperature conditions. The reasoning for this behavior can be attributed to the same rationale discussed in the low temperature OT testing discussion.

A statistical analysis was conducted to evaluate the impact of geogrid depth on the cracking performance of HMA mixtures. Thus, a Student's T-test was conducted on the BBF results to determine if the geogrid depth provided a statistically significant difference in performance from the unreinforced HMA mixture. For this study, a significance level of 95% was used. Any test combination that results in a p-value less than 0.05 indicates that there is a significant difference in performance due to geogrid embedment depth. The results of the T-test analysis is presented in Table 11.

Table 13

Statistical Analysis to Evaluate the Impact of Geogrid Depth on the Performance of Geogrid-Reinforced HMA

HMA Mixture Type	**Test Temperature: 20°C**		**Test Temperature: 4°C**	
	T-Statistic	**p-value**	**T-Statistic**	**p-value**
F-25-100-A (HD)	-0.797	0.470	-12.082	0.000***
F-25-100-A (TD)	-6.248	0.003***	-119.636	0.000***
F-25-200-A (HD)	-1.302	0.284	-3.357	0.028***
F-25-200-A (TD)	-8.925	0.003***	-119.636	0.000***
F-30-100-B (HD)	1.127	0.377	2.295	0.083
F-30-100-B (TD)	3.197	0.049***	-2.655	0.057
B-25-90-L (HD)	1.895	0.131	-2.677	0.055
B-25-90-L (TD)	-0.977	0.110	-119.636	0.000***

*** Significant at confidence level of 95%

The statistical analysis at the intermediate temperature range showed that only geogrid-reinforced HMA mixtures with geogrids embedded at one-third depth (measured from the bottom) had a significant difference in performance when compared with the unreinforced HMA mixture. A similar finding was found for the cold testing temperature, in which three out of four geogrids with geogrids embedded at one-third depth showed a significant difference in performance. It is acknowledged that two geogrid types (F-25-100-A and F-25-200-A) also showed a significant improvement in performance for half-depth specimens. Overall, based Table 11, it can be observed that primarily only the geogrid-reinforced HMA mixtures with geogrids at one-third depth showed a significant difference in performance. Therefore, the depth of geogrid embedment is a critical factor that impacts the fatigue performance of geogrid-reinforced HMA.

Effects of Freeze-Thaw Cycling on Geogrid-Reinforced HMA Fatigue Cracking Performance

The freezing and thawing of pavement systems has been a readily researched issue as it creates additional voids within HMA materials [91]. This phenomenon leads to early HMA cracking and premature failure in pavement systems. Therefore, as the scope of this study is to evaluate the fatigue cracking of geogrid-reinforced HMA, it is vital to consider the effects of freeze-thaw cycling on geogrid-reinforced HMA. Methods have been developed to replicate this environmental behavior in the laboratory [91]–[94]. This has led to the development of the standard protocol (AASHTO T283) for simulating freeze-thaw cycling and evaluating the moisture sensitivity of HMA mixtures.

For this study, all samples prepared for evaluation of moisture sensitivity were conditioned according to AASHTO T283. More details regarding the conditioning process were provided previously in Chapter 3. The DCM test was also conducted on unreinforced and geogrid-reinforced HMA samples that were subjected to freeze-thaw conditioning. The freeze-thaw conditioning process was discussed in a previous subsection (Chapter 3). The results of the DCM test after freeze-thaw conditioning are presented in Figure 29.

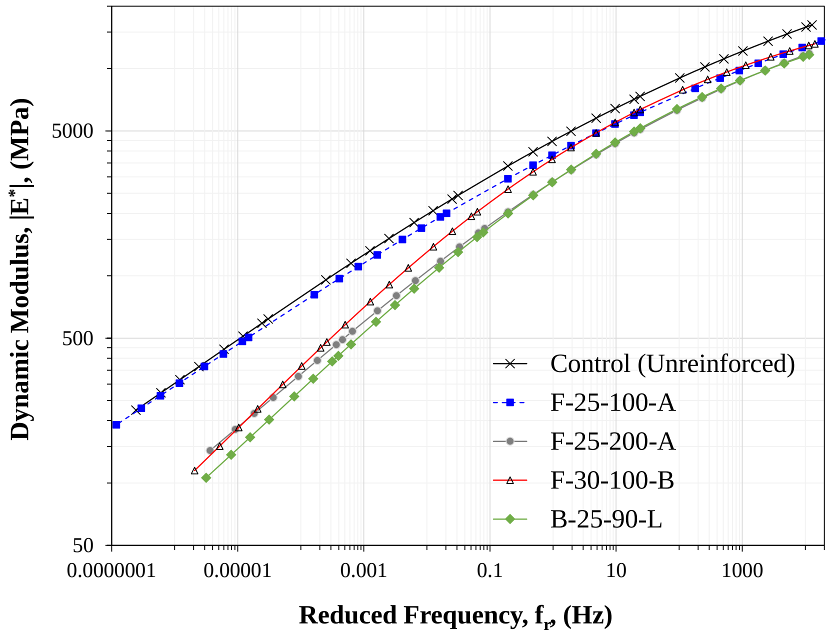

(a)

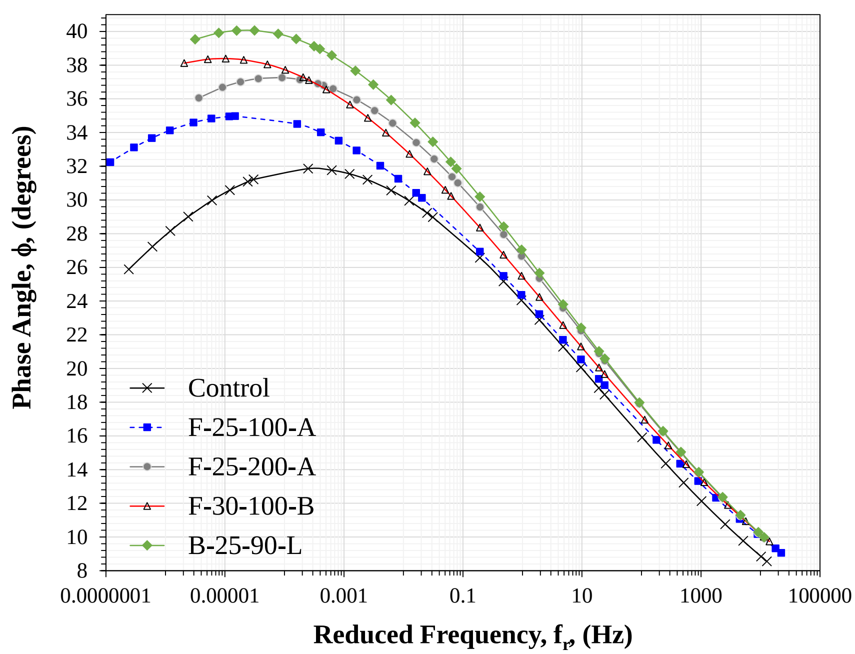

(b)

Figure 29. The (a) Dynamic modulus master curve and (b) phase angle master curve for geogrid-reinforced HMA and control HMA mixtures after freeze-thaw conditioning at 21.1˚C

From Figure 29, it was observed that the $|E^*|$ values for all geogrid-reinforced HMA mixtures are similar to or lower than that of the control (unreinforced) HMA mixture. This finding is similar to the |E*| results obtained for the samples not subjected to freeze-thaw conditioning. Additionally, Figure 29b presents an increase in phase angle due to geogrid reinforcement. As mentioned previously, the lower |E*| and increased phase angle may potentially be a result of the geogrid fiber redistribution under compressive loading. The redistribution process results in an overall compression of the geogrid material and leading to higher displacements and lower |E*| measurements. It was found that one geogrid-reinforced HMA mixture (F-25-100-A) followed more closely with the unreinforced HMA after freeze-thaw conditioning, which was not the case for the unconditioned case (Figure 18). Therefore, the effects of the geogrid (F-25-100-A) after freeze-thaw conditioning may be reduced. This leads to the assumption that the geogrid may be experiencing some level of degradation under freeze-thaw conditioning. As in the unconditioned case, the Fatigue Factor (FF) can also be determined from the |E*| results to evaluate the fatigue performance of geogrid-reinforced HMA. The FF results of the unreinforced and geogrid-reinforced HMA samples after subjected to freeze-thaw conditioning are presented in Figure 30.

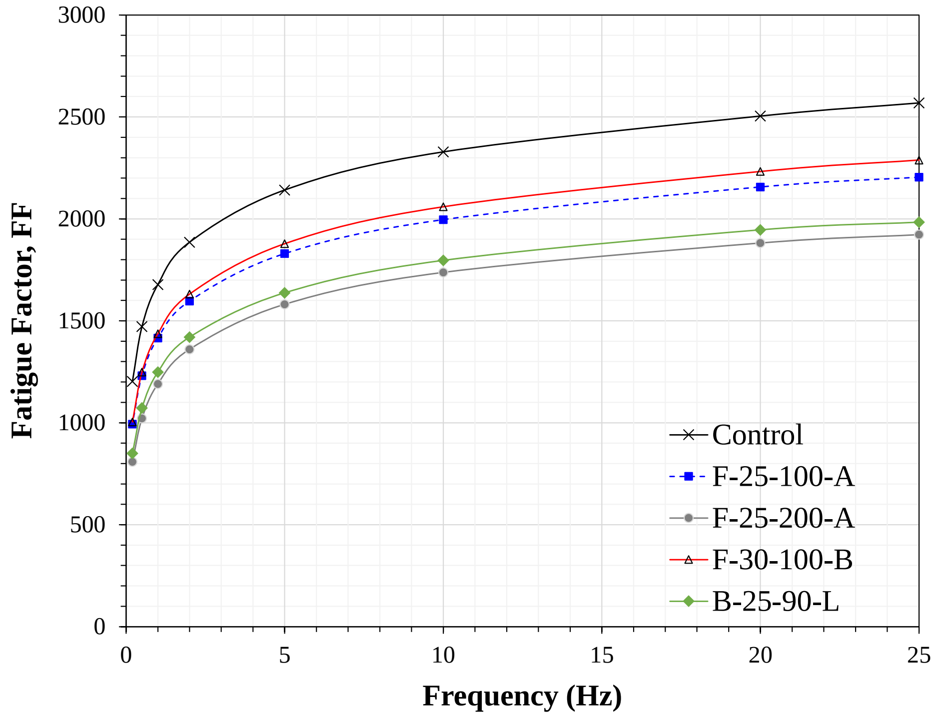

Figure 30. Results of the DCM fatigue factor analysis after freeze-thaw cycling for geogrid-reinforced HMA and control HMA mixtures at 21.1°C

As can be observed from Figure 30, the control (unreinforced) HMA mixture had the greatest FF values when compared to all other geogrid-reinforced HMA mixtures. This finding was also observed in the HMA samples that were not subjected to freeze-thaw conditioning (Figure 19). It is noted that though geogrid type F-25-100-A was similar in |E*| to the unreinforced HMA mixture, this geogrid type exhibited improved fatigue resistance when using the FF analysis. As mentioned previously, the FF findings concur with previous laboratory studies that evaluate the fatigue resistance of geogrid-reinforced HMA mixtures through flexural testing [18], [20], [21]. The type of geogrid used for reinforcing HMA mixtures also showed an impact on the FF of HMA mixtures. The FF indicated that the B-25-90-L and F-25-200-A geogrids were the best at improving the fatigue resistance of asphalt mixtures (i.e., had the lowest FF values). This was the case for both FF analyses on the unconditioned and freeze-thaw conditioned HMA specimens.

The OT on unconditioned HMA samples was replicated to investigate the effects of freeze-thaw conditioning on the cracking performance of geogrid-reinforced HMA mixtures. The OT procedure remained constant for the freeze-thaw conditioned samples (Tex-248-F) to allow for comparison between unconditioned and conditioned test samples. The freeze-thaw conditioning process followed the AASHTO T283 procedure as discussed in previous sections. The OT results at 25°C and 4°C are presented in Figure 31 for freeze-thaw conditioned samples. Additionally, the OT results for unconditioned samples are presented in Figure 31 for ease of interpretation.

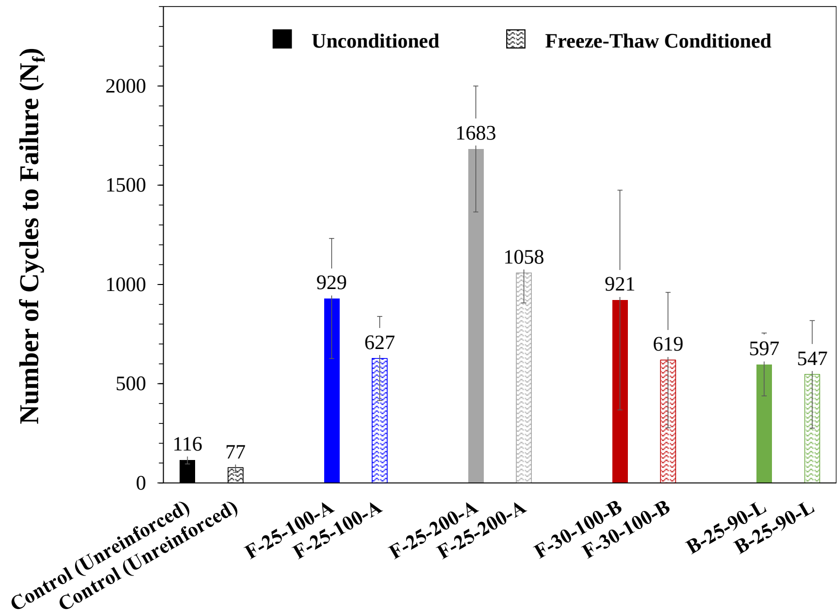

(a)

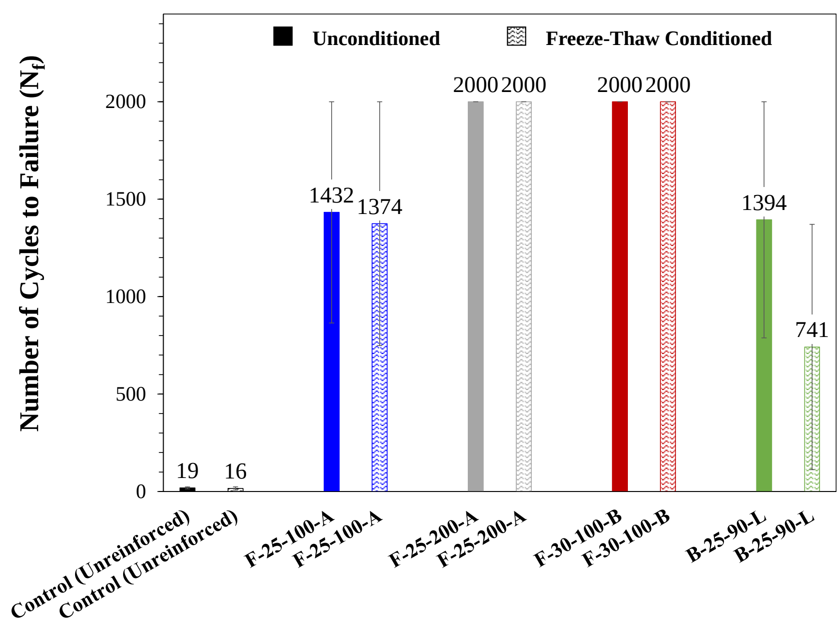

(b)

Figure 31. Results of the OT test for the control (unreinforced) and geogrid-reinforced HMA mixtures unconditioned and subjected to freeze-thaw conditioning at (a) 25°C and (b) 4°C.

As can be observed in Figure 31a, all geogrid-reinforced HMA mixtures showed an average number of OT cycles to failure ($N_{f\text{-}OT}$) greater than the unreinforced HMA mixture with an average improvement in $N_{f\text{-}OT}$ of 9.26 times across all geogrid types at intermediate temperatures. This finding is similar to the observed improvement in $N_{f\text{-}OT}$ (8.88 times greater) for unconditioned geogrid-reinforced HMA mixtures at the intermediate temperature. Therefore, the OT results indicate that geogrids are capable of improving the cracking resistance of HMA mixtures when exposed to freeze-thaw cycling. Additionally, the high tensile strength geogrid type (F-25-200-A) exhibited the greatest improvement in $N_{f\text{-}OT}$ at the intermediate testing temperature condition with an average improvement in $N_{f\text{-}OT}$ of 13.74 times. It is noted that this finding agrees with the unconditioned OT testing in which the high tensile strength geogrid type (F-25-200-A) also exhibited the greatest improvement in $N_{f\text{-}OT}$ (Figure 31a). The rationale for this trend in geogrid-reinforced HMA mixes was described previously in the unconditioned OT samples.

The low temperature OT testing also showed greater average $N_{f\text{-}OT}$ for geogrid-reinforced HMA across all geogrid types (Figure 31b). It is noted that several geogrid-reinforced HMA samples were terminated due to reaching the maximum number of OT cycles (2000 OT cycles) rather than achieving HMA failure. This also agrees with the findings found for HMA samples that were not subjected to freeze-thaw conditioning (Figure 31b). The number of OT cycles that were terminated based on reaching the maximum number of OT cycles is presented in Table 12.

Table 14

Number of Samples that Reached Maximum Number of OT Cycles at 4°C for Unconditioned and Freeze-Thaw Conditioned HMA Mixtures

4°C Unconditioned			**4°C Conditioned**		
HMA Mixture	Number of samples that reached maximum BBF cycles	Total samples tested	HMA Mixture	Number of samples that reached maximum BBF cycles	Total samples tested
Control (Unreinforced)	0	3	Control (Unreinforced)	0	3
F-25-100-A	2	3	F-25-100-A	2	3
F-25-200-A	3	3	F-25-200-A	3	3
F-30-100-B	3	3	F-30-100-B	3	3
B-25-90-L	2	3	B-25-90-L	1	3

In addition to |E*| and OT, the BBF test was also replicated on freeze-thaw conditioned samples to evaluate the effects of freeze-thaw conditioning on the fatigue performance of geogrid-reinforced HMA. It was vital to replicate the BBF testing as flexural tests are most commonly used to evaluate the fatigue performance of geogrid-reinforced HMA due to the reinforcement mechanisms of geogrids [15], [18], [20]–[23], [60], [95]. As stated previously (Chapter 3), the samples were subjected to one cycle of the freeze-thaw conditioning process as described in AASHTO T283. The samples were then conducted using the same temperatures and tensile strain rates as the unconditioned HMA samples in order to facilitate comparisons between the two data sets. The results of the BBF test at 20°C and 4°C on freeze-thaw conditioning HMA samples are presented in Figure 32 and Figure 33, respectively.

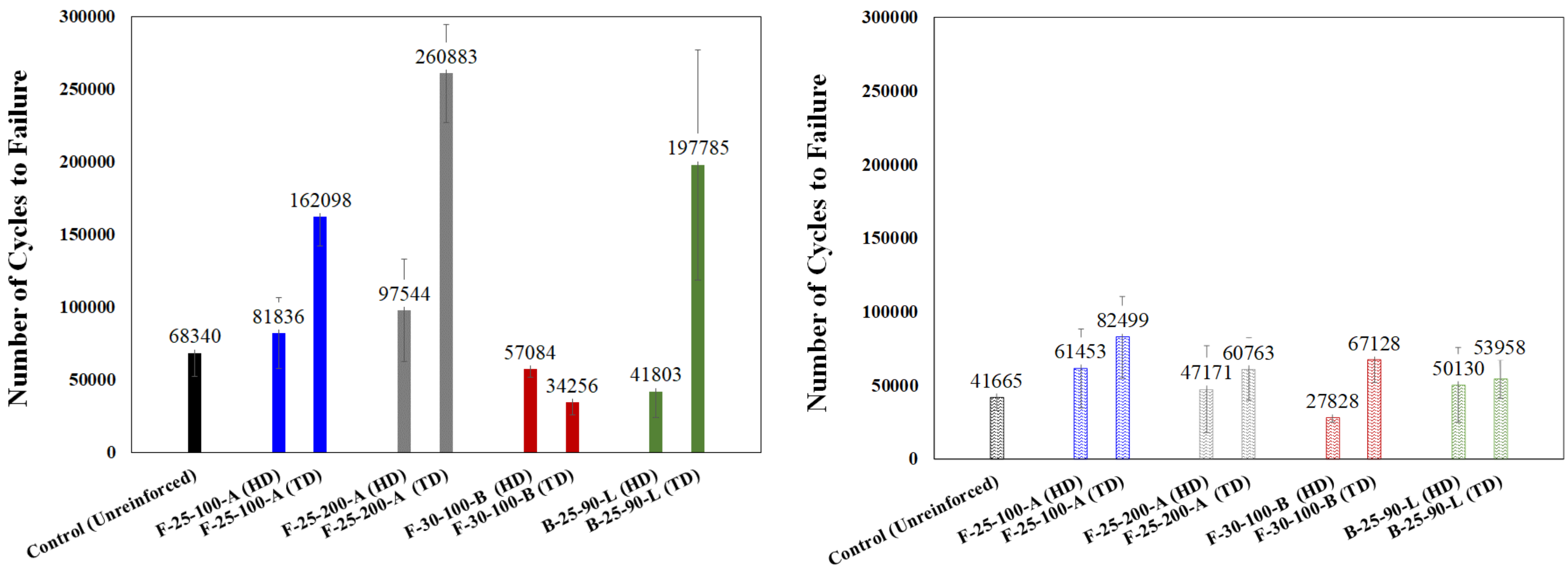

(a) (b)

Figure 32. BBF number of cycles to failure results for (a) unconditioned and (b) freeze-thaw conditioned samples at 20˚C.

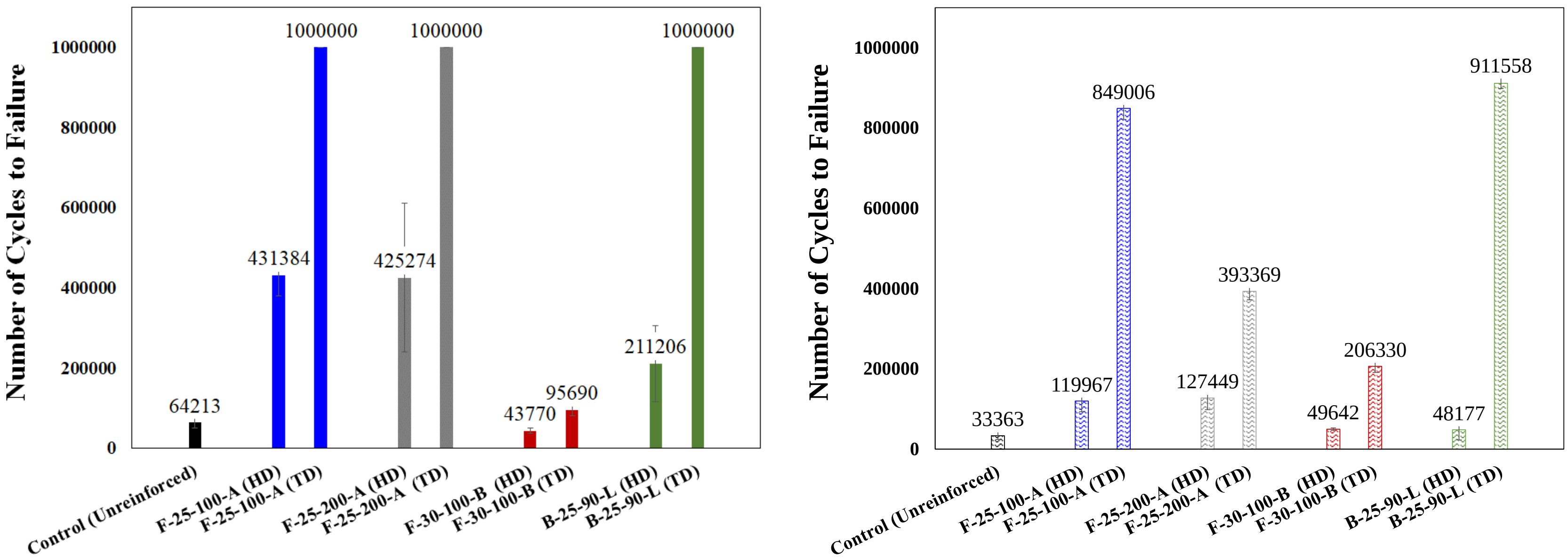

(a) (b)

Figure 33. BBF number of cycles to failure results for (a) unconditioned and (b) freeze-thaw conditioned samples at 4°C.

When exposed to freeze-thaw conditioning, the number of BBF number to failure ($N_{f\text{-}BBF}$) for geogrid-reinforced HMA mixtures was on average 1.35 times greater than that of the unreinforced HMA mixture across all geogrid types and embedment depths at the intermediate temperature. This is evident from Figure 32a in which seven out of the eight geogrid-reinforced HMA mixtures had a greater average $N_{f\text{-}BBF}$ than the unreinforced HMA mixture. It is noted that the average improvement in $N_{f\text{-}BBF}$ was lower for the BBF samples that were exposed to freeze-thaw conditioning (1.35 times greater) compared with the BBF samples that were unconditioned (1.71 times greater). Therefore, it is evident that the freeze-thaw conditioning reduced the effectiveness of using geogrids in HMA mixtures. It is noted that the geogrid-reinforced HMA mixtures with geogrids embedded at one-third depth (measured from the bottom) outperformed the half-depth mixtures, which was similar to the trend observed in the unconditioned state.

Further, the freeze-thaw cycling removed the benefits of embedding geogrids at one-third depth that was evident in the unconditioned geogrid-reinforced HMA mixtures (Figure 32). In fact, at intermediate temperatures, the HMA mixtures with geogrids embedded at half-depth experienced an improvement in $N_{f\text{-}BBF}$ of 1.12. The HMA mixtures with geogrids embedded at one-third depth (measured from the bottom) illustrated an improvement in $N_{f\text{-}BBF}$ of 1.59, which is a difference of 0.47. The difference for freeze-thaw conditioned samples is lower than the difference exhibited at intermediate temperatures for unconditioned BBF samples (1.39). Therefore, it can be concluded that the freeze-thaw conditioning reduces the effectiveness of geogrid embedment depth in the overall laboratory BBF performance.

With respect to low temperature testing, the geogrid-reinforced HMA mixtures showed $N_{f\text{-}BBF}$ values that were on average 10.13 times greater than those of the unreinforced HMA mixture across all geogrid types and embedment depths at the intermediate temperature he geogrid-reinforced HMA mixtures exhibited. As can be observed from Figure 33*Figure 33*, all geogrid-reinforced HMA mixtures outperformed the unreinforced HMA mixtures. It is noted that at low temperatures, there existed unconditioned BBF samples with geogrids embedded at one-third depth (measured from the bottom) that did not reach failure and were terminated based on the maximum allowable number of BBF cycles. This was also observed for the freeze-thaw conditioned geogrid-reinforced HMA samples. A comparison between the number of samples that did not reach failure for the unconditioned BBF samples and freeze-thaw conditioned BBF samples is presented in Table 13. From Table 13, it can be observed that a lower number of HMA BBF samples did not reach failure when subjected to freeze-thaw conditioning.

Table 15

Number of Samples that Reached Maximum Number of BBF Cycles at 4°C for Unconditioned and Freeze-Thaw Conditioned HMA

4°C Unconditioned			**4°C Conditioned**		
HMA Mixture	Number of samples that reached maximum BBF cycles	Total samples tested	HMA Mixture	Number of samples that reached maximum BBF cycles	Total samples tested
Control (Unreinforced)	0	3	Control (Unreinforced)	0	3
F-25-100-A	3	6	F-25-100-A	1	6
F-25-200-A	3	6	F-25-200-A	0	6
F-30-100-B	0	6	F-30-100-B	0	6
B-25-90-L	3	6	B-25-90-L	2	6

A statistical analysis was also used to evaluate the impact of freeze-thaw on the cracking performance of HMA mixtures. As conducted previously for evaluation of geogrid depth, a Student's T-test was conducted on the freeze-thaw BBF results between the geogrid-reinforced HMA mixtures and the unreinforced HMA mixtures. For this study, a significance level of 95% was used. Any test combination that results in a p-value less than 0.05 indicates that there is a significant difference in performance due to freeze-thaw. The results of the T-test analysis is presented in Table 14.

Table 16

Statistical Analysis to Evaluate the Impact of Freeze-Thaw Conditioning on the Performance of Geogrid-Reinforced HMA

HMA Mixture Type	Test Temperature: 20°C		Test Temperature: 4°C	
	T-Statistic	p-value	T-Statistic	p-value
F-25-100-A (HD)	-1.204	0.295	-2.931	0.043***
F-25-100-A (TD)	-2.434	0.072	-10.315	0.001***
F-25-200-A (HD)	-0.310	0.772	-9.580	0.001***
F-25-200-A (TD)	-1.426	0.227	-7.414	0.002***
F-30-100-B (HD)	2.439	0.071	-1.364	0.244
F-30-100-B (TD)	-2.474	0.069	-26.000	0.000***
B-25-90-L (HD)	-0.545	0.615	-1.076	0.343
B-25-90-L (TD)	-0.977	0.384	-9.924	0.001***

*** Significant at confidence level of 95%

The statistical analysis at the intermediate temperature range showed that the geogrid-reinforced HMA mixtures showed no significant difference in fatigue performance compared with the unreinforced HMA mixture. This finding varies from the findings in the unconditioned state where the geogrid-reinforced HMA mixtures with geogrids embedded at one-third depth showed a statistically significant change in fatigue performance from the unreinforced HMA mixture.

In contrast to the intermediate temperature, the statistical analysis showed similar findings for the unconditioned and conditioned HMA mixtures at the cold testing temperature. This is primarily due to the fact that the cold temperature testing showed such improvement in $N_{f\text{-}BBF}$ so any decrease in $N_{f\text{-}BBF}$ due to conditioning was not significant. Overall, based on Table 14, it can be observed that freeze-thaw conditioning reduces the effectiveness of geogrids in HMA mixtures.

Based on the findings of the effects of freeze-thaw conditioning on fatigue performance, it is evident that the freeze-thaw conditioning deters the effectiveness of using geogrid reinforcements to deter HMA cracking. A potential reason for this finding may be the result of water absorption and expansion in the geogrid reinforcement during the freeze-thaw process. At the microstructure level, the geogrid can potentially be absorbing moisture. Thus, the freeze-thaw process may create additional air voids along the geogrid plane. The effects of freezing and thawing geogrids that have absorbed moisture can be visually represented in Figure 34. This could potentially lead to a reduction in the geogrid to HMA bond and the overall fatigue cracking performance of geogrid-reinforced HMA.

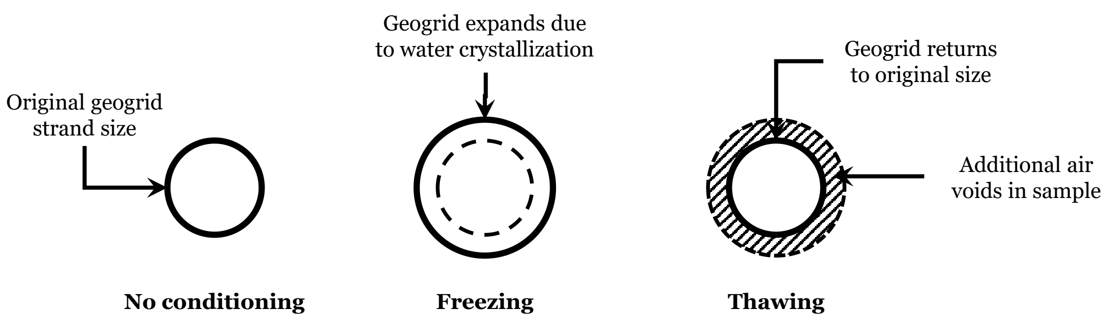

Figure 34. Representation of potential geogrid behavior when exposed to freeze-thaw conditioning

Therefore, in an effort to determine the accuracy of the freeze-thaw geogrid behavior, the geogrid reinforcement must exhibit signs of absorption when exposed to moisture. Absorption testing has been readily conducted on coarse and fine aggregates to assist in the mix design of HMA mixtures [82], [96]. Standards (AASHTO T85 and AASHTO T84) were then developed to determine the absorption of aggregates in HMA mixtures. The standard for coarse aggregate absorption (AASHTO T85) was considered in this study to evaluate the absorptive properties of geogrid materials. However, the standard could not be followed directly due to the fact that aggregates were not being tested. Therefore, in effort to best replicate the test procedure on aggregates, the geogrids were cut into 3 inch by 3 inch squares with no restriction on the number of geogrid strands in either direction. The geogrid samples were then submerged in water and saturated for 16 hours. Images of the saturated geogrid reinforcements are provided in Figure 35.

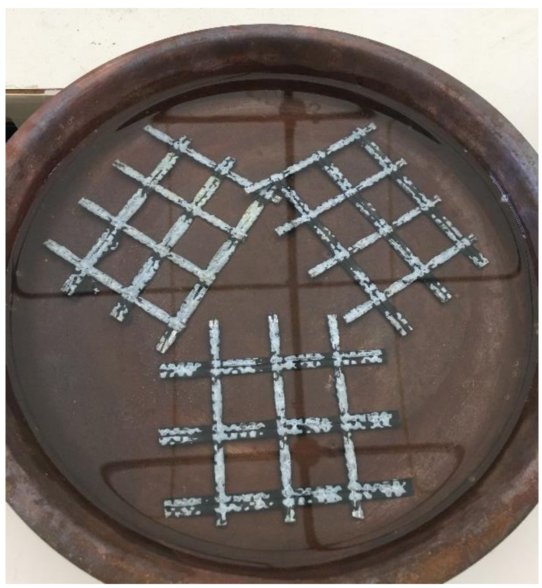

Figure 35. Representation of potential geogrid behavior when exposed to freeze-thaw conditioning

The saturated geogrids were then patted dry using a damp tower to achieve the saturated surface dry (SSD) state and weight measurements were taken. It is noted that the weight measurements were taken with a precision of 0.001 grams due to the lightweight nature of the geogrid reinforcement. The absorption of each geogrid sample was then determined using the formula in AASHTO T85. The results of the absorption testing are presented in Figure 36.

$$Absorption\ (\%) = \frac{B-A}{A} \times 100 \tag{15}$$

Where,

A = Mass of dry geogrid sample, g

B = Mass of SSD geogrid sample, g

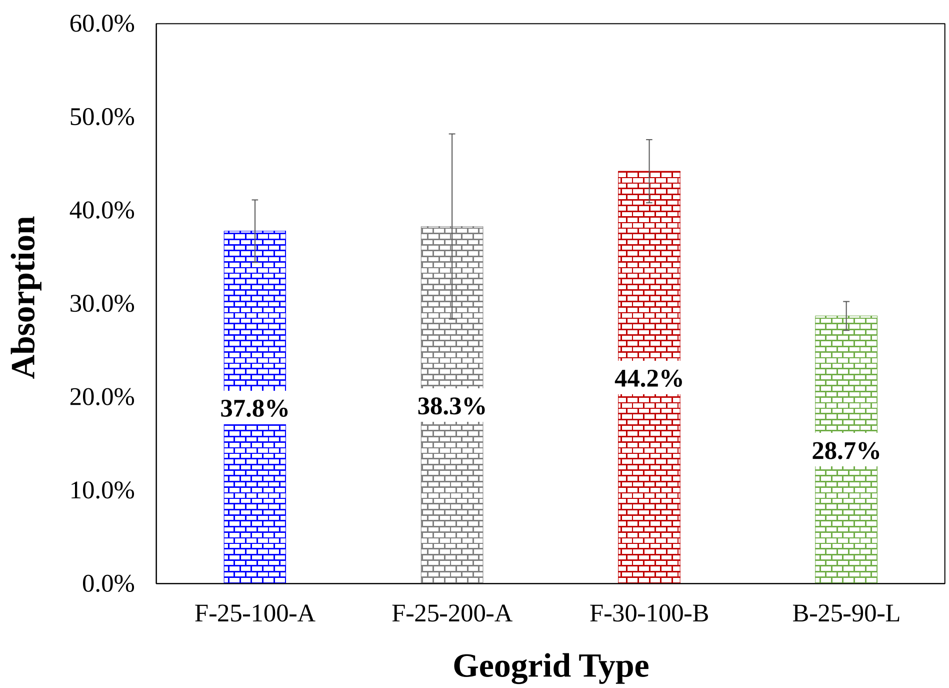

Figure 36. Results from the absorption measurements for each geogrid type according to AASHTO T85.

As can be seen from Figure 36, all geogrid types showed absorptive characteristics when exposed to water. The three fiberglass type geogrids (F-25-100-A, F-25-200-A, and F-30-100-B) had greater absorption levels than the basalt geogrid (B-25-90-L), which may be a result of the material used to manufacture the geogrid reinforcement. This finding also correlates with the findings from the BBF testing at low temperature (Table 13). As presented previously, Table 13 showed that the number of samples that did not reach failure at low temperature testing reduced by one for the basalt geogrid type (B-25-90-L), whereas the other geogrid-reinforced mixes reduced by two or more samples. It is also worth noting that the geogrid type with the highest absorption (F-30-100-B) exhibited poor performance in the BBF testing. The high absorption levels in this geogrid type may be a result of the additional fabric located on the bottom of the geogrid, which was presented previously in Figure 9c.

Effects of Compaction Procedures on the Fatigue Cracking Performance of Geogrid-Reinforced HMA

It is vital to simulate similar field HMA compaction conditions during laboratory testing. The main concern for this study is that there is uncertainty in the field compaction conditions of geogrid-reinforced HMA. The method and conditions of geogrid-reinforced HMA construction and compaction have the potential to impact the overall performance of the material. In fact, laboratory studies have been conducted on construction and compaction methods of geogrid-reinforced HMA investigating the depth of embedment and the use of tack coat [13], [18], [20], [21]. Therefore, an additional testing factor was included in this study to investigate the effects of laboratory compaction procedures on the fatigue cracking performance of geogrid-reinforced HMA. Two compaction procedures (hot and cold compactions) were developed to investigate the most extreme potential field conditions for constructing geogrid-reinforced HMA. Each field condition would be dependent on the environmental conditions, the rate of geogrid and HMA placement, and the temperature of the HMA layers. Thus, it is beneficial to evaluate extreme compaction conditions for a better understanding of the fatigue cracking performance of geogrid-reinforced HMA. A greater description was provided previously of each compaction procedure (Chapter 3).

For this study, two geogrid types were evaluated under the varying construction conditions. It is noted that the testing matrix was reduced for this part of the study due to the added time and complexity of compacting the geogrid-reinforced HMA mixtures using the cold compaction procedure. The first geogrid type (F-25-200-A) was selected because it showed the greatest performance using the hot compaction procedure. The second geogrid type (B-25-90-L) was selected because it had no additive coating to aide in geogrid-HMA bonding. The lack of additive coating may result in significantly different performance evaluations between the hot and cold HMA compaction procedures.

The BBF test was selected as the method to evaluate the effect of different compaction procedures. This test was selected based on the test method most commonly utilized in literature for geogrid-reinforced HMA. To facilitate comparisons between the hot and cold compaction procedures, all BBF testing parameters remained constant to the hot compaction procedures that were discussed previously. The BBF results using the cold compaction (CC) procedure at 20°C and 4°C are presented in Figure 37. It is also noted that the BBF results using the hot compaction (HC) procedure are presented again in Figure 37 for comparison between compaction procedures.

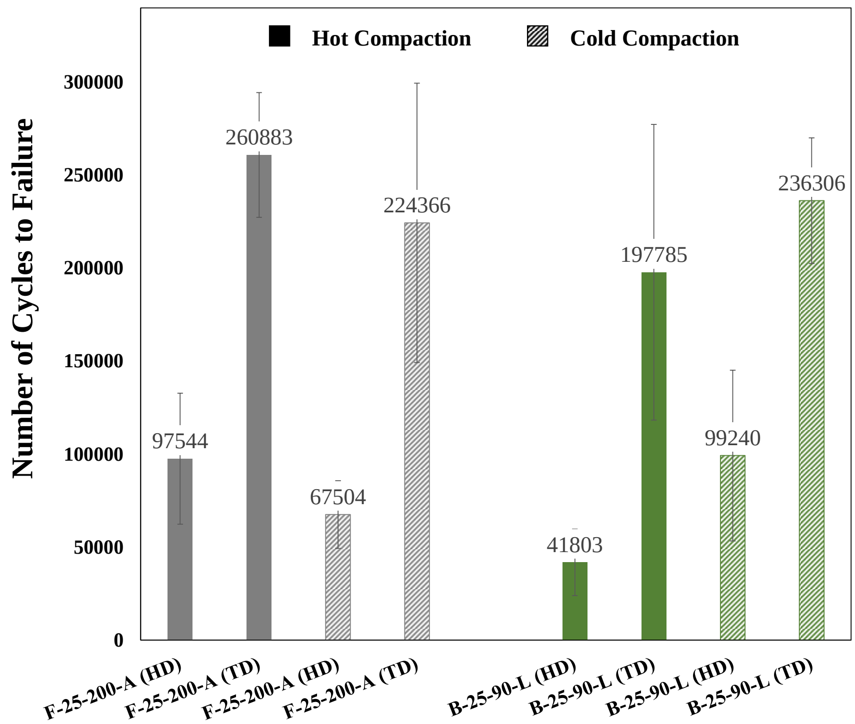

(a)

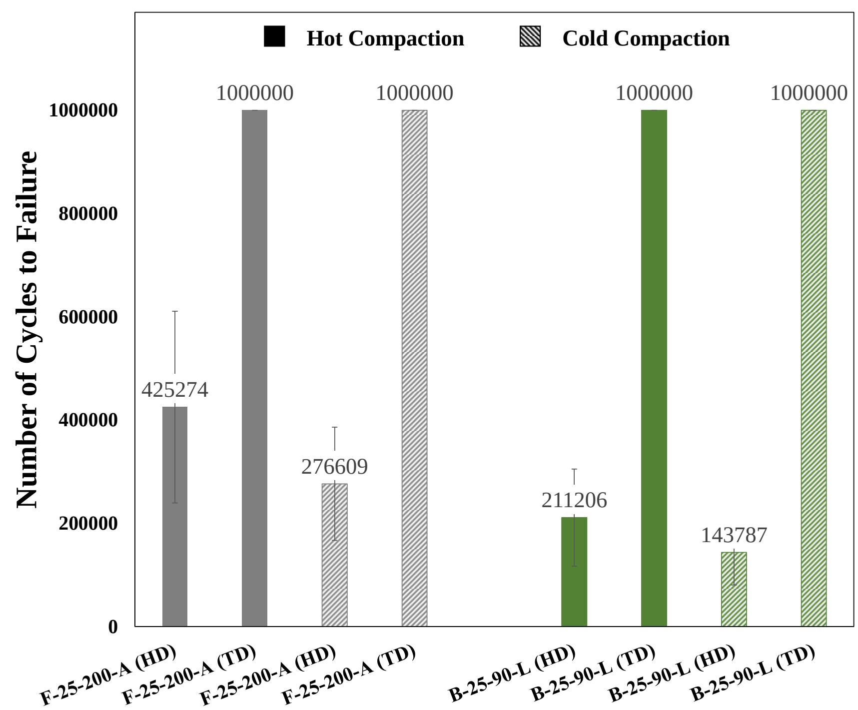

(b)

Figure 37. Summary of BBF test on geogrid and unreinforced HMA mixtures at (a) 20°C and (b) 4°C using the hot and cold compaction procedures

Further, a statistical analysis was conducted using a Student's T-test to determine if the compaction procedures provided a statistically significant difference in performance. For this study, a significance level of 95% was used. Any test combination that results in a p-value less than 0.05 indicates that there is a significant difference in performance between the hot and cold compaction procedures. The results of the T-test analysis is presented in Table 15. As can be seen from Table 15, there was no condition in which the compaction procedure significantly impacted the performance.

As can be seen from Figure 37, the number of BBF cycles to failure ($N_{f\text{-}BBF}$) was statistically similar for the hot and cold compaction procedures. This finding appeared to indicate that the method of laboratory fabrication does not significantly impact the fatigue performance of geogrid-reinforced HMA. The reason for this trend in $N_{f\text{-}BBF}$ between the cold and hot compaction procedures may be attributed to the micromechanical bonding occurring between the HMA layers and the geogrid reinforcement. In the case of the cold compaction procedure, an asphalt emulsion (in this study CSS-1h emulsion) was applied according to the manufacturer specifications in order to aide in the bonding process. This application of asphalt emulsion would be common in the use of geogrid reinforcements in HMA layers. On the other hand, the HMA is placed while the mixture is still at compaction temperature. In this state, the asphalt binder has low viscosity during compaction and can also aide in the bonding process. Thus, as a result, the added emulsion and hot asphalt binder from each compaction procedure may be acting as a similar overall bonding agent between the geogrid reinforcement and HMA.

Table 17

Statistical Analysis to Evaluate the Impact of Compaction Procedure on the Performance of Geogrid-Reinforced HMA

HMA Mixture	Test Temperature: 20°C		Test Temperature: 4°C	
	T-Stat	P-value	T-Stat	P-value
F-25-200-A-HD	1.313	0.281	-1.194	0.318
F-25-200-A-TD	0.769	0.498	Note 1	Note 1
B-25-90-L-HD	-2.02	0.137	1.030	0.379
B-25-90-L-TD	-0.772	0.496	Note 1	Note 1

Note 1: The samples were all terminated at 1 million BBF cycles and did not achieve failure

Furthermore, a compaction analysis was conducted on geogrid reinforcement to quantify the constructability, or workability, of geogrid-reinforced HMA materials. When introducing an HMA modifier during the construction process, such as geogrid reinforcement, it is important to investigate if there is an impact on the workability of HMA mixtures. Thus, a lower workability (or higher CDI value) can be interpreted as additional compaction energy required to reach a desired density level. Two methods have been used to investigate the workability: (i) number of gyrations to reach a desired compaction level and (ii) the Construction Densification Index (CDI). Figure 38 presents results of the compactability analysis conducted as part of this study.

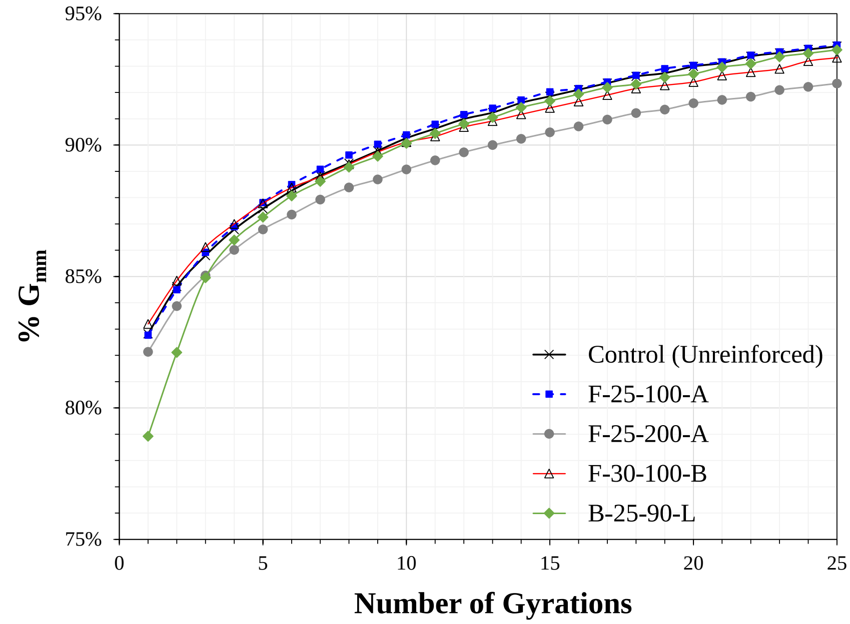

(a)

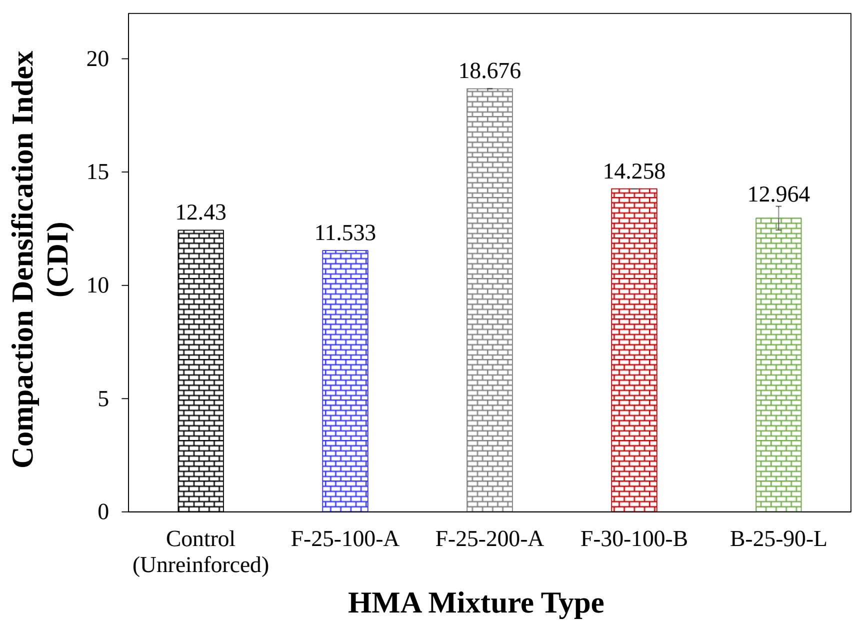

(b)

Figure 38. Compactability analysis results for (a) construction portion of compaction curves for control (unreinforced) and geogrid-reinforced HMA mixtures and (b) compaction densification index.

As can be seen from Figure 38a, all HMA mixtures reached a %G_{mm} level of 92% at a similar rate (around 17 gyrations) except for geogrid-reinforced HMA samples prepared using F-25-200-A geogrids which had a 92% densification level after applying 23 gyrations. Both evaluation methods (Figure 38a and Figure 38b) indicated that no additional compaction energy is necessary for three geogrid types (F-25-100-A, F-30-100-B, B-25-90-L). As can be seen from Figure 38b, one geogrid type (F-25-200-A) resulted in higher CDI values and a reduction in the workability of the HMA mixture. This reduction in workability may be a result of the higher tensile strength of the geogrid. The increased tensile strength may inhibit and reduce aggregate movement during compaction, thus resulting in a decrease in the workability of the HMA mixture.

Chapter 5

Finite Element Model of Geogrid-Reinforced HMA

The goal of this chapter is to identify, develop, and/or modify different approaches to model geogrid reinforcements in HMA. The topics include a brief review of FEM and the critical evaluation points for evaluation in pavement systems, relevant material constitutive behavior models for flexible pavement systems, and the different FEM approaches used to model geogrid reinforcements. Finally, the developed FEM approaches were then implemented into a full-scale pavement system simulation to predict the change in mechanistic responses due to the use of geogrids in HMA.

Background

FEM allows for the simulation of different loading conditions on any system. In the field of pavement engineering, FEM has been used to evaluate pavement systems with modified HMA material parameters, different pavement structural conditions, varying traffic loading patterns, etc. The simulated pavement systems are commonly modeled using a typical pavement system structure and the mechanistic responses are evaluated at the critical points of the flexible pavement system [80], [97].

A typical flexible pavement system consists of three different layers—subgrade, base, and HMA—as shown in Figure 39. This general flexible pavement design is used to achieve the most economical design for base and HMA layers, taking into account the expected traffic loading and the natural soil strength. The thickness of each flexible pavement layer is dependent on the traffic loading and the distribution of the load from the asphalt surface course to the lower aggregate layers. In flexible pavement systems, traffic loading on the surface results in localized flexural and compressive strains below the wheel load. The two critical strains of a flexible pavement system are (i) tensile strain at the bottom of the HMA layer and (ii) compressive strain at the top of the subgrade layer. These critical strains are illustrated in Figure 39. A failure at these critical points can lead to pavement distresses and/or pavement failure.

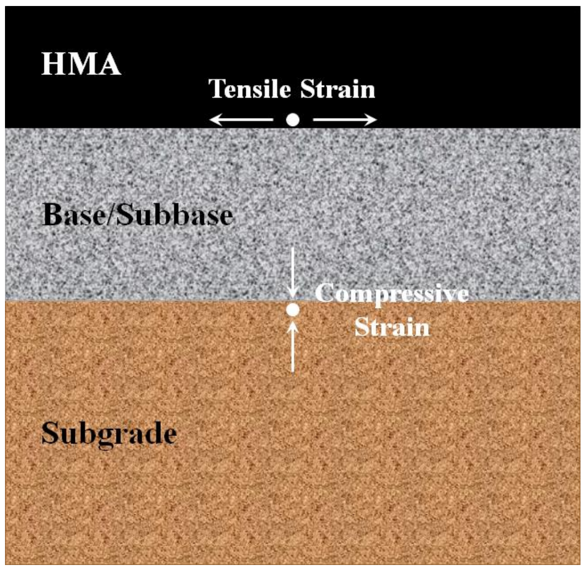

Figure 39. General flexible pavement design with associated critical points.

General Theory of Finite Element Analysis

FEM approximates a finite solution for a specified state variable (i.e. stress, strain, displacements, etc.). During simulation, an exact solution can be reached only through the equilibration of force and moment at any arbitrary volume within the model. This requirement is difficult to maintain in complex systems; thus, a weaker assumption is made and an approximated solution is obtained. The weaker requirement to be maintained is an equilibrium of force and moment over a finite number of divisions of the volume of the body. The entire system equilibration can be expressed in Equation 16.

$$\int_S \boldsymbol{t}\, dS + \int_V \boldsymbol{f}\, dV = 0 \tag{16}$$

Where,

t = surface traction force per unit of current area

f = body force per unit of current volume

Through the application of the Gaussian theorem and matrix functions, the equilibration statement applied to the elements is a combination of the force and moment equilibration equations, called the virtual work statement. The principle of virtual work states that the work done by external forces must equal the work done by internal forces [98]. The equilibrium equation must be numerically solved to determine the internal forces on the system. The numerical solution technique used for solving the nonlinear equilibrium equations is commonly the Newtonian method [98]. The Newton method utilizes Taylor Series and an iterative process to minimize the difference between the approximated solution and the exact solution. This method is the default method used by FEM software packages because the convergence rate is greater for this method; however, alternative numerical techniques can be utilized in to solve the nonlinear equilibrium equations [98].

Material Constitutive Behaviors

Elasticity. Pavement layers can be modeled by assuming an isotropic elastic behavior model. This material constitutive model has been readily implemented in the FEM of full-scale pavement systems [80], [97]. Therefore, an isotropic elastic material behavior model was adopted for the base and subgrade layers of the pavement system.

This was assumed to be acceptable because pavement distresses due to failure in the unbound pavement layers (i.e. rutting) was not considered in this study.

Viscoelasticity. Typically, asphalt concrete has been modeled under the assumption of an elastic material [2], [63], [65], [66], [68], [69]; however, hot-mix asphalt concrete exhibits a viscoelastic behavior [99]. Viscoelasticity is a material property that exhibits both elastic and viscous characteristics when undergoing deformation. Therefore, the total strain experienced in these materials becomes dependent on the time the loading is applied. This differentiation from classic elastic theory provides a more accurate representation of the mechanical responses the specific material is experiencing.

In the context of pavement system, during the application of vehicular traffic, the pavement system will experience the peak stress at contact, but will exhibit peak strain values at a delayed response due to the viscous component of its behavior. The quantification of this delay has been attempted through several rheological models. These models consist of two primary elements—Hookean and Newtonian—that describe the elastic and viscous damping components of viscoelastic materials, respectively. Rheological models exist to quantify the viscoelastic relationships utilizing the Hookean and Newtonian elements. The generalized Maxwell model is a common rheological model used to define HMA viscoelastic material behavior with a Hookean and Newtonian element connected in series [99]. The generalized Maxwell model is represented in Figure 40.

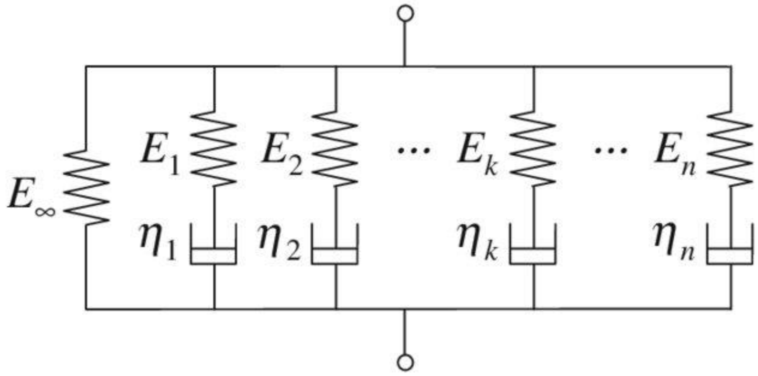

Figure 40. Representation of the Generalized Maxwell model using spring (Hookean) and dashpot (Newtonian) elements connected in parallel [100].

The model is widely implemented because it is able to quantify both strain accumulation and stress relaxation in HMA materials. The generalized Maxwell model is defined through the use of a Prony Series in which each series parameter defines a new set of Hookean and Newtonian elements in the complex series. The application of this analysis to HMA materials has been widely researched [101]–[108]. Equation 17 and Equation 18 represent the general Prony series equations in the time and frequency domain used to determine the viscoelastic properties of HMA.

$$E(t) = E_e + \sum_{i=1}^{m} E_i e^{\frac{-t}{\tau_i}} \tag{17}$$

$$E(\omega) = E_\infty + \sum_{i=1}^{m} \frac{i \times \omega \times \tau_i \times E_i}{i \times \omega \times \tau_i + 1} \tag{18}$$

Where,

E(t), E(ω) = Relaxation modulus in the time (t) and frequency (ω) domain

t = time

ω = angular frequency

$E_{e,}$ = Instantaneous elastic modulus

E_∞ = Long-term elastic modulus

E_i, τ_i = Model fitting parameters

Commonly, FEM software packages utilize shear and bulk modulus values to define the viscoelastic behavior [98]. The Prony-series models for the shear modulus, G(t), and bulk modulus, K(t), are shown in Equations 19 and 20.

$$G(t) = G_0(1 - \sum_{i=1}^{n} G_i\left(1 - e^{\frac{-t}{\tau}}\right)) \qquad (19)$$

$$K(t) = K_0(1 - \sum_{i=1}^{n} K_i\left(1 - e^{\frac{-t}{\tau}}\right)) \qquad (20)$$

Where,

G(t), K(t) = Shear and Bulk Modulus

G_0 and K_0 = Instantaneous Shear and Bulk modulus

G_i, K_i, and τ_i = Model fitting parameters

The method used to determine appropriate Prony series parameters is an iterative process that minimizes the error between predicted modulus values using Prony series and known modulus values. An error function (χ^2) is introduced as function to be minimized and includes two terms due to both the real and imaginary parts of the complex modulus. The accuracy of the Prony series is dependent on the study. Some researchers have established a tolerance level to determine if an appropriate number of parameters have been implemented [109]. Other researchers, however, have visually inspected the curve fitting process and compared with known |E*| values [110]. The number of Prony series parameters needed in the prony model is determined by incrementally increasing the number of parameters until the tolerance level is reached [111].

Geogrid Modeling Approaches

For this study, two separate approaches were considered for the modeling of geogrid reinforcements in HMA layers: (i) elastic geogrid reinforcement and (ii) modified HMA material behavior. The first procedure has been thoroughly utilized in literature for the FEM of geogrids [72], [78]–[80]. The second procedure is a novel approach that modifies the viscoelastic properties of the HMA layer for geogrid reinforcements. The framework of each procedure is presented in Figure 41.

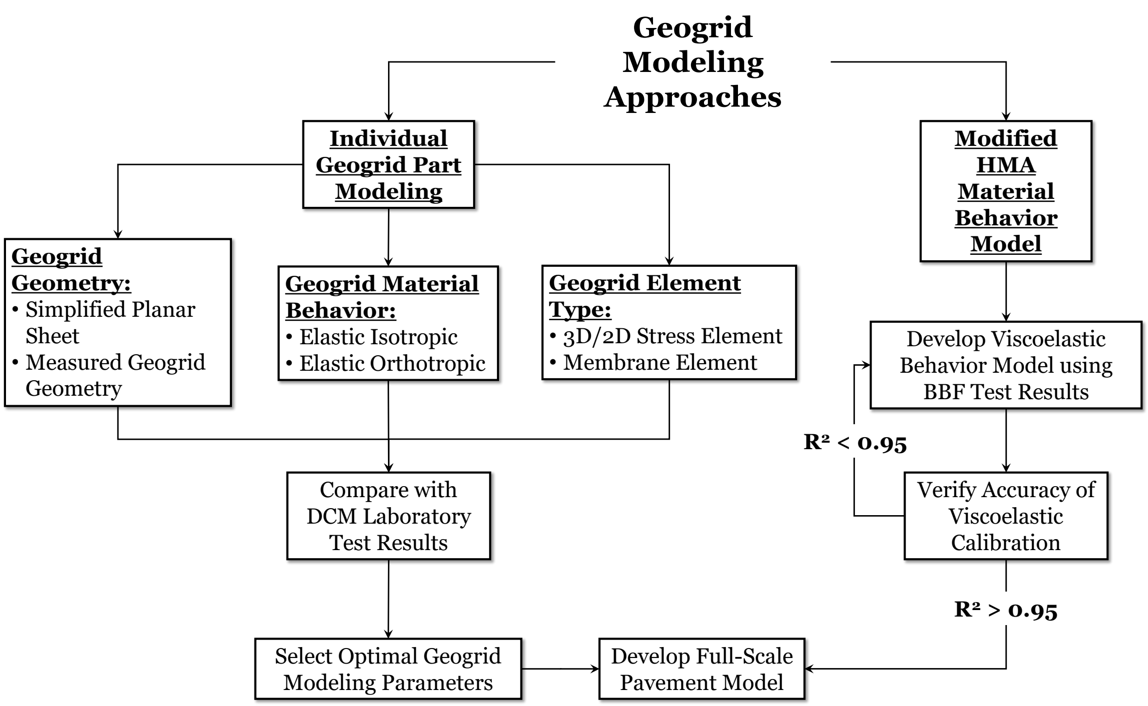

Figure 41. General overview of the adopted geogrid modeling approaches.

Finite Element Modeling Using Elastic Geogrid Reinforcement. The first approach considered in this study considers several different model parameters (geometry, element type, material behavior model) to find the optimal set of parameters compared with the laboratory testing. The same model parameters, after validation with laboratory testing, would then be used to simulate the full-scale pavement response. The laboratory test used for validation was the DCM test and was simulated using a 3DFEM. This test was selected due to its ability to depict and identify the change in viscoelastic properties due to the geogrid reinforcement. Additionally, laboratory compressive tests have been primarily used in literature for validation of geogrid FEM studies [12], [79].

Geogrid Geometry Variations. Two FEM geometry modeling procedures of the geogrid were selected: (i) simplified sheet method and (ii) realistic geogrid geometry method. Both methods were considered due to their use in literature [79]. The simplified sheet approach does not consider the openings in the geogrid reinforcement, whereas the latter approach uses actual geogrid geometry dimensions and considers the geogrid openings. When geogrid openings are considered in the geometry, HMA material properties are assigned to the elements in each geogrid opening. These two approaches are illustrated in Figure 42.

.

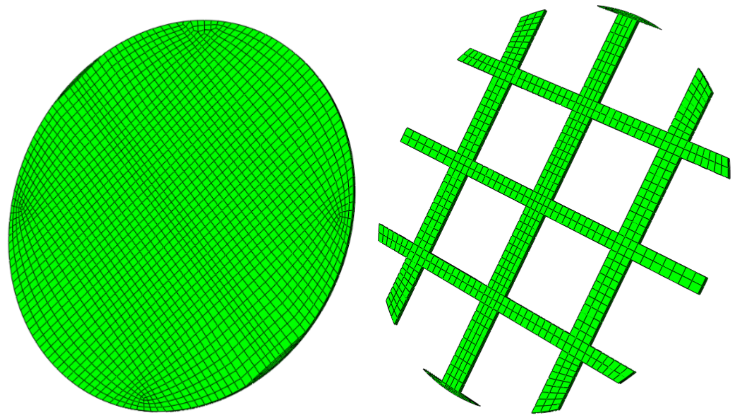

Figure 42. Different three-dimensional geogrid geometry modeling approaches: (a) simplified sheet and (b) actual geogrid (with HMA elements filling in all openings).

Geogrid Element Type. In addition to the different geogrid geometry modeling approaches, two different element types were considered. These elements types were chosen based on the practices used in previous studies [70], [75]–[78]. The element types considered were membrane elements and 3D stress element (also known as brick or solid elements). The main difference between element types is that membrane elements do not transmit out-of-plane stresses and have no flexural rigidity. Finally, two constitutive models were considered to define the material behavior of the geogrid reinforcement. A further description of the material constitutive behavior models for geogrids is explained in the following subsections.

Geogrid Material Constitutive Behavior. A linear elastic isotropic material behavior and linear elastic orthotropic material behavior were selected. The linear elastic material behavior was discussed in a previous section with regards to pavement system layers. A linear elastic orthotropic material consists of a material with a direction-dependent stiffness. For this material behavior, the material parameters must be defined for all dimensions considered in the FEM. These moduli define the elastic compliance matrix as shown in Equation 21.

$$\begin{Bmatrix} \varepsilon_1 \\ \varepsilon_2 \\ \varepsilon_3 \\ \gamma_{12} \\ \gamma_{13} \\ \gamma_{23} \end{Bmatrix} = \begin{bmatrix} 1/E_1 & -\nu_{21}/E_2 & -\nu_{31}/E_3 & 0 & 0 & 0 \\ -\nu_{12}/E_1 & 1/E_2 & -\nu_{32}/E_3 & 0 & 0 & 0 \\ -\nu_{13}/E_1 & -\nu_{23}/E_2 & 1/E_3 & 0 & 0 & 0 \\ 0 & 0 & 0 & 1/G_{12} & 0 & 0 \\ 0 & 0 & 0 & 0 & 1/G_{13} & 0 \\ 0 & 0 & 0 & 0 & 0 & 1/G_{23} \end{bmatrix} \begin{Bmatrix} \sigma_{11} \\ \sigma_{22} \\ \sigma_{33} \\ \sigma_{12} \\ \sigma_{13} \\ \sigma_{23} \end{Bmatrix} \quad (21)$$

Where,

E_{ii} = Elastic Modulus in the principal direction i

ν_{ij} = Poisson's ratio in the ij direction

G_{ij} = Shear modulus in the ij direction

ε_{ii} = Strain in the principal direction i

γ_{ij} = Shear strain in the ij direction

σ_{ij} = Stress in the ij direction

The orthotropic material behavior was adopted for geogrid reinforcement because the stiffness is assumed unequal in all directions. The geogrid type adopted for the model comparison and validation was F-25-100-A. This geogrid type was chosen because the Young's modulus in both principal directions parallel to the thickness of the geogrid (i.e. E1 and E2) were available in literature [112]. For this geogrid type (F-25-100-A), the Young's Modulus was determined to be 73,000 MPa according to literature [112]. That value was used as the modulus values in both tensile principal directions (i.e E1 and E2). The stiffness orthogonal to the geogrid thickness (i.e. E3) was assumed to be significantly different than the tensile modulus parallel to the thickness (i.e. 0.01% of the instantaneous HMA modulus). Based on the moduli of the HMA layer and geogrid reinforcement, this value was assumed to be 1 MPa (i.e. geogrid would fully compress under loading). This assumption was made to replicate the geogrid strand redistribution (and resulting geogrid compression) under loading. Though the geogrid thickness is not significantly large, the FEM of small-scale laboratory testing may incur error due to this variation in compression. Based on these assumptions, the linear elastic orthotropic material constitutive behavior was also considered for the geogrid reinforcement.

Model Calibration and Validation. The various geogrid modeling approaches considered needed to be evaluated for accuracy. Therefore, the different approaches were compared and validated with the experimentally obtained DCM responses for the unreinforced HMA and one geogrid type (F-25-100-A). For this study, the dynamic complex modulus (|E*|) test has been adopted to characterize the viscoelastic behavior of asphalt concrete. The master curves were then developed at 21.1°C using a sigmoidal fit and polynomial time-temperature superposition. The master curves for the unreinforced and geogrid-reinforced HMA mixtures were presented previously in Figure 18. Based on the |E*| master curve, the Prony series parameters can be determined using the curve fitting procedure. The Prony series parameters for the unreinforced HMA mixture are presented in Table 16. It is also acknowledged that the shear and bulk parameters were assumed to be equal based on previous success in literature [12].

Table 18

Prony Series Model Coefficients for P-401 HMA Based on DCM Test Results

N	Prony Series Fitting Parameters		
	G_i	K_i	τ_i
1	-0.1484	-0.1484	2.37E-05
2	0.4086	0.4086	6.93E-04
3	0.3465	0.3465	1.00E-02
4	0.2309	0.2309	0.1741
5	6.72E-03	6.72E-03	0.211
6	0.1239	0.1239	4.102
7	-1.93E-04	-1.93E-04	6.703
8	6.10E-06	6.10E-06	48.77
9	-2.19E-06	-2.19E-06	262.6
10	3.25E-07	3.25E-07	1345

The HMA cylindrical sample, fabricated for DCM testing, was modeled using the same dimensions as outlined in AASHTO T378 for validation of the geogrid modeling approaches. The boundary conditions for the DCM test simulation were simple roller supports at the bottom of the sample. As stated previously, the viscoelastic material was characterized using the Prony Series model determined from the DCM testing on the unreinforced HMA mixture. The geogrid was considered fully bonded and no slippage was allowed. Due to the Prony series dependency on the master curve at 21.1°C, only the DCM test results at this temperature were compared with the FEM. The accuracy of each geogrid modeling approach was determined based on the average percent error of the stress-strain curve from the experimental DCM dataset. The average percent error for each geogrid modeling approach is presented in Table 17.

Table 19

Average Percent Error of Stress-Strain Curve for each Geogrid Modeling Approach

Constitutive Behavior	Planar Sheet			Geogrid Geometry		
	2D-Membrane	3D-Membrane	3D-Brick	2D-Membrane	3D-Membrane	3D-Brick
Isotropic-Elastic	29.48%	29.13%	26.53%	22.88%	20.26%	12.47%
Orthotropic-Elastic	29.48%	29.13%	18.98%	22.88%	20.26%	2.57%

From Table 17, the model approach including the actual geogrid geometry with 3D stress elements and an orthotropic constitutive material behavior was determined as the most accurate method of modeling geogrid reinforcement. The strain response with time and the stress-strain curve obtained from the experimental testing and the 3DFEM at 10 Hz are presented in Figure 43. As can be seen from Figure 43, the model accurately predicts the mechanistic responses in both unreinforced and geogrid-reinforced HMA mixtures. It is acknowledged that slightly higher inaccuracy is found in geogrid-reinforced HMA mixtures. Even though this modeling approach showed success at 10 Hz, another frequency (25 Hz) was also considered to evaluate the accuracy of this approach under different loading conditions. The accuracy of the model under the quicker loading condition also yielded an acceptable average percent error of 4.77%.

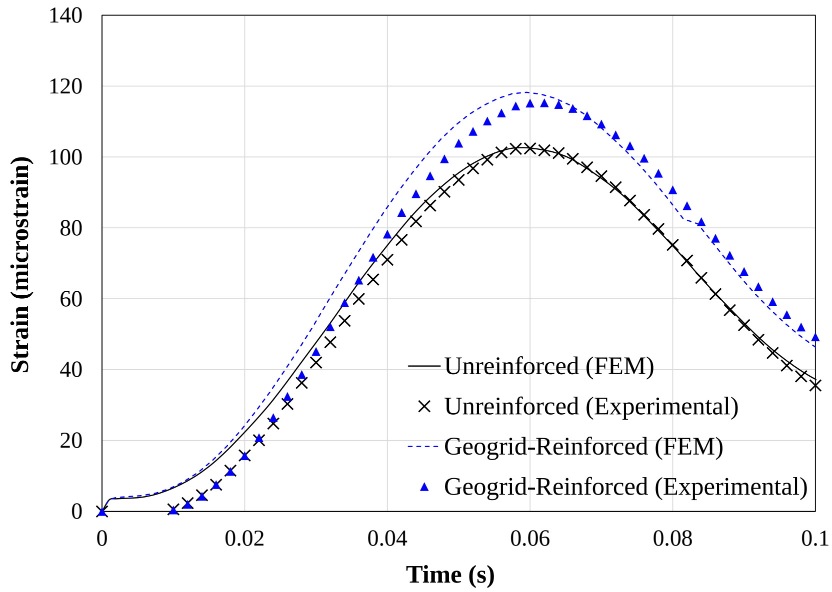

(a)

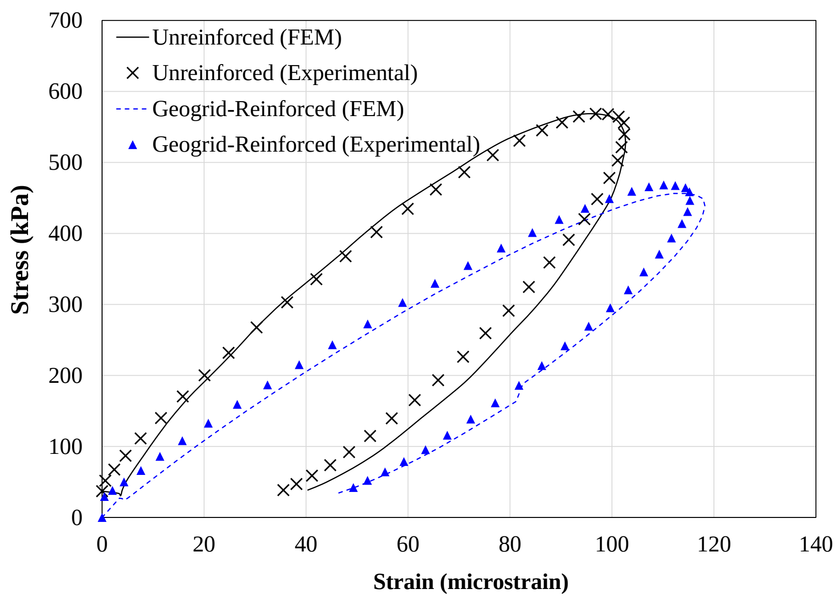

(b)

Figure 43. Comparative view of the (a) time history of strain and (b) stress-strain curve obtained from DCM testing and FE simulations.

Finite Element Modeling Approach Using Modified Hot-Mix Asphalt Properties. The second approach modifies the material parameters used to define the HMA viscoelastic constitutive behavior model to account for the geogrid reinforcement. In order to incorporate the findings from BBF testing, methods of modeling this laboratory test are being investigated. Previously, the BBF testing has been modeled using a Prony Series to quantify the viscoelastic behavior developed from BBF test results [110]. This method is anticipated as a feasible method to quantify the impact of geogrid reinforcement in HMA. Because the benefits of geogrids are primarily evident in the relaxation of the HMA materials, each geogrid-reinforced HMA will be defined using a unique Prony-Series model.

Prony Series Model Fitting. The Prony series models have been developed for the unreinforced and geogrid-reinforced HMA specimens using the BBF results laboratory results at 20°C. This procedure has been implemented in literature for defining the viscoelastic behavior of HMA in FEM [110]. The intermediate testing temperature was selected due to its recommendation in respective specifications (ASTM D7460 and AASHTO T321) to ensure appropriate modulus degradation response. For this study, the tolerance level for accuracy determination of the Prony series model was defined in terms of the coefficient of determination (R^2) greater than 95% for the equality line between predicted and measured |E*|. Additionally, a unique Prony series model was developed for each geogrid embedment depth (i.e. one-half depth and one-third depth) specimens. It is acknowledged that, in this method, the geogrid or its respective properties will not be modeled and the benefits of the geogrid will be incorporated within the Prony Series model. Additionally, the number of parameters will remain constant across all HMA mixtures in order to maintain consistency. The fitted parameters for each HMA mixtures is provided in Table 18 and the equality lines between predicted and laboratory-tests |E*| values are presented in Figure 44 and Figure 45.

Table 20

Prony Series Parameters Determined for each HMA Mixture with Different Geogrid Embedment Depths

Prony Series Coefficients for each HMA Mixture							
F-25-100-A (HD)		F-25-200-A (HD)		F-30-100-B (HD)		B-25-90-L (HD)	
E_i	τ_i	E_i	τ_i	E_i	τ_i	E_i	τ_i
2327.587	0.000345	2203.662	0.000381	2480.399	0.000403	2616.008	0.000465
811.3706	0.004937	713.8169	0.005184	857.2189	0.00648	678.4299	0.005097
0.1	0.002029	0.1	0.002029	0.1	0.002029	0.1	0.002024
468.8305	0.055869	371.1854	0.055989	553.6188	0.044419	630.1945	0.049618
258.6508	0.669585	264.7395	0.674798	284.3243	0.500859	635.8144	7.333193
E_o	1547.649	E_o	1307.176	E_o	1377.712	E_o	1427.827
F-25-100-A (TD)		F-25-200-A (TD)		F-30-100-B (TD)		B-25-90-L (TD)	
E_i	τ_i	E_i	τ_i	E_i	τ_i	E_i	τ_i
3114.168	9077.363	3114.168	9077.363	1377.559	0.001385	1348.789	4673.429
6369.01	9752.691	6369.01	9752.691	523.5768	0.016318	9636.028	1599.914
540.7879	0.059454	572.2171	0.053564	0.1	0.002589	9558.436	2092.909
1403.957	0.002751	1043.313	0.002249	327.255	0.14161	1410.928	0.004232
7478.334	4061.932	7478.334	4061.932	10021.00	32.49744	9138.743	8388.097
E_o	2690.678	E_o	2609.039	E_o	1687.038	E_o	3316.174

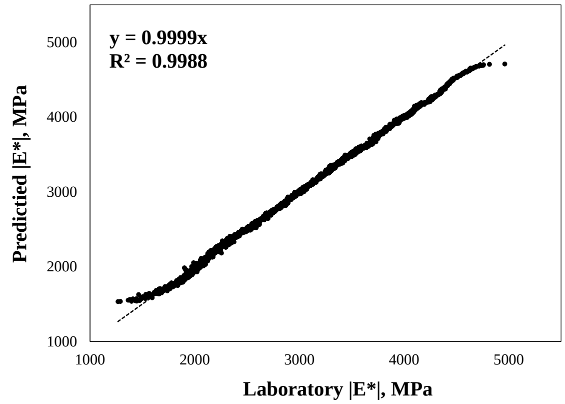

(a)

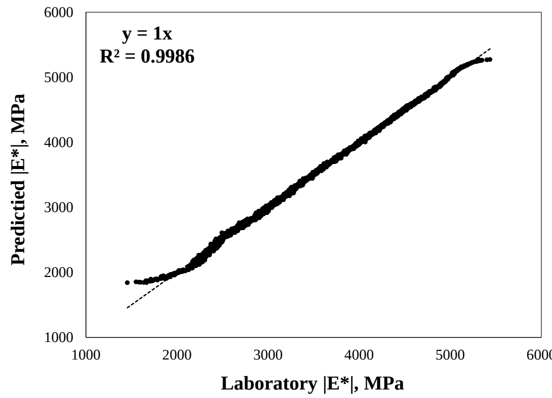

(b)

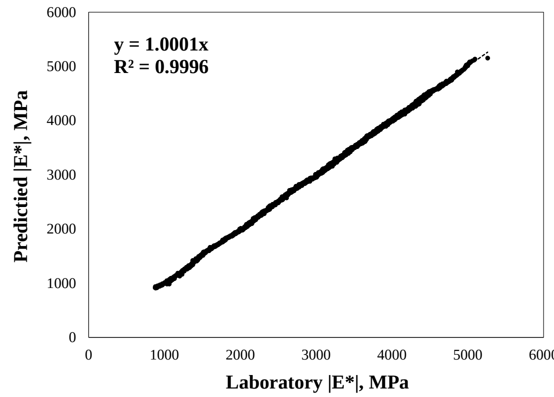

(c)

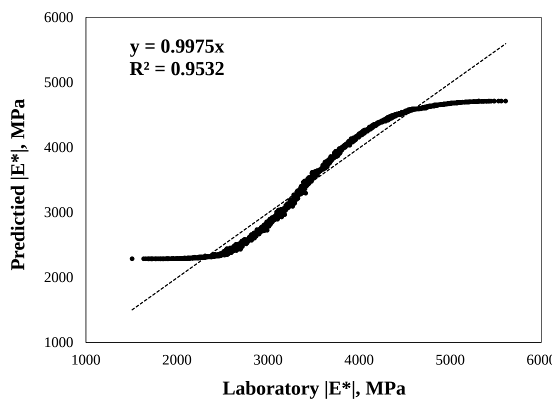

(d)

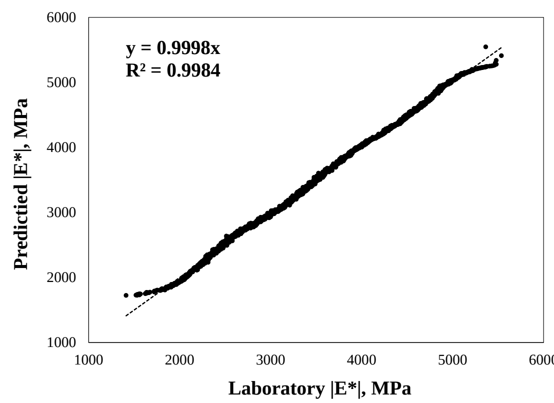

(e)

Figure 44. Equality lines for laboratory and predicted $|E^*|$ for geogrid-reinforced HMA with geogrids at embedded at one-half depth when (a) control or unreinforced HMA mixture, (b) F-25-100-A, (c) F-25-200-A, (d) F-30-100-B, and (e) B-25-90-L.

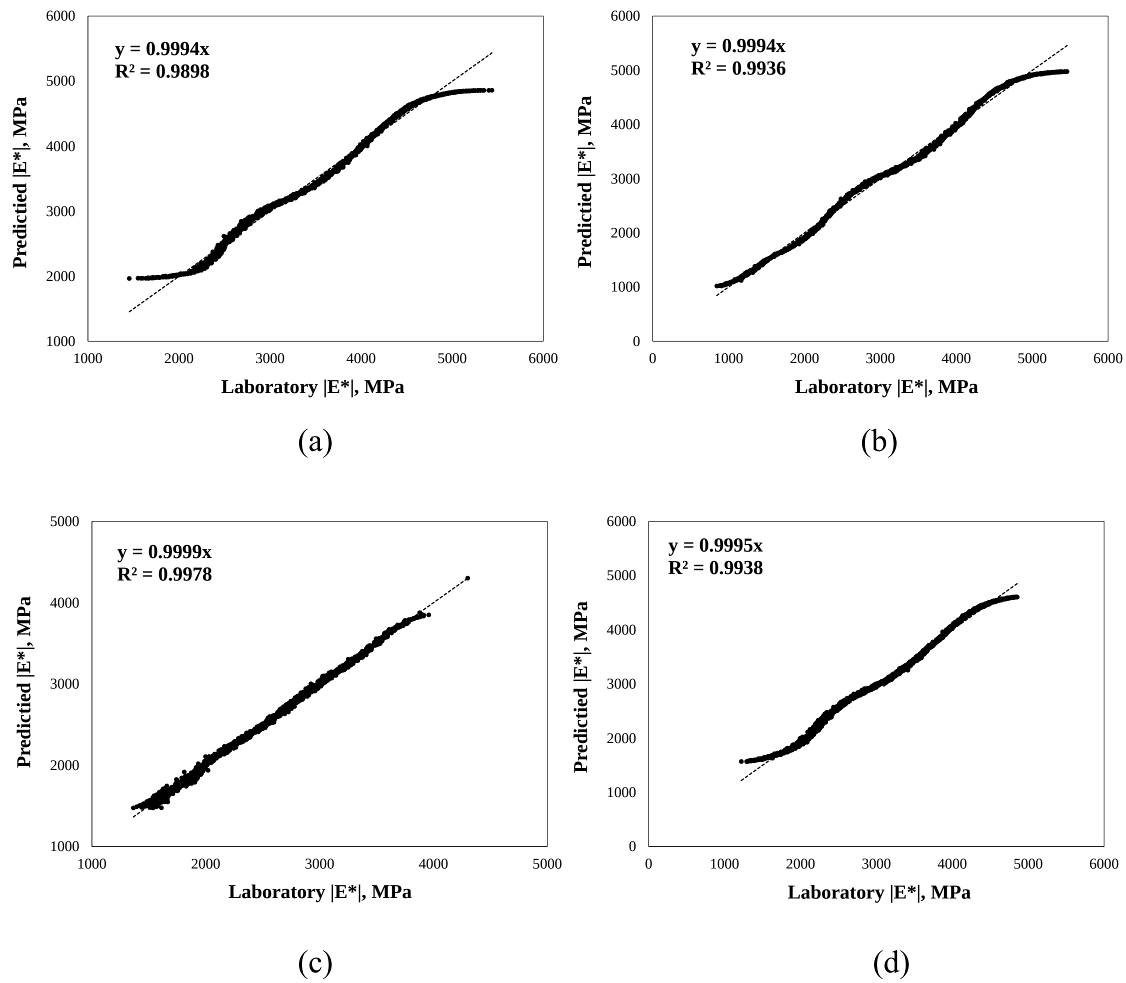

Figure 45. Equality lines for laboratory and predicted $|E^{*}|$ for geogrid-reinforced HMA with geogrids at embedded at one-third depth (measured from the bottom of the specimen) when (a) F-25-100-A, (b) F-25-200-A, (c) F-30-100-B, and (d) B-25-90-L.

Pavement System Simulations

Static Loading Analysis. For this study, a three-dimensional Finite Element Model (3DFEM) was considered for the purpose of modeling pavement systems with geogrid-reinforced HMA layers using the elastic geogrid modeling approach. A static analysis was considered using the elastic geogrid modeling approach to evaluate a change in tensile strain response due to the addition of geogrids in HMA pavement system layers under aircraft loading. Additionally, a static analysis was considered because of its close similarity to the approach used in pavement structural design [113]. Thus, the static analysis was considered sufficient for the elastic geogrid modeling approach.

Further, justifications for the use of a 3DFEM for geogrid-reinforced systems are described in literature [66], [114], [115] and are summarized as follows:

1. Allows for the flexibility of including realistic geogrid geometry and complex geogrid-asphalt interaction;
2. Is preferred when the verification of the numerical model results with the laboratory or field test results is desired; and
3. Better reflects the integrated behavior of the composite pavement system materials under traffic loads of different configurations.

Pavement System Geometry and Boundary Conditions. In the static analysis, a pavement system was modeled using a three-dimensional (3D) axisymmetric quarter-model. A 3DFEM was used to include the effects of geogrid geometry in the static simulation. The 3DFEM consisted of three main pavement layers: HMA layer (or geogrid-reinforced HMA layer), base layer, and subgrade. The thickness of the HMA and base layers were assumed to be 4 and 7 inches, respectively. The subgrade thickness was chosen to be large enough to neglect any boundary effects. The thicknesses, Young's modulus, and adopted constitutive models for each material are presented in Figure 46. The adopted material constitutive behaviors are explained in detail in the following subsections.

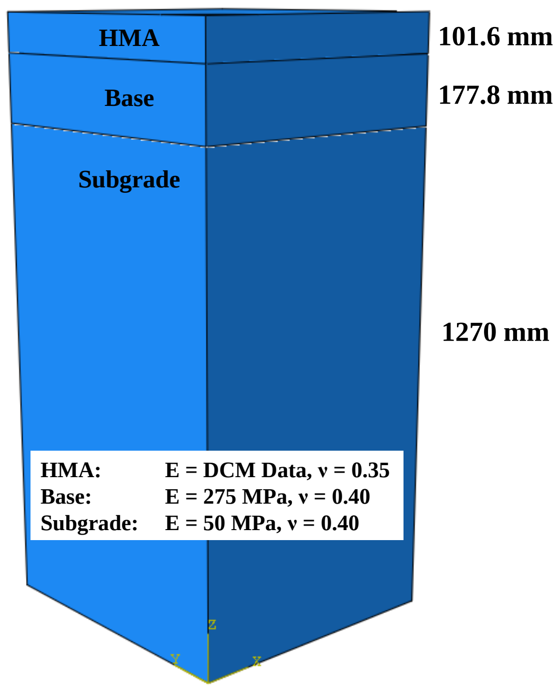

Figure 46. Cross-sectional dimensions, material properties, and modeled geometry of unreinforced flexible pavement system.

The boundary conditions for the surfaces opposite from the loading system and the bottom surface were assumed to be fixed in all directions. This boundary condition has shown success in the modeling of pavement systems [97]. The surfaces closest to the loading system were restrained from out of plane displacements. The axisymmetric FEA approach has shown success in being able to capture the responses under static loading [79].

To optimize the integrated response of geogrid-reinforced pavement, this study varies geogrid embedment depth to assess the variations in the overall pavement system performance. Three different geogrid depths—one-half (HD), one-third (TD), and one-quarter (QD)—measured from the bottom were considered. No depths lower than QD were considered because this would not be feasible for field construction of HMA layers with geogrid reinforcement. As in the DCM simulation, the geogrid was assembled into the FE geometry without slippage at the interface between geogrid and HMA material. For comparison and evaluation, the critical tensile strain in the HMA layer (i.e. tensile strain at the bottom of the HMA layer) was used. Additionally, different opening sizes (25 mm and 30 mm) were considered in the FEM to replicate the opening sizes used in this study (Table 5). For the evaluation of different geogrid opening sizes on pavement system performance, the Young's modulus value for geogrid reinforcements was obtained from literature and used as the FEM input [112].

However, as mentioned previously, the accuracy of the Young's modulus value for geogrid reinforcements is unknown and not commonly measured or reported. Therefore, a sensitivity analysis was conducted on the Young's modulus value to better understand the impact of geogrid properties on the pavement system responses. The Young's modulus value obtained from literature (73,000 MPa) was used as the basis for the sensitivity analysis [112]. An upper and lower Young's modulus value was investigated by using 150,000 MPa and 7,300 MPa, respectively.

Loading Conditions. Based on the validated modeling approach of geogrid reinforcement in HMA layers, aircraft traffic loading was simulated on the full-scale pavement system. The aircraft tire was modeled using a circular tire footprint with a radius of 221 mm and a tire pressure of approximately 1450 kPa. This loading configuration is similar to the aircraft loading utilized in literature [80].

Static Condition Results. The critical tensile strains obtained with depth for each geogrid opening size and tensile modulus are presented in Table 19 and Table 20, respectively. The reduction in tensile strain at the bottom of the HMA layer from the unreinforced pavement system is also provided for ease of interpretation. From the 3DFEM, it was observed that the use of geogrid reinforcement in HMA layers reduced the critical tensile strain when embedded below the neutral axis. Further, it was observed that the geogrid embedded depth influenced the impact on the critical tensile strain in the HMA layer. It was found that geogrids embedded at greater depths resulted in a greater reduction in critical tensile strain. The finding of the impact of geogrid depths on the reduction in critical tensile strain (and fatigue life) shows agreement with previous laboratory experiments that investigate the impact of geogrid depth [18]. It is noted, however, that the magnitude of strain reduction appears to be greater than what is physically achievable in field pavement systems. It was also observed that a localized tensile strain directly above the geogrid reinforcement was observed in the 3DFEM; however, this response is considered a limitation of the model. A contour plot of the tensile strains in an unreinforced and geogrid-reinforced HMA layer is presented in Figure 47. This response was considered a limitation of the FEM rather than a meaningful response because the magnitude of the localized tensile strain was similar to that of the unreinforced pavement system, which would indicate similar service life if the crack were to initiate and propagate from above the geogrid. This phenomenon, however, is not reflected in previous laboratory experiments [18], [21].

Additionally, the geogrid properties were varied to gain a better understanding of the overall impact on the FEM pavement responses. From Table 19, it can be observed that the geogrid opening size had little impact on the overall pavement response. With a change in opening size of 5 mm, the reduction in tensile strain varied by less than three percent. Therefore, the FEM was not able to capture an impact due to opening size. The impact of tensile modulus on the FEM pavement responses were also evaluated and are presented in Table 20. As can be seen from Table 20, the geogrid tensile modulus had very little impact on the FEM pavement system strain response. The greatest variation in tensile strain reduction was approximately 2%. Therefore, the FEM was also not capable of capturing an impact due to the tensile modulus of the geogrid reinforcement. This may be due to the fact that the tensile modulus of the geogrid was much greater than the modulus of the HMA material.

Table 21

Critical Tensile Strains Obtained from 3DFEM for Different Opening Sizes

Pavement System Model	Geogrid Property: Opening Size			
	25 mm		30 mm	
	Tensile Strain in HMA layer (microstrain)	Tensile Strain Reduction	Tensile Strain in HMA layer (microstrain)	Tensile Strain Reduction
Unreinforced	425.8	-	425.8	-
Quarter-Depth	399.6	6.15%	405.6	4.75%
Third-Depth	135.8	68.11%	146.7	65.56%
Half-Depth	96.1	77.43%	99.9	76.53%

Table 22

Critical Tensile Strains Obtained from 3DFEM for Varying Geogrid Young's Modulus Values

Pavement System Model[1]	**Geogrid Property: Young's Modulus**					
	7,300 MPa		**73,000 MPa**		**150,000 MPa**	
	Tensile Strain in HMA layer (microstrain)	**Tensile Strain Reduction**	**Tensile Strain in HMA layer (microstrain)**	**Tensile Strain Reduction**	**Tensile Strain in HMA layer (microstrain)**	**Tensile Strain Reduction**
Unreinforced	425.8	-	425.8	-	425.8	-
Quarter-Depth	399.6	6.15%	394.4	7.36%	390.6	8.25%
Third-Depth	135.8	68.11%	134.6	68.39%	135.2	68.25%
Half-Depth	96.1	77.43%	95.0	77.70%	94.9	77.72%

[1]Geogrid depth is measured from the bottom of the HMA layer

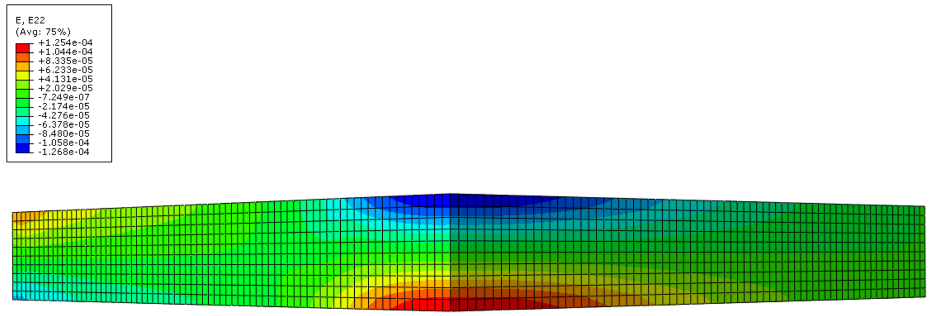

(a)

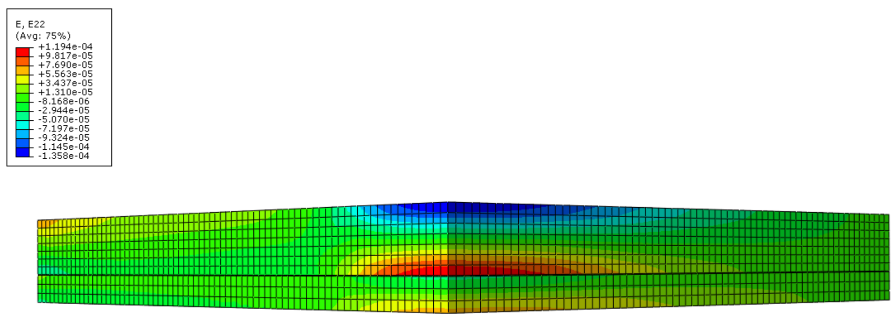

(b)

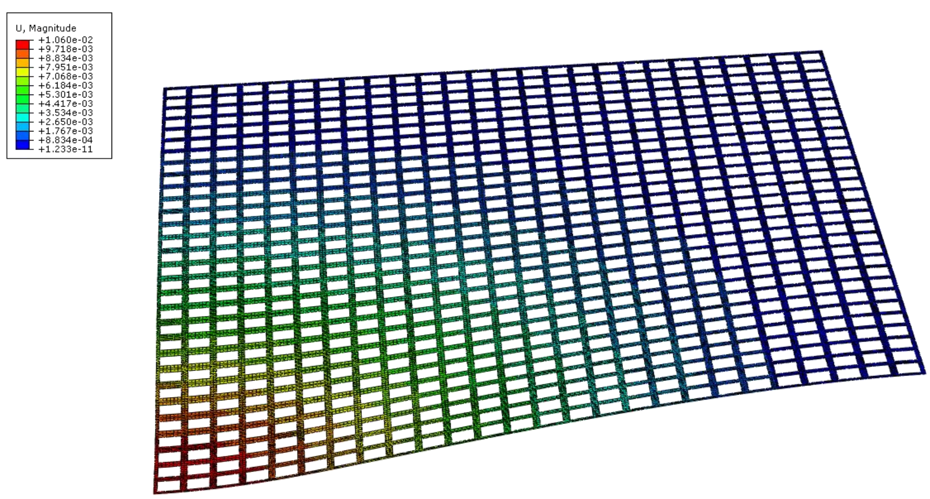

(c)

Figure 47. Tensile strain responses in HMA layers (a) unreinforced, (b) geogrid-reinforced and (c) vertical deformation in deformed geogrid reinforcement from 3DFEM.

Dynamic Loading Analysis. A dynamic loading condition was also considered to investigate the behavior of geogrid-reinforced HMA under repeated aircraft loading. Repeated loading with viscoelastic properties has been readily utilized in FEM for the evaluation HMA materials [116]–[118]. The previous FEM analysis conducted in this study utilized static analysis because of the uncertainty in the ability of the geogrid modeling approach to capture the viscoelastic behavior of geogrid-reinforced HMA under dynamic cyclic loading. In contrast, however, the modified viscoelastic properties developed based on the BBF performance data is assumed to be capable of simulating the viscoelastic behavior of geogrid-reinforced HMA. This assumption is made because the calibrated FEM input parameters were developed based on the viscoelastic performance of geogrid-reinforced HMA under repeated cyclic loading. A description of the dynamic loading FEM system is presented in the following subsections.

Pavement System Geometry and Boundary Conditions. The dynamic analysis pavement system was modeled to replicate the static analysis with three distinct pavement layers: HMA layer (or geogrid-reinforced HMA layer), base layer, and subgrade. The thicknesses of the HMA and base layers were also kept constant at 4 and 7 inches, respectively. The subgrade thickness was chosen to be large enough to neglect any boundary effects. The HMA and geogrid-reinforced HMA layers were modeled using the modified HMA approach outlined in Figure 41. This approach was considered for the dynamic analysis because it was considered the most accurate method in determining the viscoelastic behavior of geogrid-reinforced HMA. This approach utilized laboratory test data that included flexural testing results, in which the properties of geogrid are most definitive. Because of the homogeneity between layers and the lack of three-dimensional geogrid geometry modeling in the modified HMA approach, a two-dimensional finite element model (2DFEM) was used for computational efficiency. The thicknesses, Young's modulus, and adopted constitutive models for each material remain the same as the static analysis (presented previously in Figure 46*Figure 46*). A roller boundary condition was assumed for the sides of the pavement system and the bottom surface was assumed to be fixed in all directions. This boundary condition has shown success in the modeling of pavement systems [97].

Loading Conditions. For the dynamic analysis, the aircraft loading remained consistent with the loading used in the static analysis. The aircraft tire was modeled using a circular tire footprint with a radius of 221 mm and a tire pressure of approximately 1450 kPa. This loading configuration is similar to the aircraft loading utilized in literature [80]. The pulse of the aircraft loading was modeled using a haversine amplitude with a loading time of 0.1 seconds. This loading time was used in order to replicate the same loading amplitude as the BBF laboratory test data. The BBF laboratory test loading amplitude was replicated to facilitate comparisons and remove the uncertainty of HMA recovery.

Dynamic Loading Results. The critical tensile strains were measured with time, similar to the static loading analysis. The peak strain is plotted with time for each unreinforced and geogrid-reinforced HMA mix in Figure 48.

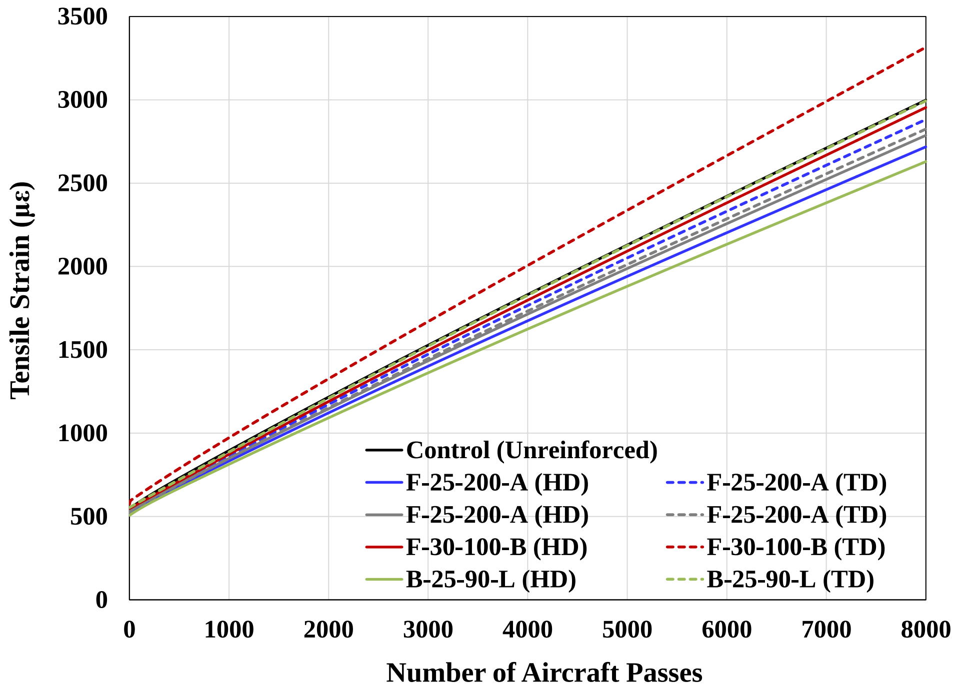

Figure 48. Tensile strain values with time for each HMA mixture considered in the modified HMA approach analysis.

As can be seen from Figure 48, four of the geogrid-reinforced HMA mixes provided lower critical tensile strains at the end of 8000 aircraft passes. It is noted that such high tensile strains are observed due to the use of aircraft loading within the FEM without fracture modeling. The overall increase in tensile strains with time results in modulus degradation and eventual pavement failure. Therefore, to gain a better understanding of the modulus degradation and the approach to failure, comparisons are made between the FEM and BBF responses.

To facilitate a comparison between FEM and BBF results, a ratio was developed between the modulus at each aircraft pass to the average modulus when the BBF laboratory sample failed. The ratio (P_f) can be practically interpreted as a measure of pavement structural integrity with time. The percentage is presented in Equation 22 and the average flexural stiffness value at failure for each HMA mixture is presented in Table 21. The percentage is plotted with time in Figure 49 for each unreinforced and geogrid-reinforced HMA mix.

$$P_f = \frac{E_{BBF-Failure}}{E_{FEM-Pass\ x}} \times 100 \quad (22)$$

Where,

P_f = Percentage of HMA failure

$E_{BBF\text{-}Failure}$ = Average modulus at failure during BBF laboratory testing

$E_{FEM\text{-}Pass\ x}$ = Modulus obtained from tensile stress and tensile strain FEM response at a specific aircraft pass

Table 23

Average Modulus at Failure during BBF Laboratory Testing for Each HMA Mixture

HMA Mixture Type	$E_{BBF\text{-}Failure}$
Control	1395.96
F-25-100-A (HD)	1600.38
F-25-100-A (TD)	1282.67
F-25-200-A (HD)	755.27
F-25-200-A (TD)	844.45
F-30-100-B (HD)	1634.29
F-30-100-B (TD)	1536.03
B-25-90-L (HD)	1532.04
B-25-90-L (TD)	1290.92

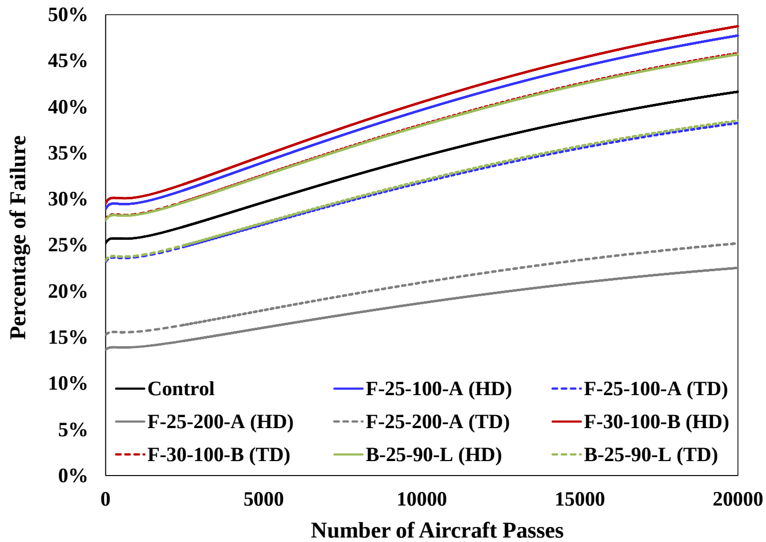

Figure 49. The percentage of failure experienced due to aircraft loading with time for each HMA mixture considered in the modified HMA approach analysis.

From Figure 49, it can be observed that several geogrid-reinforced HMA mixes outperformed the unreinforced HMA mixes when evaluating based on P_f. The high tensile geogrid (F-25-200-A) outperformed all other HMA mixtures after 20000 aircraft passes. Therefore, it appears the tensile strength of the geogrid may significantly impact the pavement system performance under heavy vehicle loading. It was also found from Figure 49*Figure 49* that the trends associated with embedment depth followed a similar pattern to the laboratory BBF performance data (with the exception of F-25-200-A). This finding provides some justification towards the use of modified viscoelastic properties in geogrid modeling.

Chapter 6

Cost Evaluation of Geogrid-Reinforced HMA

The goal of this chapter is to determine if the use of geogrid reinforcements in HMA layers is cost-effective with respect to the achievable increase in service life. This chapter utilizes Life-Cycle Cost Analysis (LCCA) as a method for evaluating the cost-effectiveness and has been readily used in literature for project cost-evaluation [119]. This chapter discusses the general background information of LCCA and the critical components for conducting a LCCA. This chapter also discusses the methodology and assumptions adopted in this study for LCCA of geogrid-reinforced HMA. Finally, the results of the LCCA are presented under varying economic and construction conditions.

Background

Project Costs. Project costs can be classified as two different cost elements: direct costs and indirect costs. Direct costs are costs that can be directly related to a single object or task (e.g., cost of asphalt), whereas indirect costs are costs that cannot be easily quantified to a specific task (e.g., costs of future rehabilitations). Both forms of cost must be included in the overall project cost analysis process. Several methods exist for estimating the direct and indirect costs, including but not limited to the Area Estimation method and Parametric Cost Estimation method.

The Area Estimation method is a cost estimation technique that utilizes areas and volumes with unit cost tables to predict the overall cost of the project. This method has the potential to implement further complexities for a more accurate estimation. These complexities could be geographical cost adjustments, inflation rates, economies of scale adjustments, or special design/site conditions adjustments. This method, through the implementation of several complexities, is considered a fairly accurate method and is readily utilized when data of only the physical layout of the construction project is provided.

The Parametric Cost Estimation method is an estimation technique that implements services and disciplines into the cost estimation. This technique provides an even more accurate method due to its inclusion of services in the estimation process. For the parametric cost estimation method, services that are readily implemented together are given a cost rate. This cost rate is then combined with the cost of the material needed to develop an overall cost of the project. These cost estimates are utilized universally and provide accurate estimations of the overall project cost.

The concepts of direct and indirect costs are used in LCCA to estimate both initial and future costs. In the context of pavement systems, initial costs are those that are incurred at the start of a project, whereas future costs are costs associated with future rehabilitation or reconstruction. These costs cannot be directly compared due to the changing utility value of money with time. Therefore, there is a need to make all costs and benefits time-equivalent through the use of a discount rate.

Discount Rate. A discount rate is used to determine the time-equivalent economic value of costs. The cost valuation of rehabilitation costs depends on two major components: (i) opportunity cost of investment and (ii) inflation. These two factors have their own distinct discount rate future cost valuation. Due to the complexities of using two different discount rates, one simplified discount rate has been developed and used for present-dollar cost valuation, referred to as the real discount rate [119], [120]. The equation for the real discount rate is provided in Equation 23.

$$i = \frac{i' - f}{1 + f} \tag{23}$$

Where,

i = real discount rate

i' = nominal discount rate

f = inflationary rate

The real discount rate has then been shortened to be the difference between the nominal discount rate and the inflationary rate. The shortened equation is readily utilized in practice by different agencies [119], [120].

Service Life Estimation. The service life is the expected lifespan of the construction project and is used during the valuation process in the LCCA. The service life adopted for each analysis is dependent on each individual construction project. For conventional flexible pavement systems, an expected service life of approximately 20 years has been used in literature [121]. The 20-year expected service life has been instituted in this analysis for the unreinforced HMA. The extension in service life due to geogrid reinforcement, however, is unknown, highly variable, and dependent on several factors including geogrid type, environment, construction procedures, etc.

Probabilistic approaches have been developed to better predict variables with high variability. These methods have been readily implemented in the field of finance to better account for inherent portfolio risk [122], [123] and have become accepted in the field of engineering for life-cycle cost analysis [124]–[128]. The implementation of a probabilistic approach utilizes probability distributions of ambiguous variables to encompass the inherent variability and risks associated with the input parameters. This simulation technique randomly samples the probability distributions associated with the input parameters and can then be implemented in the LCCA.

Methodology

A life-cycle cost evaluation was considered in this study to determine if the added product and construction costs of geogrid reinforcements in HMA are cost-effective based on the service life of the pavement system. The adopted framework for the LCCA of geogrid-reinforced HMA is provided in Figure 50.

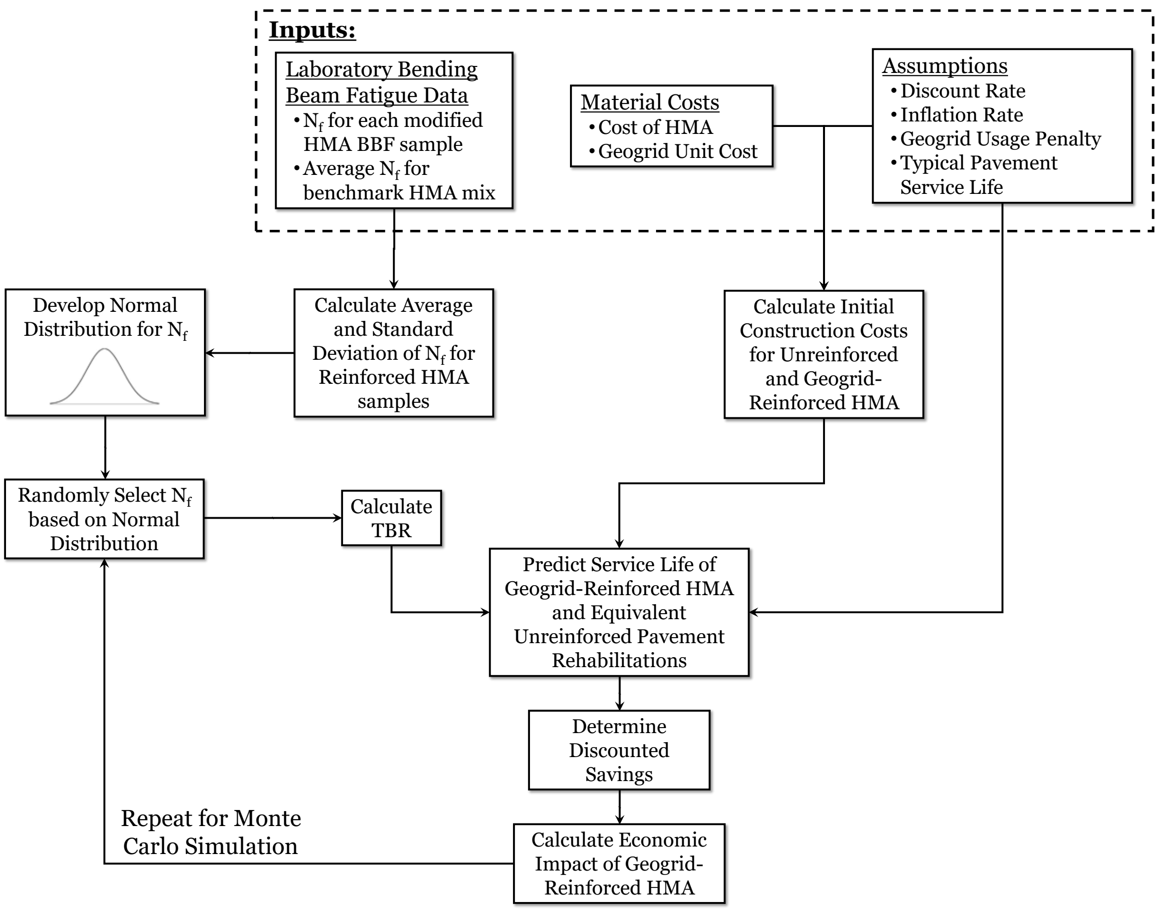

Figure 50. General framework for LCCA of geogrid-reinforced HMA.

The Net Present Value (NPV) of geogrid-reinforced pavement systems can be quantified by determining the costs of avoided future rehabilitations that would be incurred if an unreinforced HMA system were used. The NPV is calculated using three main factors—Initial Cost, Discount Future Costs (DFC), and Predicted Service Life (PSL) of geogrid-reinforced HMA. The calculation of NPV is presented in Equation 24. It is noted that the PSL is used to determine the number of rehabilitations for DFC and Salvage Value (SV) calculations.

$$NPV_R = (IC_U - IC_R) + \sum_1^x (DFC) - SV \quad (24)$$

Where,

NPV_R = Net present value of the geogrid-reinforced HMA pavement system

IC_U = Initial cost of unreinforced HMA pavement system

IC_R = Initial cost of geogrid-reinforced HMA pavement system

DFC = Discounted Future Costs

X = Number of rehabilitations

SV = Salvage Value

Initial Cost Valuation. A combination of two general methods of cost estimation, the area estimation method and the parametric evaluation method, was used in the current study to estimate the overall project cost of an unreinforced and geogrid-reinforced HMA pavement system. The area estimation method, which is commonly implemented by State Highway Agencies (SHAs) for cost estimations of roadway and airfield projects, predicts cost using known unit costs and quantity required to determine total cost for a project [113]. This method is used primarily to determine direct costs (e.g., cost of asphalt for the current project).

For this study, the pavement section geometry adopted in the finite element model (i.e. an HMA layer of four inches) with an assumed lane width of eight feet was used for the LCCA. The cost of HMA was estimated using a unit rate of 100 dollars per ton obtained from literature [129]. The cost of construction was estimated using a percentage of the total cost of HMA, which has been described in literature [130]. For this study, a construction cost estimation rate of 9% was used. The initial costs, based on these assumptions, corresponded closely with HMA construction costs per lane mile found in literature [131]. A summary of the assumed unit costs and conversion rates is presented in Table 22.

Table 24

Unit Costs and Conversion Rates for Geogrids and Hot-Mix Asphalt

Geogrid Type	**Unit Cost ($/yd^2)**	
	Minimum Amount ($)	**Maximum Amount ($)**
F-25-100-A	3.71	3.91
F-25-200-A	6.19	6.51
F-30-100-B	6.13	6.13
B-25-90-L	3.80	3.80
HMA Density Conversion		145 (lbs/ft^3)
HMA Unit Costs		100 ($/ton)
Construction Equipment Costs (percentage of HMA costs)		9%

The construction of geogrid-reinforced HMA includes several complexities during pavement construction. Most of the difficulties associated with geogrid-reinforced HMA are during placement, construction, and recycling. For example, additional machinery and labor is required to roll and place the geogrid between HMA lifts. To account for these costs a Geogrid Penalty Factor (GPF) is applied to the cost of equipment and machinery during construction. This factor can be interpreted as a multiplier to the costs associated with conventional HMA construction due to the added complexity and/or machine modifications as shown in Equation 25.

$$CC_R = GPF \times CC_U \tag{25}$$

Where,

CC_U = Equipment and labor cost for unreinforced HMA pavement system

CC_R = Equipment and labor cost for geogrid-reinforced HMA pavement system

GPF = Geogrid Penalty Factor

There has not been enough research or implementation, however, to determine an accurate GPF to quantify these added complexities. Thus, to minimize the risk of uncertainty, a parametric evaluation was conducted on the GPF. A range of GPF multipliers from three to seven was considered in the parametric analysis to incorporate extreme construction situations.

Discounted Future Cost Valuation. As mentioned previously, the NPV of the added benefits from using geogrid-reinforced HMA can be determined by quantifying the future rehabilitation costs that would be experienced if an unreinforced HMA pavement system were constructed. The future costs consist of the Avoided Rehabilitation Costs

(ARC) and the Salvage Value (SV). This evaluation is graphically represented in Figure 51 and each future cost is described further in the following subsections.

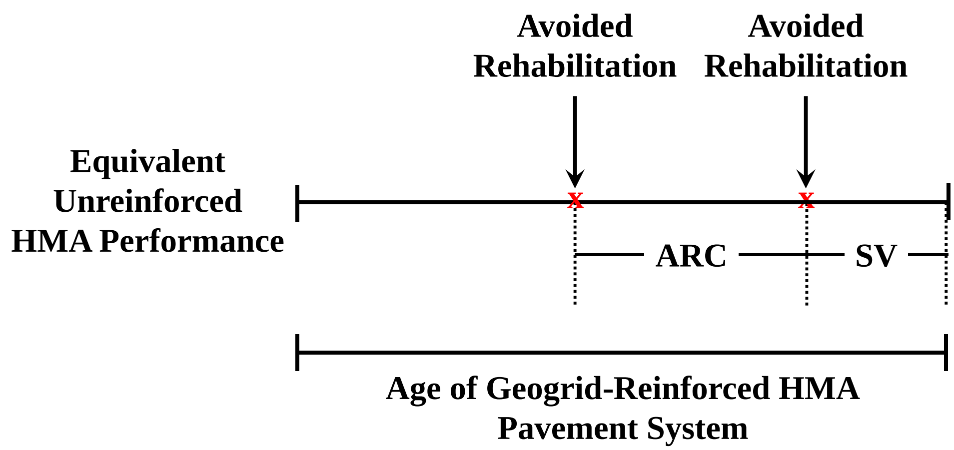

Figure 51. Representation of associated cost savings due to avoided future pavement rehabilitations with respect to pavement service life.

These future costs of pavement systems are due to maintenance and rehabilitation. For this comparative LCCA, the maintenance costs can be ignored because similar maintenance procedures will be required for unreinforced and geogrid-reinforced HMA pavement systems. Therefore, rehabilitation costs are the only future costs considered in the LCCA. For this analysis, a full rehabilitation/reconstruction was considered at the end of each assumed service life of unreinforced HMA pavement systems. The summation of future rehabilitation costs (referred to as Avoided Rehabilitation Costs) can be calculated using Equation 26.

$$\mathrm{ARC} = \sum \mathrm{RC} \times \left(\frac{1}{1+\mathrm{i}}\right)^{\mathrm{n}} \tag{26}$$

Where,

ARC = Avoided Rehabilitation Costs

RC = Rehabilitation cost (in terms of current-dollar)

i = Real discount rate

n = Time at individual rehabilitation activity

The final benefit—SV—is the additional life that is expected based on the most recent rehabilitation, but unaccounted over the service life of the geogrid-reinforced HMA system. The SV was determined using the prorated life method described in literature [113]. The general impact of each cost incurred during the LCCA is presented in Figure 52.

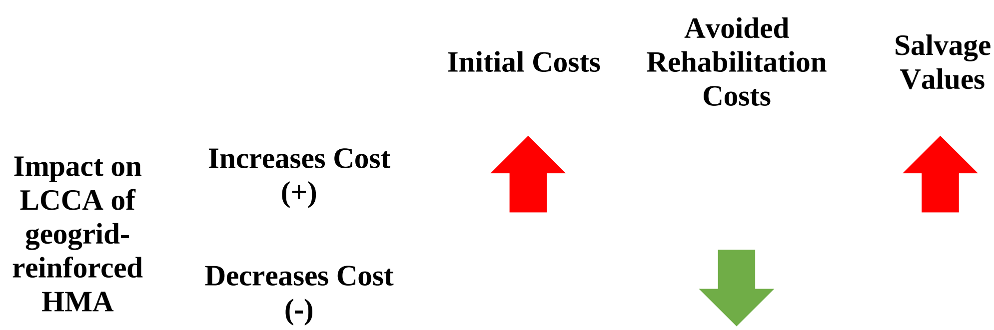

Figure 52. Generalized trend in LCCA due to the use of geogrids in HMA pavement layers.

In all cases of future costs, a discount rate must be assumed as exhibited in Equation 26. The Office of Management Budget has published yearly real discount rates for cost-benefit and cost-effectiveness analysis. For example, a real discount rate of 0.75% was recommended for use by the Office of Management Budget in the year of 2018 for 20 year projects [119]. This rate, however, varies with each year depending on the economic state of the region and future inflation rates. Therefore, for this study, a parametric evaluation was considered on the real discount rate using rates between 1% and 3% based on recent historical rates [119].

Geogrid-Reinforced HMA Service Life. The service life of the geogrid-reinforced pavement system is a vital input for the overall cost evaluation. The service life, however, contains a significant amount of uncertainty due to the lack of implementation and research into full-scale geogrid-reinforced HMA systems [21]. Therefore, a probabilistic Monte Carlo simulation approach was adopted to predict the service life of geogrid-reinforced HMA. For this probabilistic approach, a Gaussian distribution was assumed for the laboratory BBF testing results at 20°C. The probability distribution for each geogrid type and depth is presented in Figure 53 and the distribution parameters are provided in Table 23.

Table 25

Summary of Gaussian Distribution Parameters based on the BBF Laboratory Performance at 20°C

HMA Mixture Type		**Gaussian Distribution Parameters**	
		Mean ($N_{f\text{-}BBF}$)	**Standard Deviation ($N_{f\text{-}BBF}$)**
Control (Unreinforced)	-	68340.33	16409.00
F-25-100-A	One-Half	81835.67	24322.47
	One-Third	162098.33	20156.07
F-25-200-A	One-Half	97544.00	35203.15
	One-Third	260883.00	33569.69
F-30-100-B	One-Half	57083.67	5458.80
	One-Third	34256.00	8467.65
B-25-90-L	One-Half	41802.67	17862.98
	One-Third	197784.67	79497.28

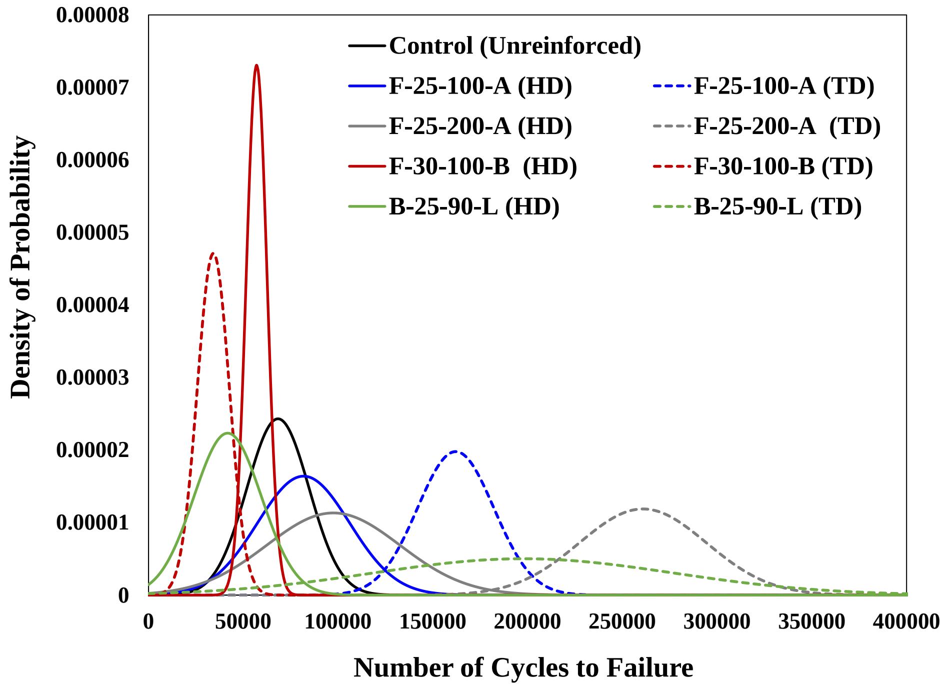

Figure 53. The Gaussian distributions utilized in the Monte-Carlo simulation to determine the number of cycles to failure for each geogrid-reinforced HMA mixture.

A random value for the number of cycles to failure was then selected from the probability distribution. The TBR value was calculated using Equation 27.

$$TBR_{BBF} = \frac{N_{MC}}{Avg.\ N_U} \tag{27}$$

Where,

TBR_{BBF} = Traffic Benefit Ratio based on 4-Point Bending Beam Fatigue test data

N_{MC} = Number of cycles to failure obtained from Monte Carlo random sampling for a specific geogrid type

Avg. N_u = Average number of cycles to failure for the unreinforced HMA BBF sample

The TBR was then multiplied to the assumed unreinforced service life of 20 years to predict the field service life of geogrid-reinforced HMA. This procedure is outlined in the general LCCA framework presented in Figure 50*Figure 50*. For this analysis, 10,000 Monte Carlo simulations were conducted for each geogrid type to minimize the influence from outliers.

Results

The LCCA was conducted on all geogrid types and embedment depths following the aforementioned methodology. As described previously, a combination of parametric evaluations and Monte Carlo simulation were used on the parameters of the LCCA. A summary of the variables used in the LCCA are presented in Table 24.

Table 26

Summary of LCCA Procedures and Variable Ranges

LCCA Variable	Type of Analysis	Range
Geogrid Penalty Factor	Parametric Analysis	3.0 to 7.0
Discount Rate	Parametric Analysis	1.0% to 3.0%
Service Life of Geogrid-Reinforced HMA	Monte Carlo Simulation	Laboratory Test Data

For this study, a set of tables for each parametric condition was developed and provided in Appendix A. In each table, a set of statistics was provided based on the Monte Carlo simulation. In addition to the statistical values, the percentage of simulations that result in a cost benefit (P_{CB}) is also provided in each table. For further understanding, the P_{CB} value is defined in Equation 28.

$$P_{CB} = \frac{N_{CB}}{N} \times 100 \qquad (28)$$

Where,

P_{CB} = Percentage of simulations resulting in cost benefit

N_{CB} = Number of simulations with a positive cost value (cost profit)

N = Number of Monte Carlo simulations (selected as 10,000 for this study)

Based on the LCCA, geogrids showed the ability to be a cost-effective option for HMA pavements. A representation of the LCCA Monte-Carlo simulation results for each geogrid embedment depth are provided in Figure 54. It is noted that each band in Figure 54 depicts an additional avoided rehabilitation that was determined by the analysis. As mentioned previously, the number of avoided rehabilitations was determined based on the Monte Carlo simulation of the service life.

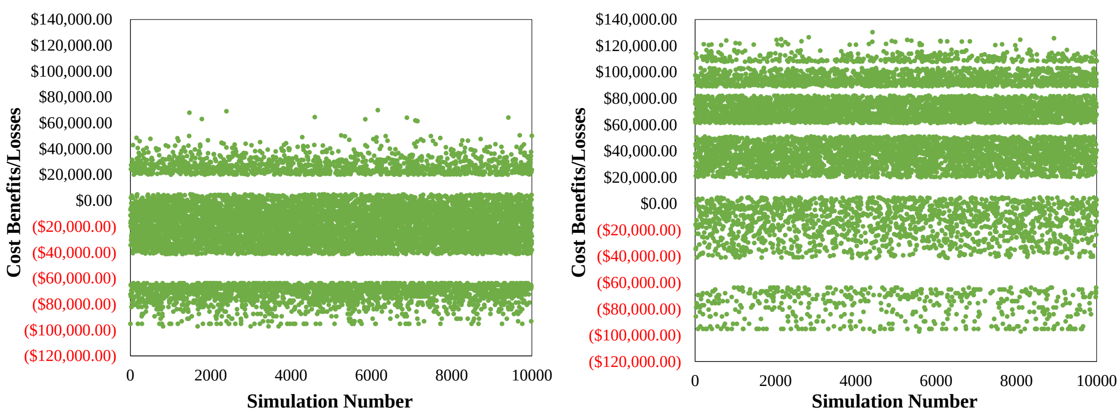

(a) (b)

Figure 54. Representation of the LCCA using the Monte-Carlo Simulation with a GPF of 5.0 and a discount rate of 2.0% for (a) geogrids embedded at half-depth and (b) geogrids embedded at one-third depth.

The cost-effectiveness of geogrid-reinforced HMA was highly dependent on the ability to embed the geogrid at one-third depth (measured from the bottom). The high-strength geogrid (F-25-200-A) showed the greatest increase in cost-effectiveness, with cost benefits ranging from approximately 143,000 dollars to 9,000 dollars depending on the GPF used and economic conditions. Based on the LCCA, no geogrid types embedded at half depth caused an extension in service life that was capable of outweighing the greater initial cost. Though cost benefits are observed are when embedding geogrids at one-third depth (measured from the bottom), it is also vital to investigate the variability incurred during the Monte Carlo simulation.

The P_{CB} can depict the variability and/or risk associated with utilizing geogrids in HMA layers. In fact, this value can be a measure of the reliability of the geogrid-reinforced HMA pavement system. Table 25 shows the range of P_{CB} values based on all the conditions considered in this study.

Table 27

Percentage of Simulations that Resulted in a Cost Benefit for Each Geogrid-Reinforced HMA Mixture

Geogrid Type		**P_{CB} Range**
F-25-100-A	One-Half	0% to 24%
	One-Third	13% to 100%
F-25-200-A	One-Half	0% to 36%
	One-Third	95% to 100%
F-30-100-B	One-Half	0%
	One-Third	0%
B-25-90-L	One-Half	0%
	One-Third	57% to 89%

As can be seen from Table 25, the range of P_{CB} values vary with the geogrid type and embedment depth. The table can be utilized to determine which geogrids contain more risk when used in HMA layers. From Table 25

Table 27, there is the possibility that 100% of the projects using F-25-100-A can result in a cost benefit; however, depending on the economic conditions and cost of construction, there is the potential that only 13% of the projects result in a cost benefit. In comparison, if F-25-200-A is available and used during construction, at least 95% of the projects will result in a cost benefit, regardless of the economic conditions and the cost to construct geogrid-reinforced HMA roadways.

Chapter 7

Overall Ranking of Geogrid-Reinforced HMA Mixtures

This study evaluated the impact of geogrid-reinforced HMA using different laboratory tests and cost-effectiveness measures. The goal of this chapter is to present an overall ranking using the laboratory performance test and LCCA results of the geogrid-reinforced HMA mixtures. This chapter describes the ranking of geogrid-reinforced HMA mixtures based on the laboratory performance of geogrid-reinforced HMA and the results of the LCCA. Additionally, within each section, an explanation is provided regarding the weighting applied to each ranking measure.

Ranking of Geogrid-Reinforced HMA using Laboratory Performance Results

Several sets of laboratory test were performed to evaluate the fatigue cracking performance of geogrid-reinforced HMA. The laboratory tests conducted were the Dynamic Complex Modulus (|E*|) test, the Overlay Test (OT), the Indirect Tension Test (ITS), and the four-point Bending Beam Fatigue (BFF) test. In addition to these performance tests, a compaction analysis (CA) was conducted to investigate the difficulty of compacting geogrid-reinforced HMA. Each laboratory performance test also included variants to investigate different environmental conditions (low temperatures and freeze-thaw cycling).

To conduct an overall ranking of the unreinforced and geogrid-reinforced HMA a base weighting of 1.0 was utilized. Each test was ranked on a scale of 1.0 (worst performing HMA mixture) to 5.0 (best performing HMA mixture). Therefore, the highest total weighted average can be considered best performing HMA mixture based on the laboratory fatigue cracking performance. Further, if two or more HMA mixtures provided similar results (within 20% of the average value) then the ranking was assumed to be equal. Additionally, only the ITS and fracture parameter values at the testing temperature of -10°C were utilized. This is because -10°C is the recommended temperature for ITS testing in the standard protocol and inclusion of all ITS results, which exhibit similar rankings at each testing temperature, may skew the ranking. Finally, it is also assumed in this ranking that embedding the geogrid at a one-third depth (measured from the bottom) is feasible for each geogrid-reinforced HMA mixture. Therefore, this ranking would take the best performance—geogrid at one-half depth or one-third depth (measured from the bottom)—to rank the laboratory BBF performance.

Not all performance tests are equal in their ability to evaluate the performance of geogrid-reinforced HMA. The benefits of geogrid have been documented in literature as evident when fatigue or cracking occurs in the geogrid-reinforced HMA mixture [18], [20]–[22]. Therefore, a reduction of 0.5 was applied to the weighting of the |E*| test and Fatigue Factor (FF) results due to the non-destructive nature of this test as it may not be the best measure for geogrid-reinforced HMA. Additionally, the Compaction Analysis (CA) is a fair measure of the workability of HMA mixtures; however, its interpretation and correlation with field workability is limited [85]. Therefore, the ranking for this test was also reduced to a value of 0.5. Finally, the flexural beam fatigue test has been readily used in literature due to its ability to recognize and initiate the reinforcement mechanisms of geogrid reinforcements [13], [18], [20]–[23], [62]. Therefore, a greater weighting (1.5) was placed on the laboratory BBF performance results because it is assumed, based on literature, that this test is most effective in evaluating geogrid-reinforced HMA. A summary of the weightings and the rationale for additions/reductions are provided in

Table 26. The results of the laboratory performance ranking are provided in Table 27 and Table 28 for unconditioned and conditioned samples, respectively.

Table 28

Summary of Weighting Modifications Applied During Ranking of Geogrid-Reinforced HMA Mixtures

Ranking Parameter	**Addition (+) or Reduction (-) to Weighting**	**Reasoning**
|E*| test and FF analysis	- 0.5	A reduction was applied as this test is a non-destructive laboratory test.
BBF test	+ 0.5	An addition was applied as this test is most prevalently used in literature and is most capable of initiating the reinforcement mechanisms of geogrids [13], [18], [20]–[23], [62].
Compaction Analysis	- 0.5	A reduction was applied as some uncertainty exists with regards to the correlation to field workability of geogrid-reinforced HMA.
Extreme GPF	- 0.5	A reduction was applied as these GPF values are considered the extremes and are less likely to occur during field implementation.
Extreme Discount Rate	- 0.5	A reduction was applied as these discount rates are considered the extremes and are less likely to occur during field implementation.

Table 29

Ranking of Laboratory Performance for Unreinforced and Geogrid-Reinforced HMA Mixtures without Freeze-Thaw Conditioning

HMA Mixture	**Laboratory Performance Test Ranking with Weighting**										**Total (Max=47.5)**
	|E*| Test	**FF (21˚C)**	**OT (25˚C)**	**OT (4˚C)**	**ITS (-10˚C)**	**G_f (-10˚C)**	**Strain Tolerance (-10˚C)**	**BBF (20˚C)**	**BBF (4˚C)**	**CA**	
	(0.5)	(0.5)	(1.0)	(1.0)	(1.0)	(1.0)	(1.0)	(1.5)	(1.5)	(0.5)	
Control (Unreinforced)	3	1	1	1	5	1	1	2	2	4	19.0
F-25-100-A	3	3	4	5	1	2	4	4	5	5	35.0
F-25-200-A	5	5	5	5	4	5	5	5	5	1	44.5
F-30-100-B	3	3	4	5	2	4	3	2	2	2	28.0
B-25-90-L	5	5	4	5	3	4	2	4	5	4	38.5

Table 30

Ranking of Laboratory Performance for Unreinforced and Geogrid-Reinforced HMA Mixtures with Freeze-Thaw Conditioning

HMA Mixture	**Laboratory Performance Test Ranking with Weighting**						**Total (Max=30)**
	|E*| Test	**FF (21°C)**	**OT (25°C)**	**OT (4°C)**	**BBF (20°C)**	**BBF (4°C)**	
	(0.5)	(0.5)	(1.0)	(1.0)	(1.5)	(1.5)	
Control (Unreinforced)	3	1	1	1	1	1	6.0
F-25-100-A	3	3	4	3	5	5	20.0
F-25-200-A	5	5	5	5	3	3	21.0
F-30-100-B	3	3	4	5	5	2	19.0
B-25-90-L	5	5	4	2	3	5	19.0

Ranking of Geogrid-Reinforced HMA using LCCA Results

A cost evaluation was conducted on geogrid-reinforced HMA to investigate if the greater initial construction costs are offset by savings due to prolonged service life. This evaluation was conducted through the use of a Life-Cycle Cost Analysis (LCCA) in which all the current and future costs are considered. A positive cost value implies that the use of geogrids in HMA layers is cost-effective and will result in a positive savings. A negative cost simply implies the opposite in which the use of geogrids in HMA layers are not a cost-effective strategy.

Additionally, from the laboratory performance, it could be observed that each geogrid performed uniquely and thus was evaluated as such to determine if one geogrid was cost-effective whereas another is cost-ineffective. The general LCCA methodology was described previously in Figure 50*Figure 50*. The cost evaluation consisted of different statistical measures including the average cost, maximum and minimum costs, 25th and 75th percentile costs, and the percentage of simulations that resulted in positive cost (P_{CB}). A subset of the cost evaluation measures—the average cost, the maximum achievable cost, and the P_{CB} values—were considered in the ranking of geogrid-reinforced HMA mixtures. Additionally, different GPF values and discount rates were considered in the LCCA. Therefore, in the ranking these variables also need to be considered. Thus, the GPF and discount rate were taken at the low, medium, and high levels for the ranking process.

To conduct an overall ranking of the unreinforced and geogrid-reinforced HMA using the LCCA, a base weighting of 1.0 was utilized (similar to the laboratory performance ranking). Each measure was ranked on a scale of 1.0 (most costly/least profitable HMA mixture) to 5.0 (least costly/most profitable HMA mixture). Therefore, the highest total weighted average can be considered the most cost-effective HMA mixture. The unreinforced HMA mixture was assumed to always have a cost value of zero dollars (or a P_{CB} value of 50%); thus, any cost measure that was positive was ranked higher and any cost measure that was negative was ranked below the control. Further, if two or more HMA mixtures provided similar results (within 10% of the cost measure) then the ranking was assumed to be equal. Finally, similar to the laboratory performance ranking, it was assumed that embedding the geogrid at a one-third depth (measured from the bottom) is feasible for each geogrid-reinforced HMA mixture. Therefore, this ranking would take the most cost-effective performance—geogrid-reinforced HMA mixture at one-half depth or one-third depth (measured from the bottom)—to rank each HMA mixture.

Not all cost scenarios considered in the LCCA are likely to occur regularly in society. Extreme economic conditions and construction costs were considered in the LCCA to observe the cost-effectiveness under the worst-case scenarios. Thus, a reduction of 0.5 was applied to the weighting of the extreme GPF values (3.0 and 7.0) results to mitigate the effects of these extreme worst-case situations on the overall cost-evaluation ranking. The results of the ranking based on the LCCA evaluation are presented in Table 29.

Table 31

Ranking of LCCA for Unreinforced and Geogrid-Reinforced HMA Mixtures

HMA Mixtures	Cost-Effectiveness Ranking for each HMA Mixture with Weighting									Total (Max=30)
	GPF 3.0			GPF 5.0			GPF 7.0			
	Average	Maximum	P_{CB}	Average	Maximum	P_{CB}	Average	Maximum	P_{CB}	
	(0.5)	(0.5)	(0.5)	(1.0)	(1.0)	(1.0)	(0.5)	(0.5)	(0.5)	
Control (Unreinforced)	2	2	2	2	2	1	4	2	3	12.5
F-25-100-A	3	3	5	3	3	4	2	3	2	19.0
F-25-200-A	5	4	5	5	4	5	5	4	5	28.0
F-30-100-B	1	1	1	1	1	2	1	1	1	7.0
B-25-90-L	4	5	3	4	5	3	3	5	4	24.0

Finalized Ranking of Geogrid-Reinforced HMA Mixtures

The laboratory performance and LCCA ranking results give an indication of the individualized value of using geogrid reinforcements in HMA layers. It is vital to combine these rankings, however, to gain a better understanding of the value of geogrid reinforcements in HMA layers. Additionally, by finalizing the rankings of each HMA mixtures, further conclusions can be determined on the optimal geogrid type and construction procedure for geogrid-reinforced HMA. The final ranking consists of two major components—laboratory performance and LCCA results—each component receiving an equal weighting (50) for a maximum total of 100 points. The laboratory performance component was further divided in two test conditions: unconditioned performance testing (30 points) and freeze-thaw performance testing (20 points). For the finalized rankings, the percentage was determined of the maximum available points for each ranking category (obtained from Tables 27 through 29) and then multiplied by the respective final ranking weights. Table 30 provides the summarized rankings for each condition considered.

Table 32

Finalized Ranking of Unreinforced and Geogrid-Reinforced HMA Mixtures

HMA Mixture	Laboratory Performance (Unconditioned) (Max=30)	Laboratory Performance (Conditioned) (Max=20)	LCCA Evaluation (Max=50)	Total Ranking (Max=100)
Control (Unreinforced)	12.0	4.0	20.8	36.8
F-25-100-A	22.1	13.3	31.7	67.1
F-25-200-A	28.1	14	46.7	88.8
F-30-100-B	17.7	12.7	11.7	42.1
B-25-90-L	24.3	12.7	40.0	77.0

From Table 30, it can be observed that all geogrid-reinforced HMA mixtures resulted in a higher ranking when compared to the unreinforced HMA mixture. This implies that the use of geogrid-reinforced HMA mixtures is beneficial in terms of performance and cost-effectiveness. In addition to this finding, Table 30 also indicates the geogrid type with the highest tensile strength (F-25-200-A) had the highest ranking score. As mentioned previously, this may be a result of the fact that this geogrid type is able to withstand greater loading before experiencing degradation. This behavior aids in maintaining the structural integrity of the HMA materials. Also when comparing geogrids with similar tensile strength values, the ranking indicated that the geogrid type with basalt fiber (B-25-90-L) had a greater overall ranking compared to the geogrid types with fiberglass (F-25-100-A and F-30-100-B). Finally, it is worth noting that the higher initial construction costs of the high tensile strength geogrid (F-25-200-A) is offset by its improvement in service life.

Chapter 8

Summary, Conclusions, and Recommendations

Summary of Findings and Conclusions

This study evaluated the laboratory fatigue cracking performance of geogrid-reinforced HMA mixtures. Five different HMA mixtures (one unreinforced and four geogrid-reinforced HMA mixtures) were used in this study to investigate the impact of geogrid type on the fatigue cracking performance of geogrid HMA mixtures. In total, all HMA mixtures were subjected to four different laboratory tests—Dynamic Complex Modulus (DCM) test, Overlay (OT) test, Indirect Tension (IDT) test, and four-point Bending Beam Fatigue (BBF) test—with each test giving an indication towards the fatigue resistance of each mixture. Additional testing combinations were included to investigate the impact of temperature (intermediate versus low temperature conditions), effects of freeze-thaw conditioning, and effects of different compaction procedures on the overall fatigue cracking performance of geogrid-reinforced HMA mixtures. Additionally, two separate FEM approaches were developed for geogrid-reinforced HMA mixtures under static and dynamic analyses. One FEM procedure consists of modeling the geogrid and its respective properties. The modeled geogrid is then implemented at the desired depth and a static analysis can then be conducted. The second procedure utilizes modified viscoelastic properties of the HMA layer to include the benefits of the geogrid reinforcement in the modulus degradation response. This method is simplified and can be used to evaluate the performance of geogrid-reinforced HMA under dynamic loading. Finally, a Life-Cycle Cost Analysis was conducted to investigate the cost-effectiveness of using geogrids in HMA layers. The LCCA included parametric evaluation and Monte Carlo simulation to develop a more robust evaluation of the use of geogrids in HMA layers. The LCCA indicated that the use of geogrids can be cost-effective when geogrids are embedded at one-third depth (measured from the bottom) depending on the type of geogrid used.

The summary of findings are as follows:

- The geogrid-reinforced HMA mixtures showed |E*| values within 20% of the unreinforced HMA mixtures at all temperatures and testing frequencies.
- On average, the OT showed an improvement of approximately 788% in number of OT cycles to failure at intermediate temperatures when using geogrid-reinforced HMA. Additionally, at low temperatures, the unreinforced HMA mixtures failed rapidly (within 200 cycles), whereas several geogrid-reinforced HMA mixtures did not achieve failure in the allowable number of load repetitions.
- The BBF test exhibited improved fatigue performance by 71%, on average, for geogrid-reinforced HMA mixtures that have been subjected to freeze-thaw conditioning. The geogrids embedded at half depth and one-third depth (measured from the bottom) exhibited improved fatigue performance by 0% and 140%, respectively.
- The high tensile strength geogrid type showed the greatest improvement in number of OT and BBF cycles to failure with an average increase of 1346% and 282%, respectively. At low temperature, the geogrid-reinforced HMA samples with high tensile strength geogrids did not achieve failure.
- The OT exhibited improved cracking performance by 826%, on average, for geogrid-reinforced HMA mixtures that have been subjected to freeze-thaw conditioning.
- The BBF test exhibited improved fatigue performance by 35%, on average, for geogrid-reinforced HMA mixtures that have been subjected to freeze-thaw conditioning. The

geogrids embedded at half depth and one-third depth (measured from the bottom) exhibited improved fatigue performance by 12% and 59%, respectively.

- The type of laboratory compaction procedure adopted showed no statistically significant difference in fatigue performance of geogrid-reinforced HMA mixtures across different embedment depths and temperatures.
- The use of an orthotropic elastic material behavior for geogrid reinforcements in HMA mixtures was considered the most accurate method when modeling geogrid reinforcements using FEM with an average percent error of 2.57%. Additionally, a unique approach was developed for better definition of the viscoelastic behavior of geogrid-reinforced HMA.
- The LCCA showed a cost benefit when using geogrids embedded at one-third depth (measured from the bottom) with an average cost benefit of approximately $46,000. The average cost benefit ranged from approximately $143,000 to $112,000 depending on the geogrid type and embedment depth.

Based on the laboratory performance testing results, developed FEM procedures, and LCCA on each unreinforced and geogrid-reinforced HMA mixture, the following conclusions were drawn:

- The use of geogrid reinforcements in HMA mixtures showed improved fatigue cracking resistance over unreinforced HMA mixtures. This was evidenced with the fatigue and cracking performance testing results that highlighted the improved number of cycles to failure, greater fracture energy, and greater fatigue factor. All of these laboratory performance findings indicate an increased fatigue cracking performance.

- From the four geogrid types considered in this study, the geogrid type with the highest tensile strength yielded the greatest improvement in fatigue cracking performance. Therefore, it can be concluded that the tensile strength property of the geogrid reinforcement is a critical component in the improvement of fatigue cracking performance of geogrid-reinforced HMA mixtures.
- The results from the overlay test and the indirect tension test showed slower crack propagation behavior in HMA mixtures due to geogrid reinforcements. This change in cracking behavior resulted in slower crack propagation and more ductile failure responses in the HMA mixtures.
- The laboratory testing also indicated that the improvement in fatigue cracking performance of geogrid-reinforced HMA mixtures at low temperatures was better than the fatigue cracking performance at intermediate temperatures.
- The susceptibility of performance of geogrid-reinforced HMA to freeze-thaw cycling is an important factor in determining its use. As evidenced in the laboratory performance testing, the freeze-thaw conditioning decreased the performance of geogrid-reinforced HMA. This can potentially be attributed to the absorption of geogrid reinforcements.
- When modeling the geogrid reinforcement, the choice of element type and geometry for geogrid was critical in the ability to account for the difference in strain response and capture the overall behavior. The 3D stress elements with an orthotropic material behavior model proved to be the most accurate approach in modeling geogrid reinforcement. This approach implies its potential for the modeling of geogrid reinforcement in future studies.

- The LCCA indicated that the use of geogrids can be cost-effective when constructed at one-third depth of the HMA layer (measured from the bottom). Significant variability exists when considering varying economic and construction conditions. It was indicated that the increased cost associated with the use of geogrid reinforcements was offset by the improvement in service life. Further, the high tensile strength geogrid type (F-25-200-A) showed the least variability and greatest average cost benefit.

Recommendations for Future Work

This study focused on the laboratory fatigue cracking performance evaluation of geogrid-reinforced HMA mixtures. Though this study evaluated the laboratory fatigue cracking performance, this study was limited in that field implementation through pilot test sections or accelerated pavement testing should be considered. Through field testing, the following specific topics can be observed or evaluated:

- Investigate construction methods for implementing geogrids within full-scale HMA layers. This investigation can include the method of geogrid placement, HMA compaction temperatures, and application of bonding agents on a full-scale section.

- Evaluate the performance of full-scale geogrid-reinforced HMA pavement layers. The performance evaluation can observe all relevant pavement distresses—rutting, cracking, and shoving—in the pavement sections.

- Evaluate the change in mechanistic responses due to geogrid reinforcements in HMA pavement layers. Through detailed instrumentation, strain gauges can be used to determine if geogrids change the tensile strain contours in HMA layers.

- Calibrate the developed FEM procedures using full-scale pavement responses and performance. Through calibration and validation procedures, future pavement structural design techniques can be developed for geogrid-reinforced HMA pavement layers.

- Assess the removal techniques for geogrid-reinforced HMA from field roadways. This is vital for future implementation of geogrid-reinforced HMA to ensure that the pavement layer can be rehabilitated or reconstructed.

In addition to full-scale pavement testing, the laboratory testing can also be expanded to investigate additional HMA mixtures for use with geogrid reinforcements. This can include different aggregate gradations (such as SMA), binder contents (low versus high binder contents), and binder grades (stiff versus soft binders). All of these factors may contribute to how the geogrid bonds with the HMA mixture and thus should be investigated in the future. Finally, the healing and recovery of geogrid-reinforced HMA mixtures must be investigated. This investigation can lead to a better understanding of the structural capacity of geogrid-reinforced HMA.

References

[1] S. K. Shukla, *Handbook of geosynthetic engineering*. 2011.

[2] R. D. Barksdale, S. F. Brown, and F. Chan, "NCHRP Report 315: Potential Benefits of Geosynthetics in Flexible Pavement Systems," *TRB, Natl. Res. Counc. Washington, DC*, 1989.

[3] B. R. Christopher and R. D. Holtz, "Geotextile Design & Construction Guidelines: Participant Notebook," US Department of Transportation Federal Highway Administration, 1992.

[4] J. W. Button and R. L. Lytton, *Guidelines for using geosynthetics with HMA overlays to reduce reflective cracking*. Texas Transportation Institute, Texas A & M University, 2003.

[5] U.S. Army Corps of Engineers, "Use of Geogrids in Pavement Construction. Technical Letter ETL 1110-1-189," 2003.

[6] J. Tingle and S. Jersey, "Cyclic Plate Load Testing of Geosynthetic-Reinforced Unbound Aggregate Roads," *Transp. Res. Rec. J. Transp. Res. Board*, 2005.

[7] J. Greene, A. Nazef, B. Choubane, and D. Horhota, "Long-Term Evaluation of Geosynthetic Reinforcement of Flexible Pavements Constructed over Thick Organic Soil Deposits," *Transp. Res. Rec. J. Transp. Res. Board*, 2014.

[8] I. Al-Qadi, S. Dessouky, J. Kwon, and E. Tutumluer, "Geogrid in Flexible Pavements: Validated Mechanism," *Transp. Res. Rec. J. Transp. Res. Board*, 2008.

[9] S. W. Perkins and E. R. Cortez, "Evaluation of base-reinforced pavements using a heavy vehicle simulator," *Geosynth. Int.*, 2005.

[10] S. Jersey R, J. Tingle S, G. Norwood J, J. Kwon, and M. Wayne, "Full-Scale Evaluation of Geogrid-Reinforced Thin Flexible Pavements," *Transp. Res. Rec. J. Transp. Res. Board*, 2012.

[11] W. J. Robinson, J. S. Tingle, and G. J. Norwood, "Full-Scale Accelerated Testing of Multi-axial Geogrid Stabilized Flexible Pavements," ERDC-GSL Vicksburg United States, 2017.

[12] F. Gu, X. Luo, R. Luo, R. L. Lytton, E. Y. Hajj, and R. V. Siddharthan, "Numerical modeling of geogrid-reinforced flexible pavement and corresponding validation using large-scale tank test," *Constr. Build. Mater.*, 2016.

[13] A. Wargo, S. A. Safavizadeh, and Y. Richard Kim, *Comparing the performance of fiberglass grid with composite interlayer systems in asphalt concrete*. 2017.

[14] S. Sachs, J. M. Vandenbossche, K. Alland, J. DeSantis, and L. Khazanovich, "Effects of Interlayer Systems on Reflective Cracking in Unbonded Overlays of Existing Concrete Pavements," *Transp. Res. Rec. J. Transp. Res. Board*, no. 2591, pp. 33–41, 2016.

[15] S. Vismara, A. A. A. Molenaar, M. Crispino, and M. R. Poot, “Characterizing the effects of geosynthetics in asphalt pavements,” in *7th RILEM International Conference on Cracking in Pavements*, 2012, pp. 1199–1207.

[16] D. Zamora-Barraza, M. A. Calzada-Pérez, D. Castro-Fresno, and A. Vega-Zamanillo, “Evaluation of anti-reflective cracking systems using geosynthetics in the interlayer zone,” *Geotext. Geomembranes*, vol. 29, no. 2, pp. 130–136, 2011.

[17] L. F. Walubita, A. N. M. Faruk, J. Zhang, and X. Hu, “Characterizing the cracking and fracture properties of geosynthetic interlayer reinforced HMA samples using the Overlay Tester (OT),” *Constr. Build. Mater.*, 2015.

[18] A. Khodaii and S. Fallah, “Effects of geosynthetic reinforcement on the propagation of reflection cracking in asphalt overlays,” *Int. J. Civ. Eng.*, 2009.

[19] K. Sobhan, T. Crooks, V. Tandon, and S. Mattingly, “Laboratory simulation of the growth and propagation of reflection cracks in geogrid reinforced asphalt overlays,” 2004.

[20] K. Sobhan and V. Tandon, “Mitigating reflection cracking in asphalt overlays using geosynthetic reinforcements,” *Road Mater. Pavement Des.*, vol. 9, no. 3, pp. 367–387, 2008.

[21] A. Zofka, M. Maliszewski, and D. Maliszewska, “Glass and carbon geogrid reinforcement of asphalt mixtures,” in *Asphalt Paving Technology: Association of Asphalt Paving Technologists-Proceedings of the Technical Sessions*, 2016.

[22] V. Kumar V and S. Saride, “Use of Digital Image Correlation for the Evaluation of Flexural Fatigue Behavior of Asphalt Beams with Geosynthetic Interlayers,” *Transp. Res. Rec. J. Transp. Res. Board*, no. 2631, pp. 55–64, 2017.

[23] S. Saride and V. V. Kumar, “Influence of geosynthetic-interlayers on the performance of asphalt overlays on pre-cracked pavements,” *Geotext. Geomembranes*, 2017.

[24] R. Gupta, “A study of geosynthetic reinforced flexible pavement system,” 2009.

[25] J. G. Zornberg *et al.*, “Validating mechanisms in geosynthetic reinforced pavements,” 2008.

[26] H. K. Kanerva, T. S. Vinson, and H. Zeng, *Low-temperature cracking: Field validation of the thermal stress restrained specimen test*, no. SHRP-A-401. 1994.

[27] M. G. Bouldin, R. Dongre, G. M. Row, M. J. Sharrock, and D. A. Anderson, “Predicting thermal cracking of pavements from binder properties: theoretical basis and field validation,” in *Association of Asphalt Paving Technologists Proc*, 2000, vol. 69.

[28] Y. H. Huang, “Pavement Analysis and Design,” *Pearson*, 2003.

[29] F. Zhou *et al.*, “NCHRP 9-57: Experimental Design for Field Validation of Laboratory Tests to Assess Cracking Resistance of Asphalt Mixtures,” College Station, Texas, 2016.

[30] M. W. Witczak, K. Kaloush, T. Pellinen, M. El-Basyouny, and H. Von Quintus, *Simple Performance Test for Superpave Mix Design*. 2002.

[31] M. W. Witczak and J. Bari, “Development of a master curve (E*) database for lime modified asphaltic mixtures,” *Arizona State Univ. Res. Report, Tempe (Arizona, USA) Arizona State Univ.*, 2004.

[32] F. Zhou, “Development of an IDEAL Cracking Test for Asphalt Mix Design, Quality Control and Quality Assurance,” *NCHRP-IDEA Progr. Proj.* , vol. 195, 2019.

[33] V. M. Garcia, J. Garibay, I. Abdallah, and S. Nazarian, *Overlay tester results from dense-graded asphalt concrete mixes*. 2017.

[34] V. M. Garcia and A. Miramontes, “Understanding Sources of Variability of Overlay Test Procedure,” *Transp. Res. Rec.*, vol. 2507, pp. 10–18, 2015.

[35] C. Von Holdt and T. Scullion, “Methods of Reducing Joint Reflection Cracking: Field Performance Studies,” Texas Transportation Institute, Texas A & M University System, 2006.

[36] A. Rawal, T. Shah, and S. Anand, “Geotextiles: production, properties and performance,” *Text. Prog.*, vol. 42, no. 3, pp. 181–226, 2010.

[37] G. S. Cleveland, J. W. Button, and R. L. Lytton, *Geosynthetics in flexible and rigid pavement overlay systems to reduce reflection cracking*. Texas Transportation Institute, Texas A & M University System, 2003.

[38] A. Chowdhury, J. W. Button, and R. L. Lytton, “Tests of HMA overlays using geosynthetics to reduce reflection cracking,” Texas Transportation Institute, Texas A & M University System, 2009.

[39] Geosynthetics Materials Association, *Handbook of Geosynthetics*. 2002.

[40] S. W. Perkins, “Geosynthetic reinforcement of flexible pavements: laboratory based pavement test sections. FHWA/MT-99-001/8138,” 1999.

[41] H. I. Ling and Z. Liu, “Performance of geosynthetic-reinforced asphalt pavements,” *J. Geotech. Geoenvironmental Eng.*, vol. 127, no. 2, pp. 177–184, 2001.

[42] Q. Chen, M. Abu-Farsakh, and R. Sharma, “Experimental and analytical studies of reinforced crushed limestone,” *Geotext. Geomembranes*, vol. 27, no. 5, pp. 357–367, 2009.

[43] M. Abu-Farsakh, S. Hanandeh, L. Mohammad, and Q. Chen, “Performance of geosynthetic reinforced/stabilized paved roads built over soft soil under cyclic plate loads,” *Geotext. Geomembranes*, 2016.

[44] J. W. Button and A. Chowdhury, “Field tests using geosynthetics in flexible and rigid pavements to reduce reflection cracking,” Texas Transportation Institute, Texas A & M University System, 2006.

[45] A. Laurinavičius and R. Oginskas, “Experimental research on the development of rutting in asphalt concrete pavements reinforced with geosynthetic materials,” *J. Civ. Eng. Manag.*, vol. 12, no. 4, pp. 311–317, 2006.

[46] R. O. Rasmussen and S. I. Garber, “Nonwoven geotextile interlayers for separating cementititious pavement layers: German practice and US field trials,” 2009.

[47] S. Youwai, W. Kongkitkul, P. Jongpradist, P. Anujorn, and K. Punthutaecha, “Geosynthetics in reinforced flexible pavement: Thailand experience,” in *Proc. of International Symposium, exhibition, and short course on geotechnical and geosynthetics engineering: challenges and opportunities on climate change, Bangkok*, 2010, pp. 220–233.

[48] B. R. Cox, T. M. Goldman, and J. S. McCartney, “The Marked Tree Site: Evaluation of Geosynthetic Reinforcements in Flexible Pavements,” 2011.

[49] J. G. Zornberg, A. Bouazza, and J. S. McCartney, “Geosynthetic capillary barriers: principles and applications,” in *Proceedings 1st African Regional Geosynthetics Conference*, 2009.

[50] F. Moghaddas-Nejad and J. C. Small, “Effect of geogrid reinforcement in model track tests on pavements,” *J. Transp. Eng.*, vol. 122, no. 6, pp. 468–474, 1996.

[51] R. Hufenus, R. Rüegger, D. Flum, and I. J. Sterba, “Strength reduction factors due to installation damage of reinforcing geosynthetics,” *Geotext. Geomembranes*, vol. 23, no. 5, pp. 401–424, 2005.

[52] M. D. Nazzal, M. Y. Abu-Farsakh, and L. N. Mohammad, “Implementation of a critical state two-surface model to evaluate the response of geosynthetic reinforced pavements,” *Int. J. Geomech.*, vol. 10, no. 5, pp. 202–212, 2010.

[53] S. K. Pokharel *et al.*, “Accelerated pavement testing of geocell-reinforced unpaved roads over weak subgrade,” *Transp. Res. Rec.*, vol. 2204, no. 1, pp. 67–75, 2011.

[54] J. Han *et al.*, “Performance of geocell-reinforced RAP bases over weak subgrade under full-scale moving wheel loads,” *J. Mater. Civ. Eng.*, vol. 23, no. 11, pp. 1525–1534, 2011.

[55] X. Tang, M. Abu-Farsakh, S. Hanandeh, and Q. Chen, “Performance of reinforced–stabilized unpaved test sections built over native soft soil under full-scale moving wheel loads,” *Transp. Res. Rec. J. Transp. Res. Board*, no. 2511, pp. 81–89, 2015.

[56] X. Tang, G. R. Chehab, and S. Kim, “Laboratory study of geogrid reinforcement in Portland cement concrete,” in *Proceedings of the 6th RILEM International Conference on Cracking in Pavements*, 2008, pp. 769–778.

[57] J. Norambuena-Contreras and I. Gonzalez-Torre, “Influence of geosynthetic type on retarding cracking in asphalt pavements,” *Constr. Build. Mater.*, vol. 78, pp. 421–429, 2015.

[58] I. Gonzalez-Torre, M. A. Calzada-Perez, A. Vega-Zamanillo, and D. Castro-Fresno, “Evaluation of reflective cracking in pavements using a new procedure that combine loads with different frequencies,” *Constr. Build. Mater.*, vol. 75, pp. 368–374, 2015.

[59] I. Gonzalez-Torre, M. A. Calzada-Perez, A. Vega-Zamanillo, and D. Castro-Fresno, “Experimental study of the behaviour of different geosynthetics as anti-reflective cracking systems using a combined-load fatigue test,” *Geotext. Geomembranes*, vol. 43, no. 4, pp. 345–350, 2015.

[60] D. Zamora-Barraza, M. A. Calzada-Pérez, D. Castro-Fresno, and A. Vega-Zamanillo, “Evaluation of anti-reflective cracking systems using geosynthetics in the interlayer zone,” *Geotext. Geomembranes*, 2011.

[61] P. Zieliński, “Investigations of fatigue of asphalt layers with geosynthetics,” *Arch. Civ. Eng.*, 2013.

[62] S. A. Safavizadeh, A. Wargo, M. Guddati, and Y. R. Kim, “Investigating Reflective Cracking Mechanisms in Grid-Reinforced Asphalt Specimens,” *Transp. Res. Rec. J. Transp. Res. Board*, vol. 2507, pp. 29–38, Oct. 2015.

[63] G. Dondi, “Three-dimensional finite element analysis of a reinforced paved road,” in *Proceedings of the fifth international conference on geotextiles, geomembranes and related products*, 1994, vol. 1, pp. 95–100.

[64] G. W. Wathugala, B. Huang, and S. Pal, “Numerical simulation of geosynthetic-reinforced flexible pavements,” *Transp. Res. Rec.*, vol. 1534, no. 1, pp. 58–65, 1996.

[65] S. W. Perkins, “Numerical modeling of geosynthetic reinforced flexible pavements,” Western Transportation Institute, Department of Civil Engineering, Montana …, 2001.

[66] B. Saad, H. Mitri, and H. Poorooshasb, “3D FE analysis of flexible pavement with geosynthetic reinforcement,” *J. Transp. Eng.*, vol. 132, no. 5, pp. 402–415, 2006.

[67] J. Kwon, “Development of a mechanistic model for geogrid reinforced flexible pavements.” University of Illinois at Urbana-Champaign, 2007.

[68] M. D. Nazzal, “Laboratory characterization and numerical modeling of geogrid reinforced bases in flexible pavements,” 2007.

[69] J. Kwon, E. Tutumluer, and H. Konietzky, “Aggregate base residual stresses affecting geogrid reinforced flexible pavement response,” *Int. J. Pavement Eng.*, vol. 9, no. 4, pp. 275–285, 2008.

[70] M. Y. Abu-Farsakh, J. Gu, G. Z. Voyiadjis, and Q. Chen, "Mechanistic–empirical analysis of the results of finite element analysis on flexible pavement with geogrid base reinforcement," *Int. J. Pavement Eng.*, vol. 15, no. 9, pp. 786–798, 2014.

[71] X. Tang, S. M. Stoffels, and A. M. Palomino, "Mechanistic-empirical approach to characterizing permanent deformation of reinforced soft soil subgrade," *Geotext. Geomembranes*, vol. 44, no. 3, pp. 429–441, 2016.

[72] I. L. Howard and K. A. Warren, "Finite-element modeling of instrumented flexible pavements under stationary transient loading," *J. Transp. Eng.*, vol. 135, no. 2, pp. 53–61, 2009.

[73] H. Moayedi, S. Kazemian, A. Prasad, and B. B. K. Huat, "Effect of geogrid reinforcement location in paved road improvement," *Electron. J. Geotech. Eng.*, vol. 14, pp. 1–11, 2009.

[74] S. Kazemian, M. Barghchi, A. Prasad, H. Maydi, and B. B. K. Huat, "Reinforced pavement above trench under urban traffic load: Case study and finite element (FE) analysis," *Sci. Res. Essays*, vol. 5, no. 21, pp. 3313–3329, 2010.

[75] H. Siriwardane, R. Gondle, and B. Kutuk, "Analysis of flexible pavements reinforced with geogrids," *Geotech. Geol. Eng.*, 2010.

[76] M. Buonsanti and G. Leonardi, "FEM analysis of airport flexible pavements reinforced with geogrids," *Adv. Sci. Lett.*, vol. 13, no. 1, pp. 392–395, 2012.

[77] W.-C. Huang, "Improvement evaluation of subgrade layer under geogrid-reinforced aggregate layer by finite element method," *Int. J. Civ. Eng.*, vol. 12, no. 3, pp. 204–215, 2014.

[78] N. S. Correia, E. R. Esquivel, and J. G. Zornberg, "Finite-Element Evaluations of Geogrid-Reinforced Asphalt Overlays over Flexible Pavements," *J. Transp. Eng. Part B Pavements*, vol. 144, no. 2, p. 4018020, 2018.

[79] M. G. Hussein and M. A. Meguid, "A three-dimensional finite element approach for modeling biaxial geogrid with application to geogrid-reinforced soils," *Geotext. Geomembranes*, vol. 44, no. 3, pp. 295–307, 2016.

[80] M. Abdesssemed, S. Kenai, and A. Bali, "Experimental and numerical analysis of the behavior of an airport pavement reinforced by geogrids," *Constr. Build. Mater.*, vol. 94, pp. 547–554, 2015.

[81] W. J. Robinson, J. S. Tingle, G. J. Norwood, and I. L. Howard, "Assessment of Equivalent Thickness Design Principles for Geosynthetic Reinforced Pavements by Way of Accelerated Testing," *Transp. Res. Rec.*, p. 0361198118781682, 2018.

[82] Asphalt Institute, *Superpave Mix Design Series No. 2 (SP-2)*. Lexington, KY, 1996.

[83] Federal Aviation Administration, "AC No: 150/5370-10G Standards for Specifying Construction of Airports," 2014.

[84] Federal Aviation Administration, "Airport Pavement Design and Evaluation," 2009.

[85] K. P. Delage, "The Effect of Fine Aggregate Angularity on Hot Mixture Asphalt Performance," *Master Degree Thesis, Dep. Civ. Environ. Eng. Univ. Wisconsin-Madison*, 2000.

[86] G. Garcia and M. Thompson, "HMA dynamic modulus predictive models (a review)," 2007.

[87] J. Bari and M. Witczak, "New Predictive Models for Viscosity and Complex Shear Modulus of Asphalt Binders: For Use with Mechanistic-Empirical Pavement Design Guide," *Transp. Res. Rec.*, 2007.

[88] A. K. Naik and K. P. Biligiri, "Predictive models to estimate phase angle of asphalt mixtures," *J. Mater. Civ. Eng.*, vol. 27, no. 8, p. 4014235, 2014.

[89] Q. Ye, S. Wu, and N. Li, "Investigation of the dynamic and fatigue properties of fiber-modified asphalt mixtures," *Int. J. Fatigue*, 2009.

[90] L. N. Mohammad, S. B. Cooper, and M. a. Elseifi, "Characterization of HMA Mixtures Containing High Reclaimed Asphalt Pavement Content with Crumb Rubber Additives," *J. Mater. Civ. Eng.*, 2011.

[91] J. A. Epps, P. E. Sebaaly, J. Penaranda, M. R. Maher, M. B. McCann, and A. J. Hand, "Compatibility of a test for moisture-induced damage with Superpave volumetric mix design. NCHRP Report 444," *Transp. Res. Board-National Res. Counc. Washington, DC*, 2000.

[92] R. P. Lottman, "Predicting moisture-induced damage to asphaltic concrete field evaluation," *NCHRP Rep.*, no. 246, 1982.

[93] D. G. Tunnicliff and R. E. Root, *Use of antistripping additives in asphaltic concrete mixtures: Field evaluation*, vol. 373. Transportation Research Board, 1995.

[94] R. Liang, "Refine AASHTO T283 Resistance of Compacted Bituminous Mixture to Moisture Induced Damage for Superpave.," United States. Federal Highway Administration, 2008.

[95] V. Kumar, "Evaluation of flexural fatigue behavior of two layered asphalt beams with geosynthetic interlayers using digital image correlation," *Transp. Res. Board TRB 2017 Annu. Meet.*, 2017.

[96] R. J. Cominsky, G. A. Huber, T. W. Kennedy, and M. Anderson, *The superpave mix design manual for new construction and overlays*, no. SHRP-A-407. Strategic Highway Research Program Washington, DC, 1994.

[97] S. M. Zaghloul and T. White, "Use of a three-dimensional, dynamic finite element program for analysis of flexible pavement," *Transp. Res. Rec.*, no. 1388, 1993.

[98] A. U. Manual, "Abaqus theory guide," *Version*, vol. 6, p. 14, 2014.

[99] M. S. Mamlouk and J. P. Zaniewski, *Materials for civil and construction engineers*. Pearson Prentice Hall Upper Saddle River, NJ, 2006.

[100] S.-H. Chae, J.-H. Zhao, D. R. Edwards, and P. S. Ho, "Characterization of the viscoelasticity of molding compounds in the time domain," *J. Electron. Mater.*, vol. 39, no. 4, pp. 419–425, 2010.

[101] W. F. Knoff and I. L. Hopkins, "An improved numerical interconversion for creep compliance and relaxation modulus," *J. Appl. Polym. Sci.*, vol. 16, no. 11, pp. 2963–2972, 1972.

[102] M. Baumgaertel and H. H. Winter, "Determination of discrete relaxation and retardation time spectra from dynamic mechanical data," *Rheol. Acta*, vol. 28, no. 6, pp. 511–519, 1989.

[103] S. W. Park and R. A. Schapery, "Methods of interconversion between linear viscoelastic material functions. Part I—A numerical method based on Prony series," *Int. J. Solids Struct.*, vol. 36, no. 11, pp. 1653–1675, 1999.

[104] S. W. Park and Y. R. Kim, "Fitting Prony-series viscoelastic models with power-law presmoothing," *J. Mater. Civ. Eng.*, vol. 13, no. 1, pp. 26–32, 2001.

[105] S. Katicha, "Analysis of Hot Mix Asphalt (HMA) Linear Viscoelastic and Bimodular Properties Using Uniaxial Compression and Indirect Tension (IDT) Tests." Virginia Tech, 2007.

[106] J. Sorvari and M. Malinen, "Numerical interconversion between linear viscoelastic material functions with regularization," *Int. J. Solids Struct.*, vol. 44, no. 3–4, pp. 1291–1303, 2007.

[107] J. A. Hernandez, "Evaluation of the response of perpetual pavement at accelerated pavement loading facility: Finite element analysis and experimental investigation." Ohio University, 2010.

[108] F. Renaud, J.-L. Dion, G. Chevallier, I. Tawfiq, and R. Lemaire, "A new identification method of viscoelastic behavior: Application to the generalized Maxwell model," *Mech. Syst. Signal Process.*, vol. 25, no. 3, pp. 991–1010, 2011.

[109] S. Hu and F. Zhou, "Development of a new interconversion tool for hot mix asphalt (HMA) linear viscoelastic functions," *Can. J. Civ. Eng.*, vol. 37, no. 8, pp. 1071–1081, 2010.

[110] R. M. Mulungye, P. M. O. Owende, and K. Mellon, “Finite element modelling of flexible pavements on soft soil subgrades,” *Mater. Des.*, vol. 28, no. 3, pp. 739–756, 2007.

[111] Y. Chen, “Viscoelastic modeling of flexible pavement.” University of Akron, 2009.

[112] Tensar International Corporation, “GlasGrid Specification Sheet: GG8501/GG8511 Asphalt Reinforcement System,” Alpharetta, GA, 2016.

[113] NCHRP, “Guide for Mechanistic–Empirical Design of New and Rehabilitated Pavement Structures,” 2004.

[114] K. D. Hjelmstad, J. Kim, and Q. H. Zuo, “Finite element procedures for three-dimensional pavement analysis,” in *Proceedings of the 1997 Airfield Pavement Conference*, 1997.

[115] J. Kim and W. G. Buttlar, “Analysis of reflective crack control system involving reinforcing grid over base-isolating interlayer mixture,” *J. Transp. Eng.*, vol. 128, no. 4, pp. 375–384, 2002.

[116] H. Fang, J. E. Haddock, T. D. White, and A. J. Hand, “On the characterization of flexible pavement rutting using creep model-based finite element analysis,” *Finite Elem. Anal. Des.*, vol. 41, no. 1, pp. 49–73, 2004.

[117] G. Leonardi, “Finite element analysis for airfield asphalt pavements rutting prediction,” *Bull. Polish Acad. Sci. Tech. Sci.*, vol. 63, no. 2, pp. 397–403, 2015.

[118] I. L. Al-Qadi and H. Wang, “Full-depth pavement responses under various tire configurations: Accelerated pavement testing and finite element modeling,” *J. Assoc. Asph. Paving Technol.*, vol. 78, pp. 721–760, 2009.

[119] OMB, “Circular No. A-94: Guidelines and discount rates for benefit-cost analysis of federal programs,” 2009.

[120] M. S. Goldberg, “Discount rates for government investment projects: The economic logic behind OMB Circular A-94,” *Eng. Econ.*, vol. 43, no. 4, pp. 290–307, 1998.

[121] D. R. Brill, I. Kawa, and G. F. Hayhoe, “Development of FAARFIELD airport pavement design software,” in *Transportation Systems 2004 Workshop, Ft. Lauderdale, Florida*, 2004.

[122] J. B. Detemple, R. Garcia, and M. Rindisbacher, “A Monte Carlo method for optimal portfolios,” *J. Finance*, vol. 58, no. 1, pp. 401–446, 2003.

[123] P. Glasserman, *Monte Carlo methods in financial engineering*, vol. 53. Springer Science & Business Media, 2013.

[124] K. D. Herbold, “Using Monte Carlo simulation for pavement cost analysis,” *Public Roads*, vol. 64, no. 3, 2000.

[125] M. Liu and D. M. Frangopol, “Multiobjective maintenance planning optimization for deteriorating bridges considering condition, safety, and life-cycle cost,” *J. Struct. Eng.*, vol. 131, no. 5, pp. 833–842, 2005.

[126] A. Kendall, G. A. Keoleian, and G. E. Helfand, “Integrated life-cycle assessment and life-cycle cost analysis model for concrete bridge deck applications,” *J. Infrastruct. Syst.*, vol. 14, no. 3, pp. 214–222, 2008.

[127] E. J. da Silva Pereira, J. T. Pinho, M. A. B. Galhardo, and W. N. Macêdo, “Methodology of risk analysis by Monte Carlo Method applied to power generation with renewable energy,” *Renew. Energy*, vol. 69, pp. 347–355, 2014.

[128] U. Arnold and Ö. Yildiz, “Economic risk analysis of decentralized renewable energy infrastructures–A Monte Carlo Simulation approach,” *Renew. Energy*, vol. 77, pp. 227–239, 2015.

[129] U.S. Department of Agriculture, “Cost Estimating Guide for Road Construction,” *Costos*, 2009.

[130] WSDOT, *Cost Estimating Manual for WSDOT Projects*. 2007.

[131] J. Carnegie, “The Cost of Roadway Construction, Operations and Maintenance in New Jersey: Phase 1 Final Report,” 2016.

Appendix: Life-Cycle Cost Analysis Tables

Table A-1:

Summary of LCCA for each Geogrid-Reinforced HMA Mixture with a GPF 3.0 and a Discount Rate of 1.0%

Geogrid Type		Average	Minimum	Maximum	25th Percentile	75th Percentile	P_{CB}
F-25-100-A	One-Half	($18,371.56)	($63,322.74)	$75,798.77	($46,749.12)	($758.96)	24%
	One-Third	$69,587.20	($11,228.15)	$138,877.13	$59,624.91	$82,372.48	100%
F-25-200-A	One-Half	($12,162.03)	($76,536.10)	$115,950.80	($37,614.31)	$10,510.03	36%
	One-Third	$143,130.11	$8,870.67	$226,405.84	$126,613.92	$164,149.50	100%
F-30-100-B	One-Half	($58,802.56)	($65,084.33)	($33,953.25)	($59,728.63)	($58,013.28)	0%
	One-Third	($65,082.30)	($73,741.94)	($38,760.98)	($66,941.80)	($63,263.45)	0%
B-25-90-L	One-Half	$624.13	($63,817.17)	$143,222.35	($24,420.40)	$23,015.80	49%
	One-Third	$97,215.34	($63,817.17)	$282,514.86	$55,865.40	$147,693.90	89%

Table A-2:

Summary of LCCA for each Geogrid-Reinforced HMA Mixture with a GPF 3.0 and a Discount Rate of 1.5%

Geogrid Type		Average	Minimum	Maximum	25th Percentile	75th Percentile	P_{CB}
F-25-100-A	One-Half	($18,313.55)	($72,201.15)	$70,547.87	($47,049.40)	($1,014.01)	23%
	One-Third	$58,651.05	($10,434.79)	$114,350.18	$51,778.98	$68,480.34	100%
F-25-200-A	One-Half	($15,194.28)	($84,403.82)	$93,848.28	($33,854.71)	$5,042.04	31%
	One-Third	$111,230.97	$32,656.17	$165,542.67	$99,372.24	$127,194.60	100%
F-30-100-B	One-Half	($59,785.31)	($67,199.46)	($30,413.88)	($60,982.56)	($58,622.53)	0%
	One-Third	($68,531.06)	($81,111.78)	($57,468.60)	($71,157.90)	($65,918.78)	0%
B-25-90-L	One-Half	($2,568.70)	($71,684.89)	$106,667.15	($21,348.66)	$17,773.43	47%
	One-Third	$78,572.25	($71,684.89)	$210,454.53	$50,305.47	$118,653.42	89%

Table A-3:

Summary of LCCA for each Geogrid-Reinforced HMA Mixture with a GPF 3.0 and a Discount Rate of 2.0%

Geogrid Type		Average	Minimum	Maximum	25th Percentile	75th Percentile	P_{CB}
F-25-100-A	One-Half	($19,701.69)	($77,294.05)	$54,354.12	($47,286.47)	($3,194.83)	19%
	One-Third	$47,783.23	($7,889.36)	$89,165.29	$43,162.02	$55,441.12	100%
F-25-200-A	One-Half	($18,236.02)	($91,498.29)	$76,842.64	($32,269.10)	($37.43)	25%
	One-Third	$85,290.61	$4,527.45	$120,752.05	$77,234.89	$96,998.76	100%
F-30-100-B	One-Half	($60,529.71)	($71,375.97)	($27,204.43)	($61,994.57)	($59,107.09)	0%
	One-Third	($71,416.05)	($87,713.25)	($59,107.09)	($74,759.12)	($68,124.20)	0%
B-25-90-L	One-Half	($5,408.44)	($78,779.35)	$87,383.14	($19,393.51)	$12,970.68	44%
	One-Third	$60,593.02	($78,779.35)	$148,136.09	$41,223.36	$93,438.86	89%

Table A-4:

Summary of LCCA for each Geogrid-Reinforced HMA Mixture with a GPF 3.0 and a Discount Rate of 2.5%

Geogrid Type		Average	Minimum	Maximum	25th Percentile	75th Percentile	P_{CB}
F-25-100-A	One-Half	($20,760.85)	($85,696.08)	$40,420.33	($47,469.94)	($4,849.36)	15%
	One-Third	$38,221.57	($12,915.04)	$69,866.75	$35,183.70	$44,342.55	100%
F-25-200-A	One-Half	($20,925.60)	($97,898.74)	$54,936.07	($30,871.92)	($4,412.22)	19%
	One-Third	$63,830.13	$19,088.03	$87,125.35	$58,176.13	$72,359.99	100%
F-30-100-B	One-Half	($61,168.92)	($71,835.01)	($27,390.38)	($62,798.91)	($59,485.49)	0%
	One-Third	($73,820.07)	($91,196.49)	($56,331.73)	($77,817.09)	($69,937.46)	0%
B-25-90-L	One-Half	($8,699.09)	($85,179.81)	$72,674.80	($18,530.56)	$8,102.80	40%
	One-Third	$46,986.56	($85,179.81)	$104,957.81	$34,240.63	$73,913.94	87%

Table A-5:

Summary of LCCA for each Geogrid-Reinforced HMA Mixture with a GPF 3.0 and a Discount Rate of 3.0%

Geogrid Type		Average	Minimum	Maximum	25th Percentile	75th Percentile	P_{CB}
F-25-100-A	One-Half	($22,302.48)	($91,473.31)	$35,184.01	($47,608.11)	($7,106.63)	9%
	One-Third	$29,565.03	($13,713.76)	$54,253.60	$27,627.42	$34,473.34	99%
F-25-200-A	One-Half	($23,582.45)	($103,675.98)	$43,068.20	($30,507.40)	($8,548.24)	14%
	One-Third	$45,915.86	($4,178.90)	$60,950.94	$42,157.34	$52,120.11	100%
F-30-100-B	One-Half	($61,655.05)	($75,769.62)	($27,591.89)	($63,425.39)	($59,773.75)	0%
	One-Third	($75,967.89)	($98,919.31)	($58,027.31)	($80,395.41)	($71,409.37)	0%
B-25-90-L	One-Half	($10,944.76)	($90,957.05)	$55,428.42	($17,724.68)	$4,200.44	34%
	One-Third	$34,705.76	($90,957.05)	$78,627.26	$26,936.93	$56,668.50	86%

Table A-6:

Summary of LCCA for each Geogrid-Reinforced HMA Mixture with a GPF 4.0 and a Discount Rate of 1.0%

Geogrid Type		Average	Minimum	Maximum	25th Percentile	75th Percentile	P_{CB}
F-25-100-A	One-Half	($27,682.94)	($73,520.63)	$71,661.14	($55,936.32)	($10,384.30)	14%
	One-Third	$60,545.93	($19,245.64)	$128,432.32	$50,790.18	$72,954.75	100%
F-25-200-A	One-Half	($21,650.27)	($85,723.30)	$113,709.74	($46,790.57)	$861.66	26%
	One-Third	$134,043.66	$12,825.12	$216,246.66	$117,558.00	$155,000.34	100%
F-30-100-B	One-Half	($67,989.14)	($73,356.56)	($36,744.80)	($68,915.83)	($67,200.48)	0%
	One-Third	($74,288.05)	($82,929.14)	($49,071.32)	($76,129.00)	($72,450.65)	0%
B-25-90-L	One-Half	($8,767.14)	($71,993.67)	$116,415.04	($33,673.53)	$13,515.43	38%
	One-Third	$88,907.57	($73,004.37)	$266,433.50	$48,048.78	$138,627.48	87%

Table A-7:

Summary of LCCA for each Geogrid-Reinforced HMA Mixture with a GPF 4.0 and a Discount Rate of 1.5%

Geogrid Type		Average	Minimum	Maximum	25th Percentile	75th Percentile	P_{CB}
F-25-100-A	One-Half	($27,863.53)	($79,879.78)	$58,524.00	($56,236.60)	($10,800.81)	11%
	One-Third	$49,301.98	($20,878.59)	$101,176.75	$42,593.95	$59,082.63	99%
F-25-200-A	One-Half	($24,358.48)	($93,591.02)	$87,148.74	($43,166.76)	($4,436.95)	21%
	One-Third	$102,106.89	($4,771.79)	$151,624.11	$90,410.02	$118,016.39	100%
F-30-100-B	One-Half	($69,011.33)	($77,686.54)	($35,889.49)	($70,169.76)	($67,809.73)	0%
	One-Third	($77,727.33)	($90,298.98)	($65,518.93)	($80,345.10)	($75,105.98)	0%
B-25-90-L	One-Half	($11,488.17)	($80,872.09)	$100,417.46	($30,326.11)	$9,101.99	35%
	One-Third	$68,764.91	($80,872.09)	$198,214.61	$40,258.17	$109,813.21	86%

Table A-8:

Summary of LCCA for each Geogrid-Reinforced HMA Mixture with a GPF 4.0 and a Discount Rate of 2.0%

Geogrid Type		Average	Minimum	Maximum	25th Percentile	75th Percentile	P_{CB}
F-25-100-A	One-Half	($29,012.94)	($88,482.82)	$45,421.54	($56,473.67)	($12,877.82)	8%
	One-Third	$38,481.12	($59,304.53)	$80,051.38	$34,009.44	$46,532.41	99%
F-25-200-A	One-Half	($26,570.15)	($100,685.49)	$67,170.82	($40,544.74)	($8,474.04)	15%
	One-Third	$75,891.98	$22,706.51	$111,699.73	$67,974.54	$87,596.49	100%
F-30-100-B	One-Half	($69,763.62)	($80,563.17)	($36,391.63)	($71,181.77)	($68,294.29)	0%
	One-Third	($80,619.19)	($96,900.45)	($42,880.82)	($83,946.32)	($77,311.40)	0%
B-25-90-L	One-Half	($14,414.85)	($87,966.55)	$79,851.24	($28,256.41)	$3,900.49	30%
	One-Third	$52,115.24	($87,966.55)	$141,246.36	$32,975.94	$84,652.94	85%

Table A-9:

Summary of LCCA for each Geogrid-Reinforced HMA Mixture with a GPF 4.0 and a Discount Rate of 2.5%

Geogrid Type		Average	Minimum	Maximum	25th Percentile	75th Percentile	P_{CB}
F-25-100-A	One-Half	($29,755.03)	($94,883.28)	$30,747.57	($56,657.14)	($14,174.07)	4%
	One-Third	$29,095.99	($18,605.73)	$62,284.85	$26,156.94	$35,326.54	97%
F-25-200-A	One-Half	($29,632.96)	($107,085.94)	$48,610.74	($39,604.21)	($13,472.46)	13%
	One-Third	$54,337.35	$10,907.79	$76,445.87	$49,053.08	$62,947.43	100%
F-30-100-B	One-Half	($70,370.14)	($82,967.21)	($36,701.21)	($71,986.11)	($68,672.69)	0%
	One-Third	($83,124.88)	($105,302.48)	($65,518.93)	($87,004.29)	($79,124.66)	0%
B-25-90-L	One-Half	($17,681.00)	($94,367.01)	$57,371.70	($27,857.19)	($731.20)	24%
	One-Third	$36,916.92	($94,367.01)	$96,503.78	$25,148.13	$64,103.32	83%

Table A-10:

Summary of LCCA for each Geogrid-Reinforced HMA Mixture with a GPF 4.0 and a Discount Rate of 3.0%

Geogrid Type		Average	Minimum	Maximum	25th Percentile	75th Percentile	P_{CB}
F-25-100-A	One-Half	($31,372.64)	($97,687.31)	$23,448.36	($56,795.31)	($16,361.30)	2%
	One-Third	$20,334.72	($19,975.32)	$45,849.08	$18,456.06	$25,353.96	92%
F-25-200-A	One-Half	($32,937.71)	($112,863.18)	$33,814.71	($39,595.55)	($17,824.74)	13%
	One-Third	$36,539.63	($20,365.40)	$51,964.25	$32,861.06	$42,829.92	100%
F-30-100-B	One-Half	($70,821.42)	($84,956.82)	($36,506.29)	($72,612.59)	($68,960.95)	0%
	One-Third	($85,094.00)	($111,079.71)	($65,518.93)	($89,582.61)	($80,596.57)	0%
B-25-90-L	One-Half	($20,544.84)	($100,144.25)	$44,092.65	($27,208.10)	($5,014.66)	16%
	One-Third	$24,880.94	($100,144.25)	$69,744.43	$17,191.09	$47,522.11	78%

Table A-11:

Summary of LCCA for each Geogrid-Reinforced HMA Mixture with a GPF 5.0 and a Discount Rate of 1.0%

Geogrid Type		Average	Minimum	Maximum	25th Percentile	75th Percentile	P_{CB}
F-25-100-A	One-Half	($36,225.82)	($81,697.14)	$59,537.01	($65,123.52)	($19,076.92)	7%
	One-Third	$51,489.09	($37,506.05)	$114,409.43	$41,882.36	$63,805.57	99%
F-25-200-A	One-Half	($30,884.14)	($94,910.50)	$99,254.36	($56,005.16)	($8,286.97)	18%
	One-Third	$125,237.51	($16,395.68)	$210,690.17	$108,290.23	$146,173.16	100%
F-30-100-B	One-Half	($77,142.45)	($84,382.84)	($51,402.93)	($78,103.03)	($76,387.68)	0%
	One-Third	($83,517.36)	($92,116.34)	($75,542.72)	($85,316.20)	($81,637.85)	0%
B-25-90-L	One-Half	($17,846.90)	($82,191.57)	$119,576.28	($42,698.32)	$4,179.13	29%
	One-Third	$80,113.85	($82,191.57)	$279,869.24	$38,196.15	$131,435.49	85%

Table A-12:

Summary of LCCA for each Geogrid-Reinforced HMA Mixture with a GPF 5.0 and a Discount Rate of 1.5%

Geogrid Type		Average	Minimum	Maximum	25th Percentile	75th Percentile	P_{CB}
F-25-100-A	One-Half	($37,189.89)	($89,066.98)	$45,338.13	($65,423.80)	($20,183.77)	4%
	One-Third	$40,054.93	($30,831.28)	$91,525.74	$33,339.07	$49,930.92	97%
F-25-200-A	One-Half	($33,552.53)	($102,778.22)	$81,764.27	($52,401.88)	($13,326.73)	13%
	One-Third	$93,154.30	$16,192.76	$144,306.17	$81,421.97	$108,528.41	100%
F-30-100-B	One-Half	($78,077.53)	($86,873.74)	($47,163.58)	($79,356.96)	($76,996.93)	0%
	One-Third	($86,913.02)	($99,486.18)	($75,843.00)	($89,532.30)	($84,293.18)	0%
B-25-90-L	One-Half	($20,903.50)	($90,059.29)	$86,416.64	($39,931.49)	($267.55)	25%
	One-Third	$58,876.41	($90,059.29)	$190,491.97	$30,180.66	$99,339.57	83%

Table A-13:

Summary of LCCA for each Geogrid-Reinforced HMA Mixture with a GPF 5.0 and a Discount Rate of 2.0%

Geogrid Type		Average	Minimum	Maximum	25th Percentile	75th Percentile	P_{CB}
F-25-100-A	One-Half	($38,052.89)	($97,670.02)	$37,403.64	($65,660.87)	($21,849.32)	2%
	One-Third	$29,488.20	($27,203.71)	$74,438.09	$24,800.24	$37,463.98	94%
F-25-200-A	One-Half	($36,432.18)	($109,872.69)	$64,300.66	($50,187.10)	($18,457.94)	13%
	One-Third	$66,757.32	($8,808.00)	$100,773.12	$58,883.69	$78,497.90	100%
F-30-100-B	One-Half	($78,917.89)	($89,750.37)	($46,942.03)	($80,368.97)	($77,481.49)	0%
	One-Third	($89,781.80)	($106,087.65)	($51,279.70)	($93,133.52)	($86,498.60)	0%
B-25-90-L	One-Half	($24,275.02)	($97,153.75)	$69,980.61	($37,853.06)	($5,996.98)	18%
	One-Third	$42,830.64	($97,153.75)	$130,426.85	$23,627.59	$75,575.17	81%

Table A-14:

Summary of LCCA for each Geogrid-Reinforced HMA Mixture with a GPF 5.0 and a Discount Rate of 2.5%

Geogrid Type		Average	Minimum	Maximum	25th Percentile	75th Percentile	P_{CB}
F-25-100-A	One-Half	($38,976.29)	($101,580.72)	$27,483.17	($65,844.34)	($23,544.95)	1%
	One-Third	$19,936.12	($27,008.52)	$52,898.07	$16,966.06	$25,998.83	90%
F-25-200-A	One-Half	($39,393.75)	($116,273.14)	$34,830.29	($49,236.74)	($22,813.36)	13%
	One-Third	$45,061.98	($43,977.02)	$68,747.08	$39,735.69	$53,746.71	100%
F-30-100-B	One-Half	($79,584.18)	($90,209.41)	($44,471.19)	($81,173.31)	($77,859.89)	0%
	One-Third	($92,166.41)	($111,999.92)	($76,263.54)	($96,191.49)	($88,311.86)	0%
B-25-90-L	One-Half	($27,039.12)	($103,554.21)	$52,480.43	($37,141.21)	($10,168.56)	13%
	One-Third	$28,584.99	($103,554.21)	$90,785.28	$16,329.78	$54,869.27	78%

Table A-15:

Summary of LCCA for each Geogrid-Reinforced HMA Mixture with a GPF 5.0 and a Discount Rate of 3.0%

Geogrid Type		Average	Minimum	Maximum	25th Percentile	75th Percentile	P_{CB}
F-25-100-A	One-Half	($40,385.01)	($106,874.51)	$12,672.49	($65,982.51)	($25,480.50)	1%
	One-Third	$11,176.02	($30,652.89)	$36,165.35	$9,095.38	$16,207.26	90%
F-25-200-A	One-Half	($42,064.90)	($122,050.38)	$21,344.56	($48,812.27)	($26,982.91)	4%
	One-Third	$27,348.73	($23,724.75)	$42,851.36	$23,663.46	$33,659.57	100%
F-30-100-B	One-Half	($80,110.99)	($91,931.68)	($45,778.88)	($81,799.79)	($78,148.15)	0%
	One-Third	($94,323.22)	($117,293.71)	($74,706.13)	($98,769.81)	($89,783.77)	0%
B-25-90-L	One-Half	($29,336.40)	($109,331.45)	$34,739.34	($36,132.44)	($14,111.81)	14%
	One-Third	$15,839.15	($109,331.45)	$60,283.79	$8,466.15	$38,321.30	78%

Table A-16:

Summary of LCCA for each Geogrid-Reinforced HMA Mixture with a GPF 6.0 and a Discount Rate of 1.0%

Geogrid Type		Average	Minimum	Maximum	25th Percentile	75th Percentile	P_{CB}
F-25-100-A	One-Half	($45,775.66)	($91,895.03)	$40,203.76	($74,310.72)	($28,351.63)	3%
	One-Third	$42,040.87	($50,605.44)	$117,020.59	$32,424.76	$54,642.18	96%
F-25-200-A	One-Half	($40,223.26)	($104,097.70)	$91,910.71	($65,210.48)	($17,991.54)	13%
	One-Third	$115,863.80	$13,951.46	$195,782.74	$99,319.60	$136,649.15	100%
F-30-100-B	One-Half	($86,393.70)	($92,645.93)	($61,046.00)	($87,290.23)	($85,574.88)	0%
	One-Third	($92,674.62)	($101,303.54)	($84,729.92)	($94,503.40)	($90,825.05)	0%
B-25-90-L	One-Half	($27,509.31)	($91,378.77)	$109,740.33	($52,333.94)	($4,702.13)	21%
	One-Third	$70,106.84	($91,378.77)	$262,602.65	$28,399.23	$120,414.28	81%

Table A-17:

Summary of LCCA for each Geogrid-Reinforced HMA Mixture with a GPF 6.0 and a Discount Rate of 1.5%

Geogrid Type		Average	Minimum	Maximum	25th Percentile	75th Percentile	P_{CB}
F-25-100-A	One-Half	($46,080.82)	($98,254.18)	$39,658.47	($74,611.00)	($29,349.12)	1%
	One-Third	$30,711.82	($36,772.59)	$92,468.60	$24,004.56	$40,746.82	92%
F-25-200-A	One-Half	($43,354.61)	($111,965.42)	$63,507.34	($62,139.29)	($23,072.20)	13%
	One-Third	$83,866.06	($23,095.07)	$138,599.25	$72,260.83	$99,542.62	100%
F-30-100-B	One-Half	($87,322.70)	($94,761.06)	($56,737.19)	($88,544.16)	($86,184.13)	0%
	One-Third	($96,094.61)	($108,673.38)	($86,184.13)	($98,719.50)	($93,480.38)	0%
B-25-90-L	One-Half	($30,090.85)	($99,246.49)	$80,033.90	($49,059.21)	($9,787.72)	15%
	One-Third	$51,004.87	($99,246.49)	$184,441.26	$22,197.10	$91,465.22	79%

Table A-18:

Summary of LCCA for each Geogrid-Reinforced HMA Mixture with a GPF 6.0 and a Discount Rate of 2.0%

Geogrid Type		Average	Minimum	Maximum	25th Percentile	75th Percentile	P_{CB}
F-25-100-A	One-Half	($47,201.85)	($106,857.22)	$25,691.16	($74,848.07)	($31,085.67)	1%
	One-Third	$20,252.54	($39,679.65)	$61,302.97	$15,761.48	$28,033.26	90%
F-25-200-A	One-Half	($45,953.96)	($119,059.89)	$51,002.99	($59,741.06)	($27,751.15)	11%
	One-Third	$57,362.40	$99.67	$91,061.87	$49,559.86	$69,091.01	100%
F-30-100-B	One-Half	($88,113.22)	($97,295.59)	($55,855.10)	($89,556.17)	($86,668.69)	0%
	One-Third	($99,040.11)	($117,276.42)	($85,267.27)	($102,320.72)	($95,685.80)	0%
B-25-90-L	One-Half	($32,640.26)	($106,340.95)	$63,521.03	($46,783.80)	($14,450.52)	14%
	One-Third	$33,461.01	($106,340.95)	$121,958.70	$14,038.79	$66,442.82	78%

Table A-19:

Summary of LCCA for each Geogrid-Reinforced HMA Mixture with a GPF 6.0 and a Discount Rate of 2.5%

Geogrid Type		Average	Minimum	Maximum	25th Percentile	75th Percentile	P_{CB}
F-25-100-A	One-Half	($48,136.18)	($113,257.68)	$22,838.17	($75,031.54)	($32,330.91)	1%
	One-Third	$10,764.35	($41,543.48)	$42,670.27	$7,866.85	$16,878.10	90%
F-25-200-A	One-Half	($48,583.60)	($125,460.34)	$26,614.63	($58,409.85)	($31,920.26)	4%
	One-Third	$35,982.68	($31,590.66)	$58,804.75	$30,498.91	$44,659.50	100%
F-30-100-B	One-Half	($88,703.21)	($99,396.61)	($54,060.36)	($90,360.51)	($87,047.09)	0%
	One-Third	($101,441.53)	($121,187.12)	($85,450.74)	($105,378.69)	($97,499.06)	0%
B-25-90-L	One-Half	($35,649.11)	($112,741.41)	$38,796.81	($45,397.92)	($19,384.25)	13%
	One-Third	$18,921.14	($112,741.41)	$80,903.29	$6,552.42	$45,760.52	78%

Table A-20:

Summary of LCCA for each Geogrid-Reinforced HMA Mixture with a GPF 6.0 and a Discount Rate of 3.0%

Geogrid Type		**Average**	**Minimum**	**Maximum**	**25th Percentile**	**75th Percentile**	**P_{CB}**
F-25-100-A	One-Half	($49,623.22)	($116,061.71)	$7,897.06	($75,169.71)	($34,357.48)	0%
	One-Third	$2,045.13	($43,891.59)	$26,135.85	$112.86	$7,018.14	76%
F-25-200-A	One-Half	($51,399.93)	($131,237.58)	$12,103.06	($58,014.69)	($36,433.86)	0%
	One-Third	$18,246.31	($30,965.86)	$33,473.33	$14,513.14	$24,489.34	97%
F-30-100-B	One-Half	($89,200.55)	($101,118.88)	($54,456.61)	($90,986.99)	($87,335.35)	0%
	One-Third	($103,443.96)	($129,454.11)	($58,613.48)	($107,957.01)	($98,970.97)	0%
B-25-90-L	One-Half	($38,411.23)	($118,518.65)	$24,307.78	($45,168.99)	($23,290.78)	8%
	One-Third	$7,036.83	($118,518.65)	$51,016.58	($622.74)	$29,071.49	74%

Table A-21:

Summary of LCCA for each Geogrid-Reinforced HMA Mixture with a GPF 7.0 and a Discount Rate of 1.0%

Geogrid Type		Average	Minimum	Maximum	25th Percentile	75th Percentile	P_{CB}
F-25-100-A	One-Half	($54,656.37)	($100,071.54)	$48,897.77	($83,497.92)	($37,071.88)	1%
	One-Third	$32,869.38	($46,082.04)	$102,755.29	$23,129.61	$45,231.02	90%
F-25-200-A	One-Half	($49,170.14)	($113,284.90)	$88,138.17	($74,585.04)	($26,012.64)	13%
	One-Third	$106,443.85	($37,550.82)	$187,219.29	$90,373.13	$127,176.74	100%
F-30-100-B	One-Half	($95,589.92)	($101,833.13)	($69,958.93)	($96,477.43)	($94,762.08)	0%
	One-Third	($101,844.13)	($110,490.74)	($77,390.38)	($103,690.60)	($100,012.25)	0%
B-25-90-L	One-Half	($36,346.49)	($100,565.97)	$92,426.24	($61,706.25)	($13,812.89)	14%
	One-Third	$61,797.07	($100,565.97)	$252,997.78	$20,150.79	$112,569.72	79%

Table A-22:

Summary of LCCA for each Geogrid-Reinforced HMA Mixture with a GPF 7.0 and a Discount Rate of 1.5%

Geogrid Type		Average	Minimum	Maximum	25th Percentile	75th Percentile	P_{CB}
F-25-100-A	One-Half	($55,537.70)	($108,949.95)	$30,566.49	($83,798.20)	($38,630.86)	1%
	One-Third	$21,555.44	($53,387.15)	$74,307.72	$14,835.43	$31,324.50	90%
F-25-200-A	One-Half	($51,991.41)	($121,152.62)	$59,535.90	($70,971.96)	($32,326.50)	9%
	One-Third	$74,526.22	($1,635.00)	$124,653.44	$63,019.83	$90,346.72	100%
F-30-100-B	One-Half	($96,459.56)	($103,948.26)	($64,397.19)	($97,731.36)	($95,371.33)	0%
	One-Third	($105,282.16)	($117,860.58)	($72,956.88)	($107,906.70)	($102,667.58)	0%
B-25-90-L	One-Half	($38,986.40)	($108,433.69)	$74,733.24	($57,774.94)	($18,830.53)	13%
	One-Third	$40,223.78	($108,433.69)	$168,240.05	$12,071.24	$81,142.10	78%

Table A-23:

Summary of LCCA for each Geogrid-Reinforced HMA Mixture with a GPF 7.0 and a Discount Rate of 2.0%

Geogrid Type		Average	Minimum	Maximum	25th Percentile	75th Percentile	P_{CB}
F-25-100-A	One-Half	($56,670.82)	($116,044.42)	$22,248.98	($84,035.27)	($40,594.95)	1%
	One-Third	$11,115.00	($52,383.04)	$50,712.96	$6,644.89	$18,980.90	90%
F-25-200-A	One-Half	($54,772.64)	($128,247.09)	$44,516.20	($69,003.50)	($36,339.59)	4%
	One-Third	$48,298.31	($10,873.54)	$84,293.07	$40,158.22	$60,091.38	100%
F-30-100-B	One-Half	($97,337.38)	($106,482.79)	($63,183.74)	($98,743.37)	($95,855.89)	0%
	One-Third	($108,191.34)	($126,463.62)	($69,813.18)	($111,507.92)	($104,873.00)	0%
B-25-90-L	One-Half	($41,922.23)	($115,528.15)	$53,177.11	($56,093.24)	($23,589.83)	13%
	One-Third	$23,934.40	($115,528.15)	$112,392.86	$4,991.23	$57,326.71	78%

Table A-24:

Summary of LCCA for each Geogrid-Reinforced HMA Mixture with a GPF 7.0 and a Discount Rate of 2.5%

Geogrid Type		Average	Minimum	Maximum	25th Percentile	75th Percentile	P_{CB}
F-25-100-A	One-Half	($57,861.92)	($122,444.88)	$8,065.52	($84,218.74)	($41,870.34)	0%
	One-Third	$1,474.41	($48,608.58)	$32,733.16	($1,488.04)	$7,722.77	67%
F-25-200-A	One-Half	($57,731.97)	($134,647.54)	$22,332.28	($67,621.48)	($41,289.61)	0%
	One-Third	$26,651.36	($40,161.54)	$49,505.57	$21,292.31	$35,403.52	98%
F-30-100-B	One-Half	($97,908.60)	($108,583.81)	($62,836.62)	($99,547.71)	($96,234.29)	0%
	One-Third	($110,632.05)	($130,374.32)	($94,637.94)	($114,565.89)	($106,686.26)	0%
B-25-90-L	One-Half	($44,220.98)	($121,928.61)	$35,217.26	($54,166.62)	($27,723.43)	7%
	One-Third	$9,836.78	($121,928.61)	$71,427.47	($2,600.98)	$36,697.06	72%

Table A-25:

Summary of LCCA for each Geogrid-Reinforced HMA Mixture with a GPF 7.0 and a Discount Rate of 3.0%

Geogrid Type		Average	Minimum	Maximum	25th Percentile	75th Percentile	P_{CB}
F-25-100-A	One-Half	($58,884.56)	($128,222.11)	($1,691.52)	($84,356.91)	($43,721.81)	0%
	One-Third	($7,162.74)	($45,688.12)	$16,986.63	($9,030.80)	($2,291.30)	13%
F-25-200-A	One-Half	($60,607.48)	($140,424.78)	$3,423.78	($67,088.50)	($45,481.84)	0%
	One-Third	$9,026.45	($22,709.72)	$24,477.50	$5,272.20	$15,273.59	95%
F-30-100-B	One-Half	($98,559.82)	($112,518.42)	($62,753.03)	($100,174.19)	($96,522.55)	0%
	One-Third	($112,670.09)	($135,668.11)	($65,518.23)	($117,144.21)	($108,158.17)	0%
B-25-90-L	One-Half	($47,645.35)	($127,705.85)	$17,614.30	($54,331.77)	($32,601.51)	1%
	One-Third	($2,500.88)	($127,705.85)	$41,746.04	($10,458.80)	$20,036.67	57%